Characteristics and scaling of tungsten-wire-array *z*-pinch implosion dynamics at 20 MA

M. E. Cuneo,[1,*] E. M. Waisman,[1] S. V. Lebedev,[2] J. P. Chittenden,[2] W. A. Stygar,[1] G. A. Chandler,[1] R. A. Vesey,[1] E. P. Yu,[1] T. J. Nash,[1] D. E. Bliss,[1] G. S. Sarkisov,[3] T. C. Wagoner,[3] G. R. Bennett,[1] D. B. Sinars,[1] J. L. Porter,[1] W. W. Simpson,[1] L. E. Ruggles,[1] D. F. Wenger,[1] C. J. Garasi,[1] B. V. Oliver,[4] R A. Aragon,[1] W. E. Fowler,[1] M. C. Hettrick,[5] G. C. Idzorek,[6] D. Johnson,[1] K. Keller,[1] S. E. Lazier,[3] J. S. McGurn,[1] T. A. Mehlhorn,[1] T. Moore,[3] D. S. Nielsen,[3] J. Pyle,[3] S. Speas,[1] K. W. Struve,[1] and J. A. Torres[1]

[1]*Pulsed Power Sciences Center, Sandia National Laboratories, Albuquerque, New Mexico 87195-1193, USA*

[2]*The Blackett Laboratory, Imperial College, London, United Kingdom*

[3]*Ktech Corporation, Albuquerque, New Mexico 87123, USA*

[4]*Mission Research Corporation, Albuquerque, New Mexico 87110, USA*

[5]*Hettrick Scientific, 1-39-59 Tama-cho, Fuchu-shi, Tokyo, Japan*

[6]*Los Alamos National Laboratory, Los Alamos, New Mexico 87545, USA*

(Received 13 June 2003; revised manuscript received 14 May 2004; published 22 April 2005)

We present observations for 20-MA wire-array *z* pinches of an extended wire ablation period of $57\% \pm 3\%$ of the stagnation time of the array and non-thin-shell implosion trajectories. These experiments were performed with 20-mm-diam wire arrays used for the double-*z*-pinch inertial confinement fusion experiments [M. E. Cuneo *et al.*, Phys. Rev. Lett. **88**, 215004 (2002)] on the *Z* accelerator [R. B. Spielman *et al.*, Phys. Plasmas **5**, 2105 (1998)]. This array has the smallest wire-wire gaps typically used at 20 MA (209 μm). The extended ablation period for this array indicates that two-dimensional (*r*-*z*) thin-shell implosion models that implicitly assume wire ablation and wire-to-wire merger into a shell on a rapid time scale compared to wire acceleration are fundamentally incorrect or incomplete for high-wire-number, massive (>2 mg/cm), single, tungsten wire arrays. In contrast to earlier work where the wire array accelerated from its initial position at $\sim 80\%$ of the stagnation time, our results show that very late acceleration is not a universal aspect of wire array implosions. We also varied the ablation period between $46\% \pm 2\%$ and $71\% \pm 3\%$ of the stagnation time, for the first time, by scaling the array diameter between 40 mm (at a wire-wire gap of 524 μm) and 12 mm (at a wire-wire gap of 209 μm), at a constant stagnation time of 100 ± 6 ns. The deviation of the wire-array trajectory from that of a thin shell scales inversely with the ablation rate per unit mass: $f_m \propto [dm_{\mathrm{ablate}}/dt]/m_{\mathrm{array}}$. The convergence ratio of the effective position of the current at peak x-ray power is $\sim 3.6 \pm 0.6:1$, much less than the $\geqslant 10:1$ typically inferred from x-ray pinhole camera measurements of the brightest emitting regions on axis, at peak x-ray power. The trailing mass at the array edge early in the implosion appears to produce wings on the pinch mass profile at stagnation that reduces the rate of compression of the pinch. The observation of precursor pinch formation, trailing mass, and trailing current indicates that all the mass and current do not assemble simultaneously on axis. Precursor and trailing implosions appear to impact the efficiency of the conversion of current (driver energy) to x rays. An instability with the character of an $m=0$ sausage grows rapidly on axis at stagnation, during the rise time of pinch power. Just after peak power, a mild $m=1$ kink instability of the pinch occurs which is correlated with the higher compression ratio of the pinch after peak power and the decrease of the power pulse. Understanding these three-dimensional, discrete-wire implosion characteristics is critical in order to efficiently scale wire arrays to higher currents and powers for fusion applications.

DOI: 10.1103/PhysRevE.71.046406 PACS number(s): 52.59.Qy, 52.58.Lq, 52.70.Ds, 52.70.Kz

I. INTRODUCTION

Tungsten-wire-array *z* pinches [1–5] on the *Z* accelerator [5] generate a 100–220-TW soft x-ray source [2,3,5–7] when imploded in 100 ns with a 20-MA current pulse. Rapid progress has been made evaluating this source for high-yield indirect-drive inertial confinement fusion (ICF) [6–16], for radiation science [17], laboratory astrophysics [18], and other high-energy density applications [19]. Some key issues for progress relevant to fusion ignition with *z* pinches are to determine how the performance scales with drive currents [20], the proper way to scale the wire array parameters, and what factors optimize wire array performance. X-ray powers of 1–1.2 PW, for example, are needed to meet the secondary hohlraum temperature requirements of the double-*z*-pinch approach to high-yield ICF [6,8].

Simple models [19,20] and two-dimensional (2D) radiation magnetohydrodynamic [21,22] simulations predict that the radiated pinch energy should scale quadratically with the current delivered to the wire array ($\propto I^2$). Recent work has demonstrated subquadratic scaling of the radial soft x-ray power ($\propto I^{1.24 \pm 0.18}$) for the massive ($>2.5$ mg/cm) 20-mm-diam, single tungsten arrays currently used to drive the double-*z* pinch [20]. This slow scaling implies that currents considerably in excess of 60 MA would be necessary to achieve the hohlraum temperatures required for capsule ignition, if single tungsten wire arrays were scaled to higher

*Electronic address: mecuneo@sandia.gov

currents keeping a constant 95 ns implosion time. Scaling to higher powers requires further optimization of wire array performance, an identification of the many factors that affect performance, and a more fundamental understanding of the wire-array initiation, ablation, implosion, stagnation, and thermalization dynamics at higher currents. Array dynamics will also affect methods for radiation pulse shaping for ICF, and may affect both secondary hohlraum coupling efficiency [6,9] and ICF capsule drive symmetry at the ~2% level for the double-pinch ICF approach [10–13].

Implosions of high-wire number arrays at high currents (7–20 MA) have been approximated as a 2D cylindrical plasma shell (e.g., see Refs. [1,3,5,6,8,21–24]). These models implicitly assume that the wires ablate and merge on a time scale much less than the array's stagnation time on axis ($t_{\text{ablate}} \ll \tau_{\text{stag}}$). Under these conditions, the power pulse rise time is thought to be controlled by the magneto-Rayleigh-Taylor (MRT) instability in the *r*-*z* plane, growing from an initial random density perturbation (RDP) of undetermined and unspecified origin. Wire-array experiments on the ~1-MA Magpie [25–33] and the ~3-MA, Angara-5-1 [34–40] accelerators have, however, revealed a long wire ablation period ($t_{\text{ablate}} \sim 0.8\tau_{\text{stag}}$) and therefore a delay in acceleration compared to a simple 1D thin-shell implosion model [28,32,34]. A critical question has been whether these discrete-wire effects apply to high-wire-number, small wire-to-wire gap arrays at 20 MA.

The present experiments [41–44] confirm observations of a delay in array acceleration at 20 MA, even at the smallest wire-to-wire gaps typically used (209 μm). Observations and modeling show that both precursor [26,27,45–47] and trailing implosions [32,33,36] are present and that only a portion of the initial mass participates in the main implosion at 20 MA, as in experiments at low currents. Since the rate of production of x rays from a pinch depends strongly on the amount of mass and current that simultaneously assembles on axis, the result is that the conversion of current (i.e., driver energy) to x rays is less efficient than predicted by simple 1D models [19,20]. This deviation from a 1D model must be understood in order to efficiently scale to higher currents and powers needed for high-yield fusion applications. The work in this paper will aid in this understanding.

This paper is a comprehensive report of part of our efforts to understand wire-array *z*-pinch physics on the *Z* accelerator at 20 MA. Data were compiled from various experiments with the extensive *Z* diagnostic set [49], over a period of about three years. A recent paper by Stygar *et al.* [20] reports on a number of further and significant advances in the study of power scaling and shot-to-shot performance variation of wire arrays for double-*z*-pinch ICF. Other publications will describe advances made by Sinars *et al.* [50,51] for the study of wire arrays with bent-crystal-imaging x-ray backlighting. We have characterized the implosion dynamics for two of the wire arrays most frequently employed for ICF experiments: the double-*z*-pinch approach and the dynamic-hohlraum approach.

The double-*z*-pinch or double-ended hohlraum ICF concept uses 10-mm-long, 20-mm-diam single tungsten wire arrays to maximize the ratio of the radiated power (P) to the hohlraum wall area (A_h) [6–10]. This results in the highest achievable hohlraum radiation temperatures [$T_R^{3.3} \propto (P/A_h)$] [6,9] for ICF and radiation physics experiments that employ the radiation of a pinch after stagnation on axis. These arrays employ 300 11.4-μm-diam tungsten wires giving a wire-to-wire gap of 209 μm, the smallest gaps (typically) used on *Z* in any configuration. The total mass (5.9 mg/cm) implodes in 95 ns with 19 MA drive currents, yielding peak radiation powers of 125 TW [6,20]. Secondary hohlraum temperatures of 70–90 eV are obtained in configurations driving capsules with this source [6,9–13]. Rapid progress has been made on hohlraum energetics [6,9], secondary coupling [6,9,12], and radiation symmetry and capsule implosions [10,11,13]. Compressed capsule densities of 40 g/cm^3 have been achieved at convergence ratios of 14–20 [11] with this concept.

The dynamic-hohlraum ICF source achieves 150–200 eV effective drive temperatures for ICF by locating the capsules internal to a nested wire array. The collapsing array material acts as a moving hohlraum wall [14,15]. Dynamic hohlraums have recently produced imploded capsules [16] with convergence ratios of about 6. Dynamic hohlraums are also used for driving radiation experiments with the 220 eV internal temperatures, out the end of the pinch, just prior to array stagnation on axis [48]. Dynamic hohlraum arrays employ 10- to 14-mm-long nested wire arrays [3] imploding onto foam targets (with embedded capsules for ICF experiments). The 40-mm-diam outer array consists of 240 7.4-μm-diam tungsten wires giving a wire-wire gap of 524 μm and an array mass of 2 mg/cm. The 20-mm-diam inner array consists of 120 7.4-μm-diam tungsten wires, with identical wire-to-wire gaps.

Although rapid progress has been made on both of these concepts with incomplete understanding of the wire array behavior, further progress will require improved understanding of wire array dynamics.

The organization of this paper is as follows. Section II provides a summary of the experimental setup and diagnostics. We also present the measured implosion characteristics for both 20-mm- and 40-mm-diam single tungsten wire arrays. We have the most complete data set for the 20-mm array used for the double-*z* pinch [6,10]. Most of the conclusions and analysis in this paper directly apply to the 20-mm single arrays. We also present results from a 2.2-mg/cm, 40-mm-diam array, described previously [3,5], and with about the same mass per unit length of the outer array of a dynamic hohlraum. Both of these arrays show significant deviations from a 1D thin-shell trajectory model with a wire ablation period $\tau_{\text{ablate}} \sim (0.44\text{–}0.59)\tau_{\text{stag}}$, implying the existence of discrete, slowly ablating, wire cores. Results from a 12-mm-diam wire array with an ablation time $\tau_{\text{ablate}} \sim (0.68\text{–}0.74)\tau_{\text{stag}}$ are also described. This array produces the largest deviation from a thin-shell model for any array on *Z* and approaches, for the first time, the very late accelerations observed on Magpie and Angara-5-1. Most of the data from radiation emission, pinch power, electrical, and laser diagnostics are described in Sec. II, for the purpose of demonstrating discrete-wire behavior. Section II also provides comparisons of the data to a thin-shell implosion model. Some comparisons to more sophisticated 2D-radiation-magnetohydrodynamics (2D-RMHD) simulations are made in Sec. II to aid in the interpretation of some of the diagnostics.

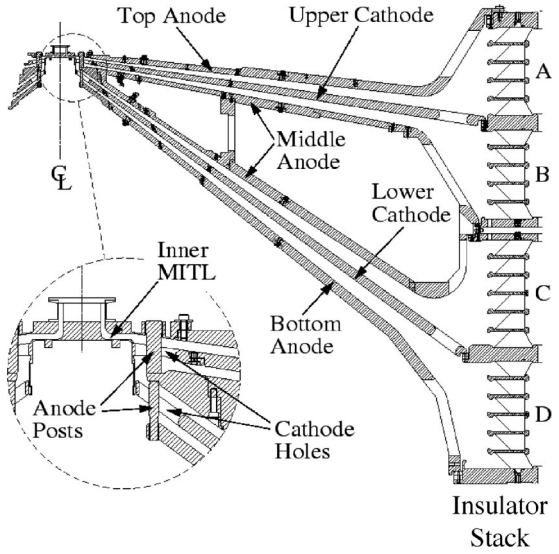

FIG. 1. Schematic of the four-level, *Z* magnetically insulated transmission line (MITL) section and plastic insulator stack (1.8 m radius). The inset shows the post-hole convolute which adds the current from the four transmission lines, with a 6-mm-wide final anode-cathode feed gap, and a typical 40-mm diam, 20-mm-long, wire array load.

The remainder of the paper compares this data with a variety of models. Section III compares the ablation period data to two different 2D-magnetohydrodynamics (2D-MHD) simulations of wire array ablation in the r-θ plane. Section IV compares the ablation, trajectory, and precursor data, and power increase during run-in, with the phenomenological rocket ablation-snowplow model of Lebedev *et al.* [32] and with results from a 1D-MHD simulation. Section IV includes trajectory scaling of wire arrays on *Z* and from lower current accelerators as a function of ablation rate per unit mass using a rocket model argument. Additional data are introduced in Sec. V for a discussion of stagnation physics including the current compression velocities and pinch stability. Section VI summarizes and provides a future outlook.

Equivalent circuit models for the *Z* accelerator are discussed in Appendix A. A glossary of symbol definitions is given in Appendix B.

II. IMPLOSION CHARACTERISTICS FOR 12-mm-, 20-mm-, AND 40-mm-diam TUNGSTEN ARRAYS

A. Experimental configuration

The electromagnetic power pulse produced by the *Z* accelerator [5] is delivered to a four-level vacuum insulator stack and four magnetically insulated transmission lines (MITL's) (Fig. 1) [52–55]. As shown in the inset, a vacuum post-hole convolute [5,52,56] connects the four MITL's in parallel to a short inner MITL that delivers power to the wire-array *z* pinch. This system can be represented as the two lumped-element circuit models [53,54] shown in Appendix A, neglecting transit time effects. Voltages are measured at the insulator stack [55]. Total currents are measured 80 cm from the wire array, prior to the post-hole convolute [55].

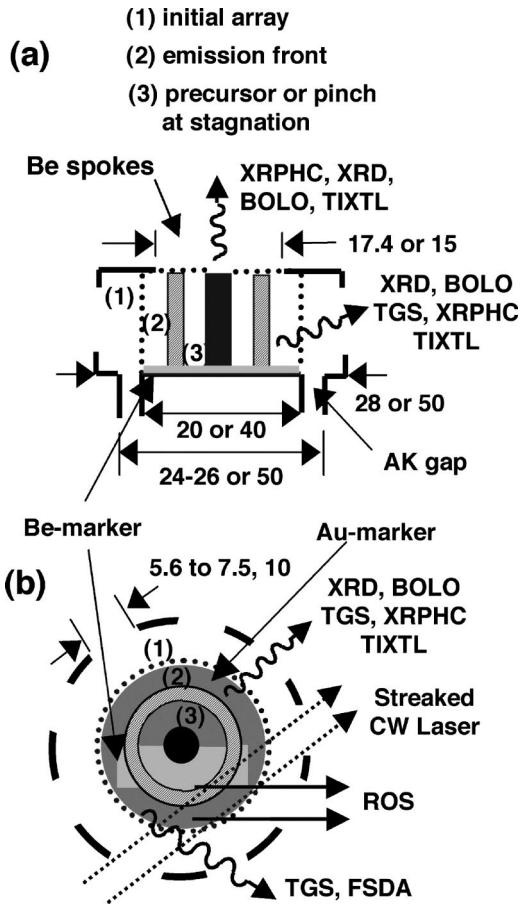

FIG. 2. Experimental wire array geometry and diagnostic lines of sight. (a) Wire array hardware in cross section shows the radial and axial diagnostic views with x-ray diodes (XRD), bolometers (BOLO), time-resolved x-ray pinhole cameras (XRPHC), transmission grating spectrometers (TGS), and time-integrated crystal spectrometers (TIXTL). The critical dimensions are given (in mm) for both 20-mm and 40-mm arrays; the 20-mm number is first. 12-mm arrays are fielded in the 20-mm hardware. Also noted is the anode-cathode (AK) power feed gap at the base of the pinch. (b) A cutaway view from the top showing the chordal lines of sight for the radial optical streak (ROS), the streaked CW laser, the TGS and filtered silicon diode array (FSDA) viewing the wires early in the pulse, and the position of the Be and Au markers for axial-self-backlighting.

Load currents are measured 6 cm from the array in the final MITL feed [55]. The voltage and current probes and circuit model are used to determine the wire array inductance during the implosion [57].

The wire-array geometry and diagnostic plan is shown in Fig. 2. The wire-array implosions are observed via radial, chordally integrating, and axially integrating lines of sight with a variety of instruments. The *Z* accelerator diagnostic suite is reviewed in Ref. [49]. The wire array is shown at its initial position (1) in Figs. 2(a) and 2(b). As the implosion proceeds, a rapidly moving radiation emission front (2) is observed on radial, chordal, and axial lines of sight. The axis of the wire array (3) (where the main implosion and any precursor implosions stagnate) is viewed with both radial and axial lines of sight.

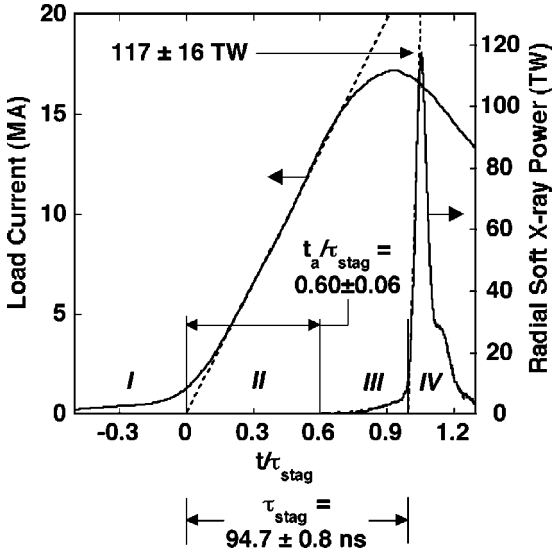

FIG. 3. Wire array load current and radiated power (average of four shots: 566, 567, 665, 667), from a typical 20-mm, 6-mg load, showing the definition of the stagnation time and the implosion phases: (I) is the wire initiation phase, (II) is the wire ablation phase, (III) the implosion or acceleration phase, and (IV) is the stagnation and thermalization phase.

The radial views are at a 12.5° polar angle through a cylindrical return-current electrode with nine slots, located coaxially with the wire array. Slot widths were 5.6 to 7.5 mm for the 20-mm array and 10 mm for the 40-mm array. Radial diagnostics are x-ray diodes (XRD's) [58] and bolometers (BOLO's) [59] for pinch power and energy. Filtered silicon diode arrays (FSDA's) [60] and transmission grating spectrometers (TGS's) [61,62] measure the wire array temperature at its initial position along a chordal line of sight, up through about 30 ns prior to stagnation. These four instruments are combined to determine the radiated pinch power back to about 60 ns prior to the pinch stagnation on axis. Pinch spectra at stagnation are measured with TGS's and time-integrated crystal spectrometers (TIXTL's) [49] on radial lines of sight. A time- and space-resolved x-ray pinhole framing camera (XRPHC) on a radial line of sight measures the structure and extent of the x-ray emission region on axis [63,20]. Optical streaks of the brightest and most rapidly moving radiation emission front are taken along chords using a fiber-optic imaging array coupled to a streak camera [64]. Time- and space-resolved shadowgraphy is obtained with a streaked cw laser (similar to the setup in Ref. [47]) in a 5-mm-wide chordal view at the array edge. This instrument is sensitive to electron density and density gradients. Axially, the radiation self-emission from the implosions is viewed through a 17.4-mm-diam Be spoke array (e.g., see Ref. [6]) for the 20-mm arrays and through a 15-mm opening in the top electrode (no spokes) for the 40-mm array. Axial diagnostics [65] include time-resolved XRPHC's, XRD's and bolometers for power and energy, and TIXTL's.

B. Implosion phases

Figure 3 shows a typical load current measurement and the pinch soft x-ray power from an average of four shots for the 20-mm array. We align the multiple x-ray power pulse curves at the time of peak power. Averaging the powers from each curve as a function of time produces the average power pulse shape. The stagnation time [66] is defined as the time interval between the linearly extrapolated leading edges (see the dotted lines) of the load current and pinch power. The stagnation time $\tau_{stag}=94.7\pm0.8$ ns for the 20-mm data in Figs. 4 and 6, 106 ± 1 ns for the 40-mm data in Fig. 7, and 100.4 ns for the 12-mm data in Fig. 5. The time axis for most of the data presented in this paper is normalized to the stagnation times.

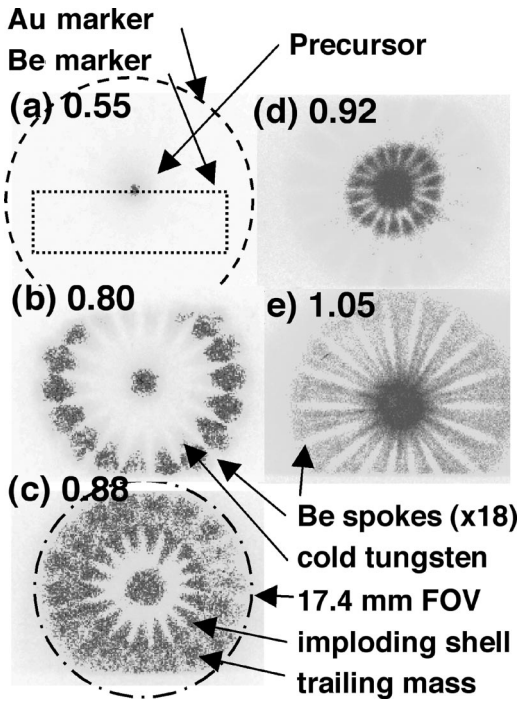

FIG. 4. (a)–(e). Axial x-ray pinhole framing camera images at various normalized times (t/τ_{stag}) during the implosion of the 20-mm-diam, 6-mg/cm wire array from shot 747. The position of the Au and Be markers are shown on part (a). The 18 Be spokes are apparent in (b)–(e). The precursor pinch is observed on axis in (a)–(d). Cold-ablated tungsten fills the center of the array in (a)–(c), obscuring the contrast between the Au and Be markers. The imploding shell implodes onto the cold-ablated tungsten at smaller radii in (b)–(d). The imploding shell has nearly merged with the precursor in (d). Trailing mass obscures the Au and Be markers in (c) and (d). The broad radial pinch profile at stagnation is shown in (e).

These data show four main phases of the implosion process as observed in previous experiments [32]. In Fig. 3 and subsequent figures, Roman numerals are used to denote the four different phases. Phase (I) is a ~50-ns wire initiation phase during the current prepulse (30–40 A/ns/wire). Based on previous single-wire experiments [67–74], this prepulse is believed to set up the initial state of the wires, prior to the more rapid wire ablation rate accompanying the higher dI/dt of the main accelerating current pulse (700–1000 A/ns/wire). Phase (II) is the wire ablation and precursor injection phase during the main current pulse. Phase (II) is defined to start (as a convenient reference point)

TABLE I. Array configurations.

Array diameter (mm)	Height (mm)	AK gap (mm)	Mass (mg/cm)	Wire number	Wire-wire gap (μm)	Wire diameter (μm)	τ_{stag} (ns)
40	20	5	2.0–2.2	240	524	7.4–7.7	106.6±1.8
20	10	1, 2, 3, 4	5.9–6.0	300	209	11.4–11.5	95.5±1.1
12	10	3	14.9	180	209	23.4	100.4

at the linearly extrapolated leading edge of the current pulse (at $t/\tau_{stag} \equiv 0.0$). Phase (III) is the wire array acceleration or implosion phase occurring onto the precursor material injected in phase (II). Phase (III) starts when the array begins to move from its initial radius and will be determined below based on emission diagnostics and electrical data. Phase (IV) is the wire-array stagnation and thermalization phase. Again, as a convenient reference point, phase (IV) is defined to start at the linearly extrapolated leading edge of the pinch power (at $t=\tau_{stag}$). During phase (IV), the kinetic energy of the incoming array and the magnetic energy stored near the axis of the pinch system are converted into radiation and the pinch power rises rapidly to peak in 3–6 ns, after which the radiation pulse rapidly terminates.

This paper presents data and models primarily for phases (II) and (III). Initial conditions and material properties chosen for the 2D-MHD models allow inference of some properties of wires at the end of the initiation phase (I). Understanding the behavior during these three phases that comprise the first 97% of the wire array's history is an essential prerequisite because these set up the "initial" conditions for the thermalization processes near the axis.

Presently, however, few direct measurements have been made that can experimentally verify the various physical processes and conditions proposed for the rapid rise (and fall) of the radiation pulse during phase (IV), e.g., the discrete wire ablation process at the array edge [25,27,32] and the MRT instability [21–23], both of which can spread the imploding shell, coupling and conversion of ion kinetic and magnetic field energy at stagnation [22,23,75,76], subsequent electron heating and radiation rates [77], and termination of the pulse by MHD instabilities of the compressed pinch on axis [33].

The wire-array configurations used in these experiments are summarized in Table I. Hence forth we refer to the arrays by their diameter. Various array implosion trajectory data are presented in Figs. 4 and 6 for the 20-mm array and in Fig. 7 for the 40-mm array. Figure 5 compares array acceleration times obtained from electrical data for 40-mm-, 20-mm-, and 12-mm-diam arrays. In Fig. 4, we present evidence for the formation of a precursor pinch on the axis of the array obtained with an axial x-ray pinhole-framing camera and for cold-ablated tungsten plasma filling the center of the array.

C. Phase II: Precursor pinch formation

Figures 4(a)–4(e) show axial XRPHC images (~250 eV) at five times on the normalized time scale, for the 20-mm-diam array. These data were obtained looking axially down along the pinch with a 17.4-mm-diam field of view (FOV) in the top electrode. The spatial resolution was about 200 μm. The XRPHC gives the axially integrated, radial spatial profile of the x-ray power. Camera gate widths were 2 or 4 ns. These images were obtained through a structure in the top electrode consisting of 18 radial Be spokes (one spoke and 16.7 wires every 20°), similar to those used in double-pinch ICF work [6]. Each of the spokes (200 μm by 250 μm in cross section) ends 1.5 mm from the axis. These spokes act as a transparent electrode, conducting current to allow the pinch to implode to the axis, preventing axial acceleration of the pinch plasma, and allowing a view of the imploding pinch through low-opacity material [6]. The spokes cause no measurable change in the wire array stagnation time to the axis or to the pinch power pulse shape and amplitude compared to shots with a solid top electrode [6]. The individual spokes are most clearly visible in Fig. 4(e) at peak power ($1.05\tau_{stag}$) when increasing radiation has burned through the ablated Be spoke material.

We observe a 1.5–3-mm full width at half maximum (FWHM) hot region on axis at $>0.50\tau_{stag}$ which is defined to be a plasma precursor [26,27,35,45–47]. The precursor persists in all frames. We have not looked earlier in time than $0.5\tau_{stag}$. Thus, material may have arrived earlier. Similar axial pinhole camera data for the 40-mm array (not shown) indicate a precursor on axis at $>0.36\tau_{stag}$ [78]. Again we did not look earlier than this time. We observe an imploding shell-like object in the axial view with the XRPHC [Figs. 4(b), 4(c), and 4(d) for the 20-mm array]. Figure 4(b) is the first frame for which the 2–3-mm-wide imploding shell has moved completely within the 17.4-mm FOV.

The data in Fig. 4 also represent an axial, self-backlighting experiment, utilizing reemission of the electrode at the bottom of the wire array. The pinch implodes on the surface of a 20-mm-diam electrode coated with 10 μm of gold [Figs. 2(b) and 4(a)]. A 50-μm thick, rectangular beryllium marker [5 mm × 16 mm, Figs. 2(b) and 4(a)] was placed over this Au surface. One-dimensional radiation burn-through calculations with a 2D-RMHD code [79] indicate the Au and Be would not burn through until $1.07\tau_{stag}$, after peak power. The higher albedo of the Au compared to the Be would provide a factor of 1.7–2.9 emission flux contrast during the period $(0.50–1.02)\tau_{stag}$, as measured in the axial pinhole camera. The contrast between this Be marker and the Au-coated electrode at the bottom of the array could, in principal, be observed between the Be spokes in Fig. 4(b). Lack of observed contrast (or emission of any kind) in experiments with both 9 (not shown) and 18 spokes (as shown) indicates that the center of the array is filled with a cold, high-opacity material.

Previous experiments have shown precursor formation on the axis of wire array implosions [26,32,35,45–47]. Related

modeling shows that a precursor can arise from $\mathbf{J}\times\mathbf{B}$ accelerated wire coronal material collecting on axis, inertially confined by impinging plasma streams from each wire [27,29,30]. In these simulations, the wires form a heterogeneous, core-corona structure. High core resistivity and high corona conductivity shunts current into the corona, leading to a slow core ablation rate and long-lived wire cores, and a delayed motion. Simulations of the ablation phase (II) in 2D (Sec. III) show that a 10–30-eV, $\sim$0.1–10-mg/cm^3 tungsten plasma is ablated and accelerated into the center of the array. This tungsten has sufficient opacity, and the electrode reemission temperature is such that it will not burn through on a 100-ns time scale, consistent with the axial-self-backlighting observations.

The presence of a hot x-ray emitting region on the axis is not, strictly speaking, sufficient to distinguish between models of wire array implosions. Two-dimensional RMHD simulations of imploding shells (e.g., those done for calculations presented in Fig. 9(a), discussed in Sec. II G 2), show that the magnetic piston launches a rapidly moving, low-density material off the inner surface of the shell ($\sim 10^{-5}$ g/cm^3), which reaches the axis quite early. However, a hot emitting region on the axis, coupled with a low-opacity region between the axis and the edge of the array, *and* a delayed acceleration of the edge of the array (both the emissive regions and the current, described next) is sufficient to establish that this hot region on the axis arises from the ablation of stationary wire cores and is a plasma precursor as observed in lower-current experiments. It also implies a distribution of ablated wire material between the precursor and wire array.

D. Phase II: Array acceleration times

The clearest demonstration of a delay in wire array acceleration, and thus a long wire ablation phase (II), is provided by the electrical data. The time-dependent convolute voltage $V_{\mathrm{conv}}(t)$ is derived from the measured insulator stack voltages and MITL currents using an equivalent circuit model for the four-level *Z* transmission lines, described in Appendix A [Fig. 24(a)]. The convolute voltage reflects the time-dependent impedance of the transmission line feed (out to about 6 cm from the load) and the wire array. In one method of determining the convolute voltage, we average the voltage from each level of the four-level transmission line on *Z*, deriving the results in Fig. 5. In a related method [57], used below in Sec. II E to derive inductances in Figs. 6 and 7, we assume that the currents from each transmission line level are equal at the convolute. The two methods give very similar results for $V_{\mathrm{conv}}(t)$. The circuit model inductances, voltages, and current probes were calibrated for consistency with a static short-circuit load [57]. Convolute voltages directly measured by an inductive-wire probe agree with those calculated from the stack voltage, MITL currents, and circuit model, to within 10%, giving confidence in our methods.

If we neglect resistive effects that occur (presumably) early in the pulse and assume that the array voltage results from a purely inductive load, we can write the post-hole convolute voltage as follows:

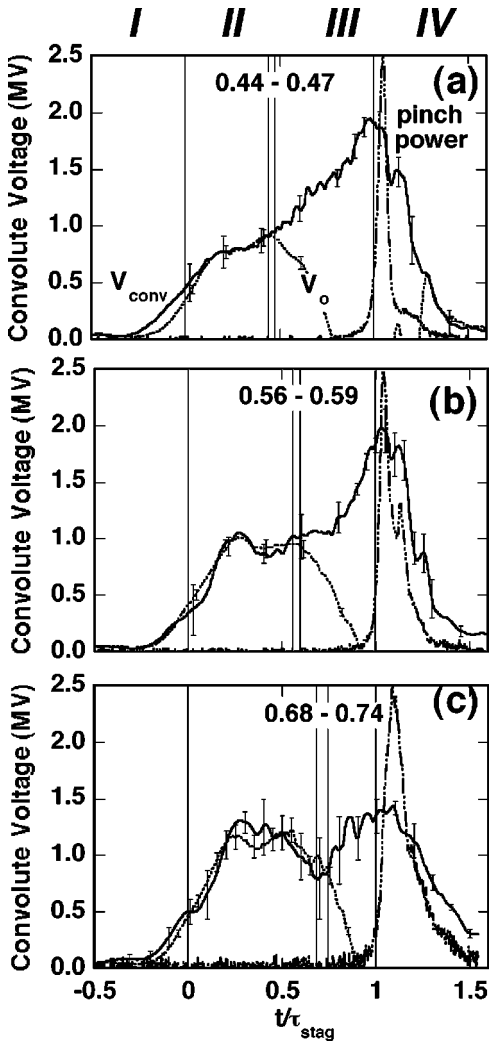

FIG. 5. Comparisons of convolute voltages $V_{\mathrm{conv}}(t)$ (solid lines) with initial voltages $V_0(t)$ (dotted lines) indicating the times of array acceleration when $V_{\mathrm{conv}} > V_0$ for (a) 40-mm- (shot 846), (b) 20-mm- (shot 818), and (c) 12-mm-diam (shot 931) wire arrays. The pinch power pulseshapes (dashed lines) are shown for reference. The acceleration time is later in the pulse for heavier, smaller diameter arrays.

$$V_{\mathrm{conv}}(t) = (L_{\mathrm{feed}} + \delta L)\frac{dI_\ell(t)}{dt} + \frac{d}{dt}[L_a(t)I_\ell(t)]. \qquad (1)$$

In this expression, L_{feed} is the constant initial transmission line inductance downstream of the convolute in the final MITL feed gap (without the array), I_ℓ is the measured load current, and $L_a(t)$ is the time-dependent array inductance. The inductance δL is a small correction to account for current convection inside the initial array radius via the ablated plasma precursor observed in 2D-MHD simulations [35,80–82] prior to array motion. Current convection is estimated to increase the inductance of the wire array by 0.17 nH/cm assuming that 57% of the array current is convected into the interior of the array as in a static analytic MHD model [35,82] for wire array equilibria and is uniformly distributed over the entire diameter. Two-dimensional

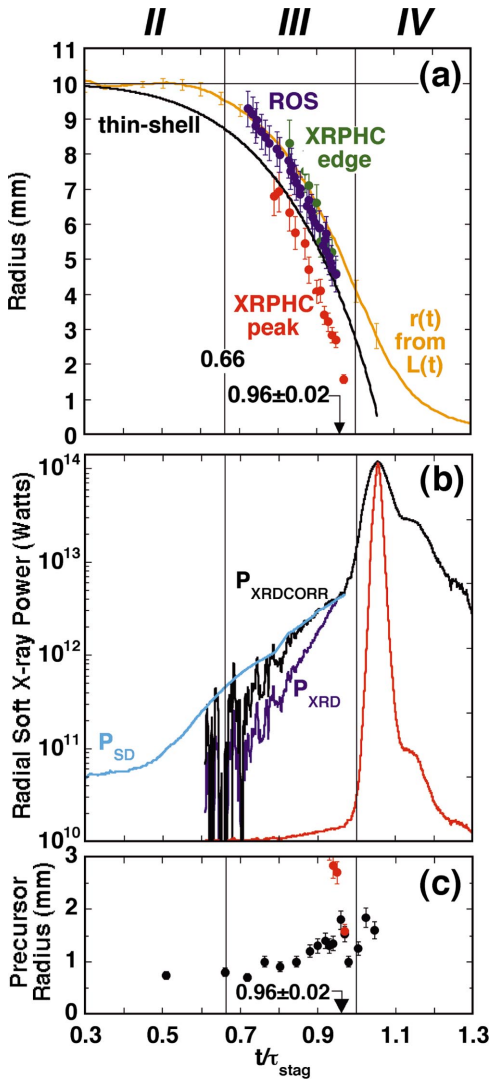

FIG. 6. (Color) Data from a 20-mm-diam, 6-mg/cm array showing (a) array trajectories versus normalized time (t/τ_{stag}) from four methods. Trajectories are from a radial optical streak [ROS, blue circles, typical of four shots (665, 674, 684, 747), shot 674 shown], the edge of the x-ray pinhole framing camera radial profile (XRPHC edge, green circles, from shots 728, 747), and the peak of the moving shell from the radial profile (XRPHC peak, red circles, from shots 728, 747) and from the inductance unfolds (orange line, average of three shots: 724, 817, 818), compared with a thin-shell model (black line). Trajectory data show the delayed start of acceleration with respect to a thin shell (black line) but earlier arrival at the axis (red circles) than a thin shell and the current (orange line), indicating trailing mass and current. (b) Radial pinch power from two different measurements: x-ray diode's (P_{XRD}, the blue line is average of shots 566, 567, 665, 674, the black line is corrected for slot collimation), and silicon diode (P_{SD}, light blue, average of shots 198, 199). The pinch power is on a log scale (left axis) and a linear scale (in red, right axis). (c) Precursor radius (black circles, from shots 728, 747) and XRPHC peak (red circles from shots 728, 747).

MHD simulations discussed in Sec. III show that 30%–40% of the array current is convected into the interior of the array, resulting in a smaller correction. This correction is a maximum of 0.2–0.3 nH for these arrays in steady state, once the

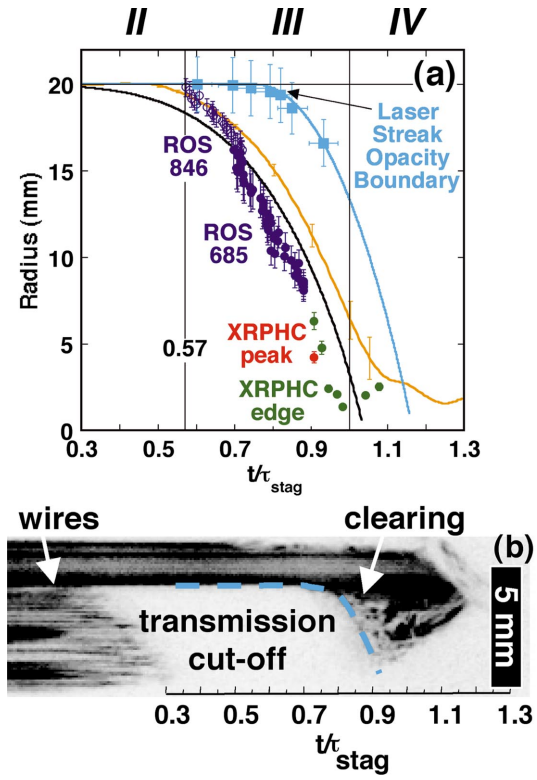

FIG. 7. (Color) Data from a 40-mm-diam, 2.2-mg/cm array showing (a) array trajectories versus normalized time (t/τ_{stag}) from the same four techniques as in Fig. 6. The radial optical streak (ROS) is a composite obtained on shots 685 and 846. Inductance unfolds are from shot 846. As for the 20-mm array, trajectory data show delayed acceleration with respect to a thin shell (black line) but earlier arrival at the axis than a thin shell (red and green circles) and the current (orange line), indicating trailing mass and current. (b) Streak shadowgraphy (and fitted trajectory in light blue) from a 532-nm laser transmission through the edge of the array on shot 846, showing the individual wires early, transmission cutoff, and the gradual clearing of the lower density trailing plasma at the edge later. Where unmarked, curves are the same as in Fig. 6.

precursor mass reaches the axis of the array. This is only 5%–10% of the inductance inside the convolute. Prior to the precursor mass and current reaching the axis, the correction is much smaller than this. This inductance correction therefore results in a voltage much smaller than the typical ±15%–±20% error in $V_{conv}(t)$.

Prior to array motion, the array inductance is fixed and $dL_a/dt=0$. Setting $dL_a/dt=0$ in Eq. (1), the initial convolute voltage is given by

$$V_0(t) = [L_{feed} + \delta L + L_a(t_0)]\frac{dI_\ell(t)}{dt}, \qquad (2)$$

where $L_a(t_0)$ is the constant initial inductance of the wire array load. Both L_{feed} and $L_a(t_0)$ are determined by the initial geometry of the transmission line and array hardware. The load current $I_\ell(t)$ is measured. The initial convolute voltage $V_0(t)$ can therefore be calculated as described by Eq. (2). The time-dependent convolute voltage with changing array inductance, $V_{conv}(t)$, described by Eq. (1), is determined from

independent measurements at the accelerator insulator stack, as noted. These two voltages V_{conv} and V_0 diverge when $dL_a(t)/dt \neq 0$.

Figure 5 compares the convolute voltages $V_{conv}(t)$ with the initial measurement $V_0(t)$ for 40-mm-, 20-mm-, and 12-mm-diameter arrays. The soft x-ray pulse shapes are shown for reference. Early in the pulse prior to array motion, V_{conv} (solid lines) agrees with V_0 (dotted lines) over a long plateau in the initial load impedance. The time when $dL_a(t)/dt \neq 0$ and $V_{conv}(t) > V_0(t)$ is clearly evident in Fig. 5. There is sometimes a clearly discernable resistive phase [see Fig. 5(a)] where $V_{conv}(t) > V_0$ early in the pulse. We chose times that are clear inflection points in both the convolute voltage and initial voltage to give an error range in determining when the array inductance changes.

Acceleration begins at $\tau_a = (0.44–0.47)\tau_{stag}$ for the 40-mm array in Fig. 5(a), at $\tau_a = (0.56–0.59)\tau_{stag}$ for the 20-mm array in Fig. 5(b), and at $\tau_a = (0.68–0.74)\tau_{stag}$ for the 12-mm array in Fig. 5(c). These times define the end of the wire ablation phase (II) and the start of the implosion phase (III). The long plateau with $dL_a/dt = 0$ clearly shows that high-wire-number arrays on *Z* have a long wire array ablation phase during which the wires are stationary at their initial positions. Thin-shell trajectories would show a resolvable acceleration in the period $(0.3–0.4)\tau_{stag}$. The 40-mm array accelerates closest to the thin-shell model. What is remarkable about these results is that the time of acceleration is later in the pulse for the smaller-diameter, heavier arrays.

The change in acceleration times is likely related to mass ablation rates. We increased the wire array mass as the array diameter decreased to keep the implosion time constant (Table I). The wire ablation rate does not appear to increase as rapidly as the mass is increased. Thus the ablation rate per unit mass is actually smaller for smaller-diameter arrays and the time of acceleration later. The peak voltage and rate of rise of voltage decrease as the radius of the array decreases, indicating a slower implosion.

These represent the first results showing scaling of the wire array acceleration time. A key feature of earlier observations of wire array trajectories was a delayed acceleration of the edge of the array compared to a thin-shell model, corresponding to a long wire ablation phase. Arrays on the Magpie [25] and Angara-5-1 [34] accelerators, at 1–3 MA, begin movement at $\sim(0.76–82)\tau_{stag}$. However, for both the 20-mm and 40-mm arrays on *Z*, the beginning of acceleration deviates less strongly from the thin-shell trajectory, beginning acceleration at $(0.44–0.59)\tau_{stag}$. This difference implies that the ablation rate per unit mass of the *Z* wire arrays is larger than on Magpie and Angara-5-1, the wires ablate faster and burnthrough earlier in the pulse, and the implosion begins earlier. The shorter pulse length of the current drive on *Z* (88 ns to peak) may be an important factor in increasing the ablation rate on *Z* in comparison with Magpie (250 ns to peak). The heavy, small-diameter, 12-mm array approaches the very late beginning of acceleration observed with wire arrays on Magpie and Angara-5-1. The small-diameter array on *Z* behaves similar to the heavy, smaller-diameter arrays (8 mm) studied on Angara 5-1 that also show a delayed implosion, even with a short current drive (70 ns to peak).

The scaling of trajectories on *Z* for the 40-mm, 20-mm, and 12-mm arrays gives confidence that wire array acceleration times can be scaled because all the data were taken on the same accelerator, with the same methods. The ablation rate per unit mass and its relationship to scaling of the acceleration time are discussed further in Sec. IV D.

E. Phases II and III: Array acceleration times and implosion trajectories

Once the wire cores ablate and burn through, possibly at axially nonuniform locations [25,26,28,32,33,35–40], the implosion starts, beginning phase III. Four different methods are used to determine the array implosion trajectory. Three are based on spatially resolved optical or x-ray emission, and one is based on electrical data. Array implosion trajectories obtained from the four techniques are plotted on the normalized time scale in Figs. 6(a) and 7(a).

One-dimensional axially and chordally averaged, radially resolved optical (400-nm) streaks (1D-ROS) view the implosion from the side, through slots in the current return electrode (see Fig. 2). We plot the trajectory of the peak intensity of this visible emission as blue circles in Figs. 6(a) and 7(a). We also plot the trajectory of the peak and edge of the imploding shell-like object observed in the axial XRPHC [as in Figs. 4(b), 4(c), and 4(d) for the 20-mm array, composite of two shots]. The outer edge of the moving x-ray shell is plotted as green circles, while the peak intensity is plotted as red circles [both shown in Figs. 6(a) and 7(a)].

Time-dependent load inductances are derived by a method described in Ref. [57]. Equations (1) and (2) are subtracted and integrated to derive $L_a(t)$ directly. Again, the circuit model inductances, voltages, and current probes were calibrated for consistency with a static short-circuit load. The measured plateau of constant initial inductance [at $L_a(t_0)$] is averaged over 20–40 ns, and the time of acceleration is given by the deviation from this initial plateau. The acceleration times are within 2–3 ns of those from the method of the previous section.

The mean or effective radius of the current sheath radial profile is calculated from the inductance. Inductance errors of ±10% lead to absolute errors of from ±15 to ±20% in the radius because the conversion from inductance to radius involves an exponential relationship. The array current radius $R_{cur}(t) = R/\exp[\Delta L_a(t)/(2\ell)]$, where R is the initial array radius, $\Delta L_a(t)$ is the calculated change in inductance from the initial plateau in nH [$\Delta L_a(t) = L_a(t) - L_a(t_0)$], and ℓ is the array length in cm. The error in the current radius shown on Figs. 6(a) and 7(a) is the error based on the shot-to-shot variation in the average of $R_{cur}(t)$ for three identical shots. The shot-to-shot variation in the average $R_{cur}(t)$ is smaller than the absolute errors in $R_{cur}(t)$ from the errors in the electrical data.

Linear extrapolation of the 1D radial optical streak trajectory to the initial array radius is used to define the end of the wire-array ablation phase (II) and the beginning of the implosion phase (III). (ROS data are not available between 9.5 and 10 mm for the 20-mm array.) A 1D thin-shell model [black lines Figs. 6(a) and 7(a)] assumes that the mass is

TABLE II. Acceleration times from electrical and ROS data.

Array diameter (mm)	t_a/τ_{stag} (electrical) Sec. II D	t_a/τ_{stag} (electrical) Sec. II E	t_a/τ_{stag} (ROS)
40	0.44–0.47	0.47 ± 0.02 (six shots)	0.57
20	0.56–0.59	0.55 ± 0.03 (six shots)	0.66
12	0.68–0.74	0.74 (one shot)	NA

concentrated in a shell at the initial radius and accelerated from the beginning of the current pulse. The beginning of load inductance increase (decreasing mean current radius) agrees to within 10 ns with the extrapolation of the 1D-ROS. The outer edge of the 20-mm array [Fig. 6(a)] begins to move at $(0.55\pm0.03)\tau_{stag}$ [from $L_a(t)$, average of six identical shots] to $0.66\tau_{stag}$ (extrapolated optical emission location from 1D-ROS, typical of four shots) and deviates from the thin-shell model by ~15–20 ns at the initial radius of 10 mm. With the 40-mm array, the ROS trajectory data are a composite obtained on two shots and are available out to the 20-mm initial array radius. The implosion phase begins at $(0.47\pm0.02)\tau_{stag}$ [from $L_a(t)$, average of six identical shots] to $0.57\tau_{stag}$ (emissive, 1 shot) for the 40-mm array [Fig. 7(a)]. The beginning of the load inductance increase agrees to within 7 ns with the 1D-ROS.

Hence both the 20-mm and 40-mm arrays have an extended ablation period $\tau_{ablate}\sim(0.44–0.66)\tau_{stag}$ confirmed by both emissive and current diagnostics. The earlier acceleration time for the 40-mm compared to the 20-mm array was also confirmed by both diagnostics. No optical streak data were obtained with the 12-mm array because the visible emission from the delayed trajectory merged with that from the power increase during the implosion. Table II summarizes acceleration times obtained from both electrical methods and the radial optical streaks.

The ROS emission trajectory accelerates inward ~7–10 ns later than the current front for both arrays. This difference is not understood. The size of the inductance increase required appears to be larger than the maximum possible effect caused by current convection into the center of the array. We assume that the implosion of the brightest front observed with the optical streak represents the location where current heats some rapidly moving mass. One possibility is that the wire cores could carry some current and begin to move prior to complete wire core burnthrough. Complete core burnthrough at some axial locations [28,32] is possibly associated with the more rapid and bright implosion observed with the ROS. This difference might also be a signature of nonuniform ablation at the array edge [28]. Axial modulation of the ablation rate leads to an axially periodic perturbation of the wire cores [28]. Current flows along the perturbed surface prior to acceleration, increasing the inductance. The ROS gives an image integrated over the array length and the boundary remains stationary until the wire cores burn through at some axial locations. Once the wire cores burn through completely, the current does not follow the perturbed core surface but penetrates into the array interior [32], and the ROS shows the start of the implosion. A different starting time for acceleration and different implosion velocities are evidence for 3D effects on wire array trajectories, discussed more completely in Sec. III G.

Wire ablation times are compared with the predictions of 2D MHD simulations in Sec. III and with phenomenological models in Sec. IV.

F. Phase II-IV: Pinch power and precursor expansion data

The pinch power ramps up from ~0.05 to 5 TW during phases II and III as the pinch implodes [Fig. 6(b)]. Radiated powers of >1–3 TW are observed while the array radius $r(t)\sim(0.8–0.5)R$, well away from the axis. Radiated power that ramps up during the implosion phase, well before final stagnation, was observed on Magpie and was proposed as a possible signature of interaction with and snowplow accretion of preablated wire material [19,32,33,83,84]. We describe two methods to determine the pinch power during the implosion phase, at powers of <5% of peak.

The pinch soft x-ray pulse shape is measured with an XRD. The pinch power is determined by normalizing these pulse shapes to the pinch energy measured with a fast bolometer. This method is in agreement with absolute unfolds of filtered XRD data to within ±20% in flux at peak power [6,48]. An average of four 20-mm shots is shown in Fig. 6(b) [$P(t)_{XRD}$, blue line]. The pinch power measurement is done through a 7.5-mm-wide slot in the electrode. Prior to $\sim0.95\tau_{stag}$, regions of the radiating mass are at a diameter larger than the slot width. The power is therefore corrected for collimation of the diagnostic viewing slot [48] assuming a Lambertian emitter **(**$P(t)_{XRDCORR}=[R_{piston}(t)/3.75]P(t)_{XRD}$, black line**).** This correction uses a radius from a rocket model [32] trajectory fit, $R_{piston}(t)$, shown on Fig. 15(a) (Sec. IV B).

The pinch power is also estimated from a pinch brightness temperature measurement, $T_P(t)$, with a filtered silicon diode array [12] [P_{SD}, light blue line, Fig. 6(b)], e.g., $P_{SD}(t)=2\pi R_{piston}(t)\ell\sigma_B T_P^4(t)$ where $R_{piston}(t)$ is again the rocket model trajectory, ℓ is the pinch height, and σ_B is the Boltzmann radiation constant. The XRD power corrected for geometric collimation nearly agrees with that estimated from the pinch temperature measurement. The sensitivity of the XRD (filtered with 4 μm Kimfol) to the soft x rays falls off rapidly at radiation temperatures below 60 eV. This might account for the underestimate of the filtered XRD measurements compared to that of the silicon diode. The error in these estimates of power, prior to $0.93\tau_{stag}$, is $(+30\%,-50\%)$. The combination of silicon diode and XRD measurements gives a composite pinch power history over the last 60 ns of the implosion history.

The power increases from 0.05 to 0.4 TW during the ablation phase (II), equivalent to a ~15–30-eV wire region temperature. During the implosion phase (III), the power increases from 0.4 to 5 TW. The radiated power for 40-mm wire arrays (not shown) also ramps up in a similar way from 0.1 to 6 TW during phases (II) and (III), prior to final stag-

nation. All primary and secondary hohlraum temperature histories observed on *z*-pinch-driven hohlraums show a foot on the drive from the pinch radiation during the implosion run-in phase (III) [6,10]. If this foot pulse can be measured accurately, understood, and controlled [33,84], it may be possible to harness this radiation to generate a foot pulse for the isentropic compression of ICF capsules.

Figure 6(c) shows the half width or radius of the precursor as a function of time from the XRPHC. The diameter is initially stable over a period of about 20 ns, from the time it is first observed. The precursor starts to expand at $\sim 0.75\tau_{\mathrm{stag}}$, just after the implosion phase starts, as also observed in previous experiments on Magpie [26,32]. Precursor expansion correlates with the increase of the power during run-in. A model for the precursor expansion is presented in Sec. IV E. This model balances the thermal pressure of the precursor against the incoming kinetic pressure of the ablated ions. The precursor expansion occurs because of absorption of run-in radiation. The increase of precursor temperature and thermal pressure leads to an increase in the precursor equilibrium radius [32].

The end of the implosion phase (III) and the beginning of the stagnation phase (IV) are approximately when the peak of the accelerating shell from the XRPHC [red circles, Figs. 6(a), 6(b), and 7(a)] strikes and merges with the expanding precursor. This occurs at $(0.96 \pm 0.02)\tau_{\mathrm{stag}}$ for the 20-mm and $0.92\tau_{\mathrm{stag}}$ for the 40-mm array, about 4–8 ns prior to the rapid power increase at the start of phase (IV), which is, by definition, at $1.0\tau_{\mathrm{stag}}$. The precursor radius appears to compress at the start of stagnation in Fig. 6(c). At stagnation, the power pulse may begin to increase with the compression and shock heating of the precursor plasma by the incoming mass and current [32,33]. Several models of the pinch power increase during implosion will be presented in Sec. IV.

G. Phases III and IV: Trailing current and mass data

Direct measurements of the trailing mass have been made on Magpie at 1 MA and Angara-5-1 at 3 MA with laser imaging diagnostics. For example, fingers of trailing mass are observed to extend to the initial array radius at stagnation on Magpie [32]. One definition of trailing mass would therefore be mass distributed between the axis and initial radius at stagnation. Recent measurements on Angara-5-1 [35] indicate that 54% of the current resides at a radius $>R/2$ for a heavy 20-mm-diam array, at stagnation. Again, R is the initial array radius. Features of these data have been reproduced with both 2D [35] and 3D MHD [85] simulations. Trailing mass and current are fundamentally three-dimensional issues, are probably related, and will impact the scaling of radiated pinch power with mass and current.

The trailing mass appears to result from axially nonuniform ablation of the wire cores [32,35]. The origin of the trailing mass is unknown and a subject of active investigation. Regions of the core that ablate through first, implode, and allow more slowly ablating regions to trail behind the implosion front or implode at a slower rate. This process may create an effectively wider imploding sheath, distributing the mass and current over a larger radial extent. The distributed mass may also allow a shunting path for some of the current at larger radius [86–88], bypassing the main implosion. Current shunting at larger radius would reduce the convergence or compression ratio of the current. Sinars *et al.* have observed axially nonuniform ablation of wire arrays on *Z* with bent-crystal radiography [50,51].

Aspects of trailing mass observed in these experiments are mass distributed outside the radius of the brightest emission regions, mass distributed well outside the effective position of the current sheath out to the edge of the array early in the pulse while the implosion is underway, or mass detected at a radius 50% larger than the effective position of the current sheath at stagnation. Aspects of the trailing current observed in these experiments are an effective radius of the current sheath well outside the radius of the brightest imploding front, as well as current distributed over a significant fraction of the initial array radius.

1. Three-dimensional implosion characteristics and trailing current

The trajectory of the outer edge of the axial XRPHC profile [green circles, Fig. 6(a)] agrees with that from the chordal 1D-ROS [blue circles, Fig. 6(a)], for the 20-mm array. Early in the implosion phase, the effective radius of the current profile also agrees with that determined for the outer array edge from both these emission diagnostics (ROS and XRPHC) for the 20- and 40-mm arrays. There is, however, a progressively larger deviation between the effective radius of the current and that of the emissive regions [e.g., the peak of the XRPHC, red circles, Figs. 6(a) and 7(a), or ROS, blue circles, Fig. 7(a)]. These deviations become apparent at an array radius $r(t) \leqslant R/2$ for the 20-mm array and $r(t) < 0.8R$ for the 40-mm array.

The brightest and most rapidly moving emission feature [the peak of the XRPHC shell, red circles, Figs. 6(a) and 7(a)] arrives on the axis well ahead of the thin-shell model [black line, Figs. 6(a) and 7(a)] and ahead of the mean position of the current [orange line, Figs. 6(a) and 7(a)]. Delayed acceleration of and earlier arrival of the peak of the XRPHC compared to the thin-shell model and the current indicates that it is not carrying the entire initial array mass or current at the moment it first arrives at the axis. This means that there must be current and mass distributed at radii outside this brightest and most rapidly moving front. As noted, the ROS data [blue circles, Figs. 6(a) and 7(a)] appear to have a delayed start of acceleration compared to the current. The trajectory of the ROS also crosses over the current and thin-shell trajectory [in particular in Fig. 7(a)], indicating it does not carry all the mass or current. These observations all require a 3D explanation. We refer to this mass and current as "trailing" without specifying either its quantity or actual radial distribution.

We hypothesize that the visible 1D-ROS and electrical data show the position of the outer edge of an optically thick object, while the axial diagnostics detect features moving internal to the outer, optically thick edge of the imploding *z* pinch. For the 40-mm array, with only 37% of the mass per unit length of the 20-mm and a lower optical depth, the ROS data may not entirely coincide with the outer edge of the

imploding mass at smaller radii [see Fig. 7(a) where the radius of the ROS is less than the radius of the effective current position].

The velocity of the peak of the emission layer at the axis (40 cm/μs) is significantly larger than the velocity of the ROS (24–33 cm/μs) or the current (28 cm/μs) (see Sec. V A). The different velocities are evidence consistent with an axially inhomogeneous implosion. This bright front may be a shock launched into the precursor plasma by the magnetic piston at the moment the acceleration starts. Lebedev *et al.* first observed this shock, in an axial view of aluminum wire-array implosions [32]. Shocks may not be observed if the precursor plasma temperature is too high [89]. The bright front may also correspond to the implosion of the array at some axial locations prior to others, because of axially nonuniform ablation [32,33]. The heating by this shock and/or heating and snowplow accretion by the magnetic piston may contribute to the power increase during the implosion phase (see Sec. IV D).

At stagnation, the effective radius of the current, determined from the inductance unfolds [57], is more than twice as large as that for the brightest radiation emission observed radially. The radius of the current at peak power is $R_{cur} = 2.8 \pm 0.4$ mm for the 20-mm array [average of six identical shots, from the database of Ref. [20], with anode-cathode (AK) gaps of 3 and 4 mm], corresponding to a diameter of 5.6 ± 0.8 mm. The convergence ratio of the current (CR $= R/R_{cur}$) is $3.6 \pm 0.6:1$ [Figs. 6(a) and 16(a)]. This is significantly less than the $\geqslant 10:1$ typically inferred from x-ray pinhole camera measurements of the size of the brightest radiating region at peak power [3,5,89]. This is discussed more completely in Sec. II G 4.

This effective radius is calculated assuming that the inductance of the imploding wire array can be represented as a collapsing thin shell in a concentric return-current conductor. This provides a physically meaningful result, since the resulting radius, as a function of time, is well behaved and monotonically decreasing. This technique does not give information on the profile of the current, without further assumptions. There could be current distributed both inside and outside the effective radius. Since the inductance $L_a \sim \ln(R/r)$, most of the current is distributed inside this effective radius. The observation that the current converges to a factor of 2 larger radius than the brightest emission region on axis again indicates trailing current, even at stagnation, near the axis.

Load currents are measured 6 cm from the wire array, prior to the final, smaller AK gap at the base of the wire array (see Figs. 1 and 2). Anode-cathode gap current loss at the base of the array might lead to systematic errors in interpretation of the electrical data as a lower inductance. Larger load currents (smaller convolute voltages) can be produced by both a resistive path in parallel with the pinch inductance (e.g., AK gap or convolute current loss) [22,23,6] or by trailing current (e.g., a lower pinch inductance). If one assumes that the current flow results only due to load inductance and there is actually AK gap or convolute current loss in parallel, a mistakenly larger current radius and smaller convergence ratio would result. Also, if the pinch were resistive at stagnation and we neglected this effect, the decrease in load current would look like a smaller radius of current and a larger convergence ratio.

We unfold electrical data from 20-mm arrays [Fig. 6(a)] with the largest AK gap (3 or 4 mm), for which the radiated power and energy no longer increase with increasing AK gap [20]. However, this could simply indicate that current loss across the 3- or 4-mm gap has become small and fixed, not necessarily zero, leading to some small but systematic error in determining the radius of the current. We also caution that the load current measurements may have a somewhat larger systematic error beyond peak. Despite these caveats, we interpret the electrical data from 20-mm arrays after the peak of the current at $\sim 0.8\tau_{stag}$ as a strong indication of trailing current (current outside the radius of brightest emission) because the mean current radius shows reasonable agreement with the ROS and XRPHC edge measurements down to $r(t) \geqslant 0.5R$ (at $t \leqslant 0.95\tau_{stag}$), well beyond peak current. Also, other observations, discussed below, directly or indirectly indicate trailing mass.

By comparison with the 20-mm data, the 40-mm AK feed gap has an $\sim$40% weaker initial magnetic insulation of the feed gap and, hence, possibly more current loss in parallel with the load inductance compared to the 20-mm array. [The magnetic insulation of the feed gap scales as $d(t)/R$, where $d(t)$ is the time-dependent AK gap.] The 40-mm current radius values [Fig. 7(a)] may therefore underestimate the convergence ratio relative to the 20-mm array. The radius of the compressed current is 4.2 mm at peak power, for the 40-mm array, which corresponds to a CR of 4.7:1. This is a larger current radius at stagnation than for the 20-mm array. Soft x-ray pinhole camera measurements in the radial direction, however, typically show a smaller FWHM of the brightest emitting regions at peak power for the 40-mm arrays (1.5 ± 0.2 mm, CR=26.7:1; see Ref. [3]), compared to the 20-mm (1.7 ± 0.2 mm, CR=11.8:1; see Ref. [20]), which suggests a tighter pinch. Also, axial XRPHC data (not shown; see Ref. [78]) indicate a tighter compression of 40-mm (6.9:1) compared to the 20-mm (4.7:1). Larger AK gaps (8–10 mm) are recommended to increase magnetic insulation and test for systematic effects of current loss on inductance unfolds for larger diameter arrays.

2. Trailing mass: Axial diagnostics

As an indirect test for trailing mass, we utilized the thick Be and Au foil reemission markers on the electrode at the bottom of the 20-mm pinch as described in Sec. II C. Recall that 1D radiation burnthrough calculations indicate that these foils would provide a factor of 1.7–2.9 reemission contrast between $0.50\tau_{stag}$ and $1.02\tau_{stag}$. Two-dimensional RMHD simulations of tungsten array interaction with the electrode surface show a maximum Rosseland mean optical depth of tungsten left behind on the electrode of $\tau_R \sim 0.1$–0.3 (total for both the upper and lower electrode surfaces). The lack of observable contrast between the Au and Be at large radii after the shell has moved by [Figs. 4(c)–4(e), $t \geqslant 0.85\tau_{stag}$] therefore indicates that the emission is not coming from the bottom electrode, but from the emission of hot trailing mass which appears to extend to the limit of the field of view.

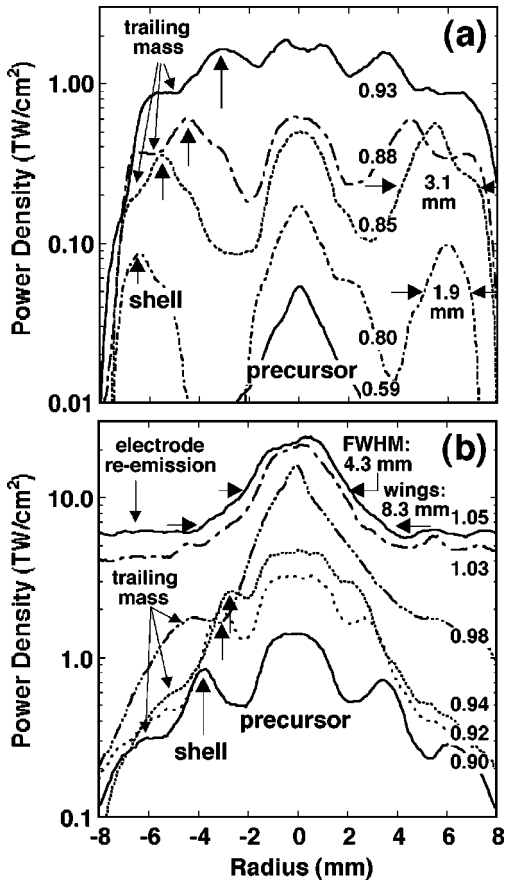

FIG. 8. Radial profiles of axial x-ray pinhole framing camera images (from Fig. 4, for the 20-mm array from shot 747), plotted as power density (TW/cm^2) by normalizing the images to the measured axial power from an x-ray diode and bolometer. The numbers on the curves are normalized times (t/τ_{stag}). (a) used 4-ns gates between $0.58\tau_{stag}$ and $0.93\tau_{stag}$; (b) used 2-ns gates between $0.90\tau_{stag}$ and $1.05\tau_{stag}$. The error is ±20% in power density. The precursor is observed on axis. A 1.9–3.1-mm FWHM shell-like object implodes onto the precursor. A plateau of hot trailing mass is observed outside the shell between $0.85\tau_{stag}$ and $0.98\tau_{stag}$. The radial extent of the pinch at peak power ($1.05\tau_{stag}$) is very broad.

Radial profiles of x-ray intensity are obtained from the axial XRPHC data shown in Fig. 4. Axial XRD's and bolometers normalize the radial intensity profiles [65,78], giving the power density profiles shown in Fig. 8(a) and 8(b). Early in the pulse, we see a precursor radiation brightness temperature of ~25–30 eV. The moving shell feature, with a width of 2–3 mm, enters into the axial view at $0.76\tau_{stag}$. The material on axis at the center of the collapsing region, including the precursor, heats up. The precursor broadens as the implosion proceeds [Fig. 6(c)]. Shell widths are difficult to extract later in the implosion because of the broadening of the precursor, the heating of material in the center, and the shelf or plateau at large radius. Nevertheless, it appears that the shell does not widen as the implosion proceeds and may actually narrow (possibly from snowplow mass accretion; see Sec. IV D). The moving shell eventually merges with the precursor region at $0.96\tau_{stag}$ [Fig. 6(c)]. The precursor reaches a brightness temperature of 75 eV just prior to merger. The increase of the precursor temperature prior to merger is qualitatively similar with the model of precursor expansion in Sec. IV E.

A shelf or plateau (labeled trailing mass) is observed on the XRPHC radial emission profile at a radius larger than that of the ~2–3-mm FWHM moving shell for $>0.85\tau_{stag}$ [Figs. 8(a) and 8(b)]. The radius of the edge of these profiles [given in Figs. 6(a) and 7(a) as the green circles] is well outside the peak of the moving shell [given in Figs. 6(a) and 7(a) as the red circles]. The edge radius, however, coincided with the effective position of the current [orange lines on Figs. 6(a) and 7(a)]. The mean position of the current is at a larger radius than the brightest and most rapidly moving front. As noted, the lack of contrast between the Au and Be markers implies that this emission cannot be from the bottom electrode surface. Further evidence that this plateau must be hot mass, trailing in the wake of the imploding shell or mass imploding more slowly, is provided by a calculation of the maximum possible reemission flux of the bottom electrode.

For this calculation, we assume the system is a hohlraum with no plasma fill other than a tightly compressed *z* pinch on the axis driving the system (e.g., a so-called vacuum hohlraum [7]). The measured pinch powers [Fig. 6(b)] are used in a 0D hohlraum power balance model [9,90]. We calculate a conservative (maximum possible) bottom electrode reemission temperature given the range in error for the measured powers and wall albedo.

We find that the plateau of the x-ray emission at the edge of the distribution has a from 2.1 ± 0.9 to 4.1 ± 1.8 greater reemission flux than the maximum possible bottom electrode of the equivalent vacuum hohlraum would have, between $0.85\tau_{stag}$ and $0.98\tau_{stag}$. This is independent and strong evidence that the emission comes from hot plasma in the hohlraum at large radius, and *not* the bottom electrode. The ratio increases from 2.1 ± 0.9 to 4.1 ± 1.8 in the period from $0.85\tau_{stag}$ to $0.93\tau_{stag}$ as the trailing mass heats. Between $0.93\tau_{stag}$ and $1.05\tau_{stag}$ (about 11 ns) the ratio falls from 4.1 ± 1.8 to 0.9 ± 0.2 as the trailing mass either moves out of the way and implodes or burns through with the rapidly rising pinch power at stagnation.

Some mass appears to trail to the edge of the field of view ($r=0.87R$) between $0.85\tau_{stag}$ and $0.90\tau_{stag}$ and at least 2–4 mm behind the moving shell between $0.94\tau_{stag}$ and $0.98\tau_{stag}$. At stagnation, the full width of the emission profile is 8.3 mm [Fig. 8(b)], implying some mass located out to 4.2 mm, 50% larger than the effective position of the current. If this mass has a large magnetic Reynolds number ($R_m=\mu_0 v l/\eta$, where μ_0 is the permeability of free space, and v, l, and η are some characteristic fluid velocity, length, and resistivity, respectively), there could be current frozen into this mass, out to 4.2 mm.

At peak power, the reemission flux of the plateau is equal to that from the hohlraum model (a ratio of 0.9 ± 0.2), consistent with the measured power and calculated albedos. Near peak power, the hohlraum indeed behaves as a vacuum hohlraum. This conclusion is consistent with previous work that confirmed the energy balance and secondary coupling of these systems at peak pinch power, to within ±20% [6,9,12]. Prior to peak power, as well as for smaller diameter secondaries [12], we may not be able to neglect pinch plasma

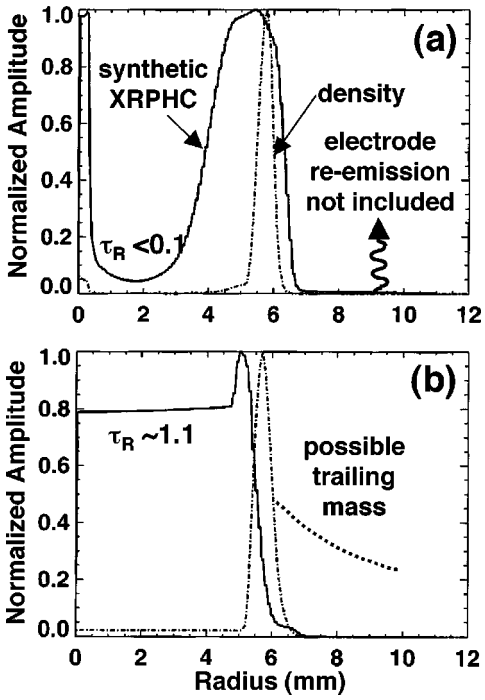

FIG. 9. Radial profiles of the density (dashed lines) and corresponding synthetic axial x-ray pinhole camera (XRPHC) images (solid lines) from 2D(*r*-*z*)-RMHD simulations of a 20-mm, 6.0-mg array seeded by random density perturbations (RDP) for (a) a shell-like implosion with a 1% RDP and (b) a shell implosion onto a uniform, cold, prefill with 25% of the array mass, with a delayed trajectory and with a 4.5% RDP. τ_R is the Rosseland opacity of the material located radially between the axis and imploding shell, when viewed axially.

blocking the entrance to the hohlraum and its potential impact on secondary coupling [12] and capsule drive symmetry for ICF applications [11–13].

Direct interpretation of the radial profiles from the axial XRPHC is difficult because of radiation transport integrated along the length of the pinch implosion system and because of an *a priori* unknown mass and temperature distribution. Figure 9 gives two illustrations of this issue in 2D(*r*-*z*)-RMHD simulations of imploding shells. A multigroup radiation diffusion treatment was used (28 groups spanning from 10 eV to 10 keV logarithimically). These are not intended to be exact simulations of the implosions, but to incorporate different elements as approximate model problems as a guide to interpreting the axial XRPHC data. Although we suspect that 3D models are ultimately required, the 2D simulations have the most advanced radiation transport models and are our best tool at present.

The Eulerian simulations were run in the *r*-*z* plane. The array was initialized as a 1-eV, 1-mm-wide, 6-mg, tungsten shell. A random density perturbation (RDP) of this initial shell is used to initiate the growth of the 2D-MRT instability [21–23]. This instability spreads the mass out during the implosion. The size of the RDP is chosen (in the conventional or classical manner as in Refs. [21–23]) so that the peak power, risetime, and FWHM of the actual power pulse at stagnation during phase IV are reproduced. The 1-mm shell compresses to 0.5 mm under acceleration by the magnetic pressure. Synthetic XRPHC profiles are then produced which account for axial radiation transport, motional blur during the XRPHC gate widths (2–4 ns), and XRPHC filter response. In general, these effects broaden the x-ray image and shift the peak of the x rays to a somewhat smaller radius ($\sim$0.2–0.9 mm) compared to the width and peak of the imploding density profile.

Figure 9(a) is a simulation of the implosion of a 1.0-mm tungsten shell. Figure 9(b) is a simulation of the implosion of a 1.0-mm shell with delayed acceleration to approximate a wire ablation period and incorporating a uniform prefill, with 25% of the initial array mass. The shell mass is decreased to 75% of its initial mass to approximate a decrease from wire ablation and precursor injection. The acceleration history of this simulation was modified to begin at $0.6\tau_{\mathrm{stag}}$ as in the experiment. The size of the RDP required to produce agreement with the power pulse was a factor of 3–5 larger for the delayed trajectory with the uniform prefill. The increase in the RDP is consistent with a lower integral number of linear MRT growth times [30,41] for a delayed trajectory with a higher acceleration and lower mass. Delayed trajectories that have an overall higher average acceleration—e.g., those of the inductance or the emission (see Sec. IV B) compared to the thin shell—have a 25%–30% lower number of linear MRT growth periods [$\sim\int\sqrt{ka(t)}dt$, where k is the MRT wave number and $a(t)$ the array acceleration] and therefore increased stability. In addition, a pinch that accretes mass during the implosion (see Sec. IV D) could be more stable to the MRT compared to a simulation without a prefill [21,32,91–94].

At a radius of $r(t)\geqslant 0.65R$ (at $t\leqslant 0.85\tau_{\mathrm{stag}}$) the density from the simulations has not broadened significantly beyond the 0.5 mm width produced initially, for either case. In Fig. 9(a) (pure shell implosion) the simulation shows a low-opacity (Rosseland optical depth $\tau_R<0.1$) material inside the collapsing shell, accelerated at high velocity down to the axis. A low-density, hot, precursor-pinch-like feature is also observed on the axis [Fig. 9(a)], a possibility we noted in Sec. III C. Were the opacity this low in the center of the array, the contrast between the Be and Au markers should be visible internal to the array in Fig. 4(a) Figure 9(b), however (shell implosion onto a cold 10–30 eV, uniform tungsten prefill), shows a high-opacity material inside the collapsing shell ($\tau_R\sim 1.1$), similar to what is observed in Fig. 4. We did not include a precursor pinch region on the axis of this simple model of ablated material in Fig. 9(b).

Neither simulation included trailing mass or electrode re-emission [see Fig. 9(a)], which accounts for the rapid falloff in the synthetic XRPHC profiles at large radius. This is in contrast with the plateau of bright emission at large radius that we concluded was from pinch plasma emission. The plateau of bright trailing mass, an example of which is added schematically in Fig. 9(b), therefore indicates a broad gradient of plasma, trailing off toward the initial array radius. This is inconsistent with the steep gradient at the outer edge produced by the implosion of an MRT unstable 2D shell with an RDP selected to match the power pulse width at stagnation [Fig. 9(a)].

The difference between the peak of the moving shell [XRPHC, red circles, Fig. 6(a)] and the radius of the outer edge [1D ROS, XRPHC, blue or green circles, Figs. 6(a)] or current [orange lines, Fig. 6(a)] gives a measure of the shell width. The shell is wide initially [$\sim$1.9–2.8 mm FWHM, from Fig. 6(a), 1.9–3.1 mm FWHM from Fig. 8(a)] at large radius $r(t) \sim (0.8–0.75)R$ [corresponding to times $t \sim (0.80–0.85)\tau_{stag}$]. Based on the two model 2D-RMHD problems, at these times and radii, only about 0.3–0.9 mm of this width results from broadening due to radiation transport and motional blur during the camera gate pulse. Two-dimensional MRT in the conventional or classical sense (e.g., Refs. [21–23]), with the RDP adjusted to match the power pulse [pure shell case, Figs. 9(a)], will only significantly broaden the apparent shell width in the XRPHC view to $\geqslant$2 mm later in the implosion as the array gets closer to the axis, $r(t) < 0.5R$ (at $t > 0.9\tau_{stag}$). Two-dimensional MRT therefore does not appear to be a factor broadening the shell at large radius, based on these simulations. The remaining width at large radius may reflect axially nonuniform wire ablation and axially nonuniform implosion at the array edge, as observed at smaller currents [26,32]. Axially nonuniform ablation and implosion could create an effectively wider imploding object by the end of the ablation phase.

The comparisons of data and this 2D-MRT model are presented to indicate that the conventional or classical MRT picture does not describe the observed large initial shell width. These 2D-RMHD simulations also do not include trailing mass, trailing current, a realistic prefill density, temperature or current profile, or azimuthal effects on instability growth and are not very good approximations of the further development of single-array implosions. Trailing mass and current imply that 3D models are required to appropriately model powers during run-in and at stagnation. Lacking a 3D wire ablation model and imaging diagnostics we cannot be more specific about contributions of 3D-MRT, motional blur, radiation transport, nonuniform ablation, and trailing mass to the width of the shell observed with the XRPHC or at stagnation. X-ray radiography [50,51] and time- and space-resolved spectroscopy data are needed to truly interpret these x-ray emission profiles in detail.

At peak power [$1.05\tau_{stag}$, Figs. 4(e) and 8(b)], the FWHM of the emitting region is 4.3 mm, when viewed axially. The width of the profile at the level of the electrode reemission temperature is 8.3 mm, indicating a very broad object with significant wings. The on-axis peak power density [$\sim$21 TW/cm^2, from Fig. 8(b)] corresponds to a 120 eV brightness temperature. The FWHM of the hot radiating region at stagnation is 1.7 ± 0.2 mm (CR=11.8:1 from analysis of five shots from the database of Ref. [20] at full current, with available x-ray pinhole camera data) when observed radially (averaged along the axial direction), with a time-resolved x-ray pinhole camera (measured at $\sim$250 eV) [63,20]. The radiated power of $\sim 124 \pm 15$ TW [20] corresponds to a 220 ± 6 eV surface brightness temperature when assumed to be emitted from a 1.7-mm-diam cylinder.

This suggests that the sources viewed by the axial and radial instruments are quite different. In addition, the radial XRPHC data show low-temperature wings on the emission profile, with a width of 4–5 mm, discussed in Sec. II G 4 below. Time-integrated crystal spectroscopy continua (measured between 1 and 1.8 keV) also indicate that the axial and radial source spectra are different. Average spectral continua brightness temperatures observed axially ($\sim$120–170 eV, over a 4–2-mm diameter) are lower than those observed radially ($\sim$250 eV, over a 2-mm diameter). The axial crystal spectroscopy also suggests the presence of a smaller-diameter hotter core within the larger-diameter softer emission.

3. Trailing mass at the array edge: Chordal diagnostics

The transmission front of a 532-nm cw laser through a chord at the edge of the 40-mm array is observed on a streak camera [Fig. 7(b)]. This instrument gives a direct measure of the trailing mass. These data show individual wires early in the implosion, consistent with a wire ablation phase (I) [$(0.15–0.30)\tau_{stag}$]. Transmission is then cut off by increasing refractive gradients and absorption ($n_e \sim 10^{18}$–10^{19} cm^{-3}). During the period that transmission is cut off (between $0.3\tau_{stag}$ and $0.85\tau_{stag}$), emission and current diagnostics show that the implosion is well underway. Thus there is a significant density of material left at radii between 15 and 20 mm even while the current and emission front are rapidly imploding toward the axis. The reappearance of laser transmission well after the edge of the array has begun imploding ($>0.8\tau_{stag}$) is consistent with plasma densities $n_e \sim 10^{17}$–10^{18} cm^{-3}, containing at most a few percent (0.5%–5%) of the array mass trailing near the initial radius at peak x-ray power. Again, if this mass has a large magnetic Reynolds number, some current would be frozen in.

The observation of a rapidly imploding front with emission and current diagnostics, while the laser diagnostic is cut off, suggests axial inhomogeneity of implosion. As Fig. 7(b) shows, once the density has dropped allowing transmission, the plasma is highly nonuniform axially and turbulent. These data also imply that mass is distributed (with some unknown profile) between the axis and initial radius of the array at peak power. This suggests that the outer edge of the mass distribution is not as sharply defined as for a 2D-MRT unstable pinch [Fig. 9(a)], as we concluded based on the axial XRPHC profiles (Fig. 8).

A spread out mass distribution is consistent with Sasorov's 2D-MHD model of the trailing current observed at Angara-5-1 [35]. These simulations produced a density profile that falls off slowly toward the initial radius. The trajectory of the clearing front [blue squares, Fig. 7(a); dotted line, Fig. 7(b)] is extrapolated to the axis assuming 0.5% of the mass and 10% of the current [light blue line, Fig. 7(a)] and appears to arrive during the tail of the power pulse, reaching the axis at $\sim 1.15\tau_{stag}$. This trajectory is also consistent with larger mass at larger currents—e.g., 5%–15% of the mass at 30%–50% of the current.

Observations of trailing mass or a very broad imploding shell are clearly related to the observations of trailing current. The laser shadowgraphy data demonstrate that even for the lightest array, with the earliest wire burnthrough and acceleration (the highest ablation rate per unit mass; see Sec. IV F), some mass lags at least 5 mm behind the effective current front. It is unknown to what extent these electron

densities of 10^{17}–10^{19} cm^{-3} (and the corresponding ion densities of 10^{16}–10^{18} cm^{-3} for an average ion charge state $\bar{Z} \sim 10$) at the edge of the array actually impede the rate of current transfer to the axis and impact the array performance at peak power. These data point to behavior earlier in the implosion that spread out the mass and possibly could limit the convergence of the mass and current at stagnation. Estimates of the clearing time or the time it takes different quantities of trailing mass to compress or accelerate inward are given in Sec. IV B.

4. Broad mass profile at stagnation: Radial diagnostics

The trailing mass near the edge of the array during the implosion can influence the mass profile near the axis at stagnation. Data from a time and space-resolved XRPHC viewing the pinch in the radial direction through the diagnostic slots give information on the spatial structure, uniformity, and radial extent of the pinch within 3 mm from the axis. The data are obtained with two different x-ray filters on the same shot. Data from shot 665 are shown in Fig. 10. These data were obtained with a 64-μm-pinhole-limited spatial resolution and a 100-ps gate pulse. Motional blur is estimated to be about 25 μm. The total spatial resolution is 70 μm. Figures 10(a)–10(e) show images from 4.8 μm Kimfol and 193 Å of aluminum ("soft" filter). Figures 10(f)–10(i) show images from 4.8 μm Kimfol with 1313 Å of aluminum ("hard" filter). The thicker aluminum filter attenuates emission below the carbon edge (284 eV) by an additional factor of 6–60 depending on the energy.

Comparing the images from the two filter levels, we observe a large diameter cold halo surrounding a hotter core region. The "core" consists of 5–15 hot regions or "hot spots" of varying sizes. Some of the hot spots could be overlapping and not individually discernable. The halo emission is effectively suppressed with the somewhat thicker Al filter. Al filters at least 1300 Å thick effectively stop UV and VUV radiation, and are also known to be pinhole free, effectively preventing the transmission of visible light.

In Figs. 10(b)–10(d) the structure of the hot spots and the shape of the intensity contours (white lines) appear to show an instability with an $m=0$ sausage character growing up rapidly during the rise of the pinch power. Figure 10(d) appears to indicate the formation of a mild $m=1$ kink instability, just after peak power. The kink instability is never observed before peak power in any framing data. We also observe in Figs. 10(c) and 10(d) the presence of a number of "bubble" regions labeled "b1" through "b3," defined for this discussion as a cold region surrounded by hot material. These aspects of Fig. 10 will be discussed in Sec. V B.

The times corresponding to each image for Fig. 10 are given with respect to peak radiated x-ray power rather than normalized to the stagnation time. Peak power is at $1.05\tau_{\mathrm{stag}}$. Figure 10(d), obtained 0.2 ns ($1.052\tau_{\mathrm{stag}}$) after peak x-ray power, shows cold material trailing outside of the hotter core region at a 2- to 3-mm radius, almost out to the edge of the slot in the electrode. Figure 11(a) compares axially averaged, radial profiles from the soft filtered data in Figs. 10(a)–10(e). The FWHM rapidly decreases from 5.2 mm, 6.6 ns prior to peak power ($0.98\tau_{\mathrm{stag}}$), to 1.3 mm, 2.4 ns after peak power

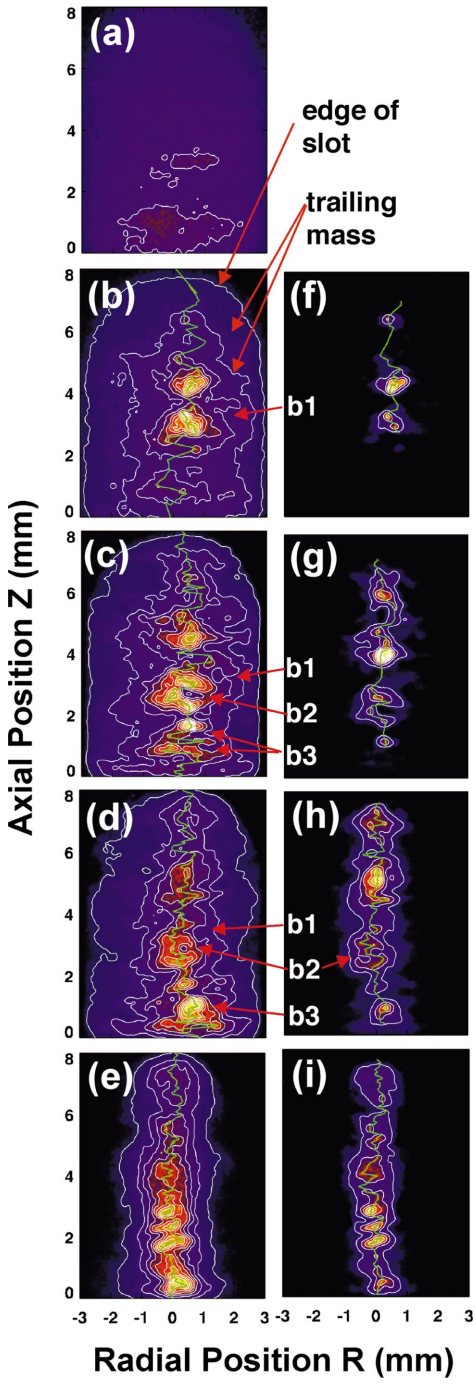

FIG. 10. (Color) X-ray pinhole camera data with a radial view of the pinch (normalized exposure) from shot 665: pinhole images were filtered with 4.8 μm Kimfol and 193 Å aluminum in parts (a)–(e) and with 4.8 μm Kimfol and 1313 Å aluminum in parts (f)–(i). Times are given as time with respect to peak radiated power, rather than normalized to the stagnation time. Part (a) was obtained at 6.6 ns prior to peak power, parts (b) and (f) at −4.6 ns, parts (c) and (g) at −1.1 ns, parts (d) and (h) at 0.2 ns, and parts (e) and (i) at 2.4 ns. The images all use the same color table. Cold material surrounds a hot core region in (a)–(e). Only the hot core is observed with the thicker filter in (f)–(i). "Bubble" regions (cold material surrounded by hotter material) are labeled b1, b2, and b3.

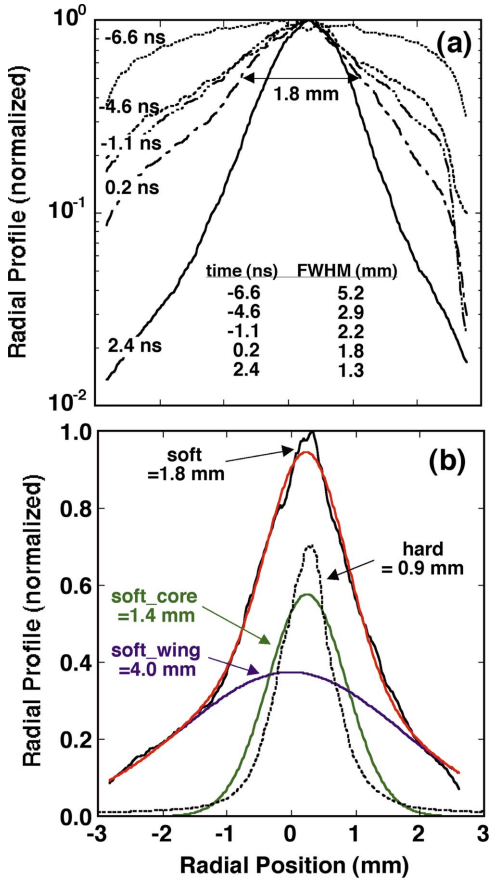

FIG. 11. (Color) (a) Axially averaged, normalized radial x-ray exposure profiles from Figs. 10(a)–10(e). Times given are with respect to peak radiated x-ray power in ns. (b) Normalized soft-filtered (solid black line) and hard-filtered (dotted black line) radial profiles at 0.2 ns [Fig. 10(d)]. The soft-filtered profile is fit by the sum of two Gaussians, showing a wing (blue), a core (green), and the total (red). Numbers on the plots are the FWHM. The pinch reaches maximum compression after peak power.

($1.084\tau_{stag}$). The intensity of the wing drops from 20% to 10% of the peak intensity between −1.1 ns and 0.2 ns ($1.039\tau_{stag}$–$1.052\tau_{stag}$), corresponding to about 50% of the peak temperature. The radial profile observed at 2.4 ns ($1.084\tau_{stag}$) falls quickly to 1% of peak, indicating little or no wing compared with earlier times.

Peak radial compression of the self-emission is after peak power [Figs. 10(e) and 10(i)], in agreement with the trajectory of the current [Fig. 6(a)]. Since wall reemission peaks about 1.5 ns after peak pinch power [6], the rapid decrease of the profile implies that the emission is not wall reemission from the inside of the electrode or emission from the edge of the diagnostic viewing slot, but the emission of trailing mass. Also, wall reemission would result in a flat plateau at large radius, not a rapidly decreasing profile. We cannot observe whether these wings extend beyond the edge of the 6-mm-wide diagnostic slot.

The FWHM of the profile from the hard filtered images [Figs. 10(f)–10(i)] actually increases from 0.5 to 0.9 mm between −4.6 ns ($\sim 1.0\tau_{stag}$) and 0.2 ns ($1.052\tau_{stag}$), as the compression and heating proceeds. This is consistent with the growth of the diameter of the stagnation region after $0.98\tau_{stag}$, observed in the axial XRPHC [Fig. 6(c)].

The series of radial profiles from the soft filter in Fig. 11(a) implies a compression time scale of about 9 ns for the mass located between 2 and 3 mm from the axis. The trailing mass either continues to implode or burns through and becomes optically thin. If interpreted as implosion, the velocity is ~(0.2–0.25) cm/9 ns or ~22–28 cm/μs, about equal to the effective implosion velocity of the current observed at a similar time [see Fig. 21(b), Sec. V A].

Figure 11(b) compares the axially averaged, radial profiles of the soft- and hard-filtered pinhole images near peak power. The hard profile is normalized to the peak intensity of the soft profile. The soft profile is fit with the sum of two Gaussians: one with a FWHM of 4.0 mm representing the wings and one with a FWHM of 1.4 mm representing the core hot-spot region. The FWHM of the core fit is somewhat larger than that of the corresponding hard-filtered profile (0.9 mm), but about that of the soft-filtered profile 2.4 ns after peak power (1.3 mm). We speculate that these wings on the mass profile at stagnation may result from the trailing mass profile near the outer edge of the array earlier in the implosion history.

We normalize the radial XRPHC images to the measured pinch power at that time, determined with the radial XRD and bolometers. The result is converted to radiation brightness temperatures assuming each pixel in the image acts as a cylindrical Planckian emitter. This procedure is only intended to be an approximate, visual aid, but has some physical content. We neglect emission integrated over one optical depth into the pinch boundary (a Milne boundary condition) and assume that the emission simply comes from a surface emitter. We also neglect the XRPHC filter response, assuming that the normalized exposure just gives some appropriate and flat weight of the contribution of each pixel to the total radiation.

Figure 12(a) shows the brightness temperature distribution for Fig. 10(d), obtained just after peak power. Figure 12(a) is essentially Fig. 10(d) plotted on a logarithmic color scale. The wings are more clearly shown as temperature. We observe halo region brightness temperatures of 50–150 eV and core region brightness temperatures of 150–300 eV. Figure 12(b) gives a 3D representation of the data, showing very clearly the broad wings of the low-temperature trailing mass.

The 4–6 mm extent of the wings at peak power is consistent with the diameter of the effective position of the current (5.6 ± 0.8 mm). The data are also consistent with the effective diameter of the pinch from the axial XRPHC (4.3 mm FWHM) and with the 8.3 mm maximum extent of the wings [Fig. 8(b)]. The wings on the radial profile are observed in all images with soft filtering. The detection sensitivity to wings on the profile is enhanced in the axial view [Fig. 8(b)] because of integration along the 10-mm length of the system. The wings are more difficult to detect in the radial view because of a decreased integration path length, increased axial nonuniformity, and decreased optical depth due to heating by the hot core.

Other published radial XRPHC data taken with soft filters show wings on the radial profile [3]. Some previously published XRPHC data show only a small, tightly pinched core,

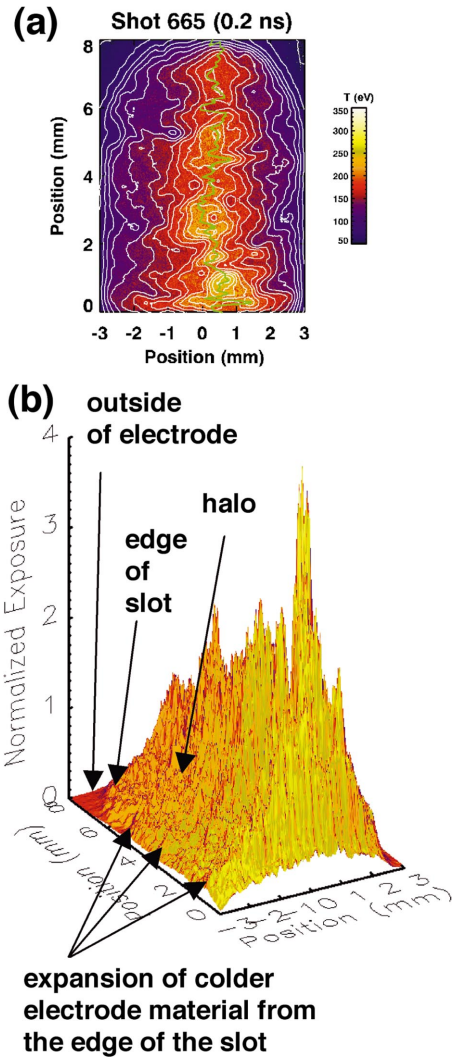

FIG. 12. (Color) (a) Temperature distribution obtained from normalizing shot 665 radial x-ray pinhole camera image [0.2 ns after peak power, Fig. 10(d)] with the measured radial power and (b) 3D representation of the 2D image. The broad wings of the colder halo, the outside edge of the slot in the current return electrode, and the cold slot material expanding from the slot edges in a few places are clearly seen.

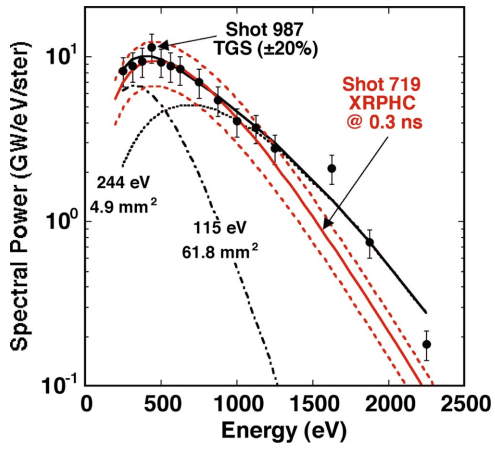

FIG. 13. (Color) Spectral power from a wire array at peak power, viewed radially with a transmission grating spectrometer from shot 987 (circles with ±20% error bars). Unfolds assume the superposition of two Planckian distributions (dashed and dotted black lines) possibly representing a cold halo and hotter core. The red lines (dashed lines show ±35% error range) are the equivalent pinch spectrum obtained from normalized radial x-ray pinhole camera data from shot 719 (0.3 ns after peak power), using the same method as for Fig. 12(a).

because of the use of thicker Be filters which transmit only radiation above 1 keV [5,89]. For example, in the case of the data in Figs. 10(f)–10(i) with the thicker Al filter, the FWHM at peak power is <1 mm, implying a convergence ratio of $>10:1$.

Sometimes, bright spots observed in the hard filtered images [e.g., the three observed at the top in Fig. 10(h)] are dimmer in the softer filtered images [Fig. 10(d)]. This indicates cooler halo material in the path between the camera and bright spot or surrounding the hot spot. Detection of halo emission is reduced with the hard filter. Since the figures have the same color table and are each normalized to their respective peaks, the relative emission of the regions of the image containing hot spots increases.

The intensity of the pinch emission is not uniform with length. Calibrations of the nonlinear XRPHC instrument gain with pinch length were taken into account for the data in Fig. 10. The pinch appears brightest near the cathode in Figs. 10(c)–10(e) ($z=0$ mm). The intensity falls as the pinch nears the anode. Although the last 2.2 mm of the pinch nearest the anode is not observed in Fig. 10, the data are consistent with the trend towards a lower temperature observed for the anode end of the pinch in the axial XRPHC data of Fig. 8. The hottest spots, observed radially, appear to be at least 3–5 mm from the end of the pinch, perhaps preventing their observation in the axial XRPHC.

Measurements of the pinch spectral power density were made between 0.2 and 2.3 keV with a transmission grating spectrograph (TGS), in the radial direction [61,62]. The spectra at peak power are shown in Fig. 13, from shot 987. The TGS spectral resolution and accuracy are sufficient to resolve a spectrum well fit by the sum of two Planckians [6,62]. The radiated soft x-ray power at peak is estimated to come, partly (37%) from a 115-eV source with a $\sim$60-mm^2 emitting area, and partly (63%) from a 244-eV source with a $\sim$5-mm^2 emitting area for the 20-mm array. The area of the low-temperature spectral component is an upper bound because of 10%–20% flux contamination from electrode reemission at a Planckian temperature of 80–90 eV.

The 12-times-smaller area of the hot area compared to the colder area is either consistent with emission from hot spots or a hot core. We know from the radial XRPHC images that the core region consists of a number of hot spots of varying sizes. Assuming cylindrical emission areas, the equivalent FWHM of the cold halo is 5–6.2 mm, while that for the hot core is 0.5 mm. The power emitted by the halo may simply be reemission of cold material at larger radii, pumped by the hot-core emission.

An equivalent pinch emission spectrum (red lines, Fig. 13) was produced from the radial XRPHC image from a nominally identical shot at peak power (shot 719), converted

TABLE III. Summary of pinch radiation brightness temperatures and sizes for 20-mm arrays.

Diagnostics	Energy range of measurement	Axial view	Radial view
X-ray pinhole camera X-ray diode Bolometer	~250 eV	120±8 eV 4.3–8.3 mm	~220 eV 1.7±0.2 mm core: 150–300 eV 0.9–1.4 mm halo: 50–150 eV 4–4.8 mm
Time-integrated crystal spectroscopy	1–1.8 keV	~120–170 eV 4–2 mm	~250 eV 2 mm
Transmission grating spectroscopy	0.2–2.3 keV	None	244±12 eV at 0.5 mm 115±6 eV at 5–6.2 mm
Current	NA	NA	5.6±0.8 mm

to brightness temperature as in Fig. 12(a). The pinch spectra are determined from these data by summing the spectra from each pixel, over the entire image, assuming each pixel radiates as a Planckian. This gives an equivalent pinch spectra such as would be observed in the TGS instrument. Although the temperature map was only intended to be an approximate, qualitative guide, the equivalent spectra compares favorably with the TGS spectrum.

This procedure appears to underestimate the higher-energy tail perhaps because we simply assume thermal emission for each pixel. Other spectral measurements show a harder, nonthermal tail [95]. The error in these spectra is of course much larger than the direct TGS measurement (±20%) because multiple instruments are involved (XRPHC, XRD, BOLO). In addition, assumptions about the emission geometry and source characteristics of each pixel are unverifiable. Although this process is only approximate, the comparison gives confidence in the interpretation of the TGS spectra as emission summed over a pinch with a nonuniform temperature distribution, approximated as a colder halo and a hotter core, and with a high optical depth thermal radiator.

The three independent brightness and size measurements at stagnation from the axial and radial views are summarized in Table III. As noted, one possible explanation for the difference in brightness temperature (and emission region sizes) between axial and radial measurements is that the hot core or local hot spots are not observed axially because of greater optical depth. The plasma may also expand axially after stagnation and radiatively cools as it does [96].

The convergences of the cold halo or wing region from the axial XRPHC (4.3 mm FWHM, CR=4.7:1, 8.3 mm width at the base of the wings, CR=2.4:1), from the wings of the radial XRPHC (5–6 mm, CR=3.3–4:1), and from the TGS radially (5.0–6.2 mm FWHM, CR=3.2–4:1) are similar to the convergence of the current (5.6±0.8 mm FWHM, CR=3.6±0.6:1) at peak power for the 20-mm array. These observations provide additional evidence that a smaller CR of the current sheath at peak power ($<5:1$) is a reasonable result, consistent with other experimental evidence. Convergence ratios of $\geqslant 10:1$ that have been historically inferred, based on radial pinhole camera measurements of the size of the brightest hot regions at stagnation [3,5,89], appear to be overestimates of the CR of the mass and current for massive tungsten wire arrays (>2 mg/cm).

In some respects, this picture of a colder halo surrounding hot spots or a hot-core region is similar to that proposed by Apruzese *et al.* to model the x-ray emission spectra of *K*-shell radiators [95]. In that work, a halo of colder material surrounds a hotter core region, and only a small amount of mass (~5 to 15%) is at a temperature that can efficiently produce *K*-shell emission. In this work, less than 10% of the emitting area of the pinch is at the highest brightness temperature, but results in more than half the radiated power. Some aspects of the picture of Apruzese *et al.* apparently apply to high-mass tungsten thermal radiators, but in addition we find that the radius of the cold halo seems to correlate with the effective radius of the current.

Trailing mass has been suggested previously as a cause of secondary implosions [32]. Trailing mass, or mass spread out during an extended wire ablation phase, may limit the power by shunting current away from the axis [32,35,86–88], creating a broader current sheath, or by creating a broader assembly of mass and current at stagnation, reducing the rate of rise of magnetic energy density near the axis, and therefore reducing pinch heating rates and conversion of magnetic energy to radiation. Quantitative measurements of the radial profiles of trailing mass (and current) within a factor of ~2–3 would be helpful.

Models of array trajectories with trailing mass and snowplow accretion will be presented in Sec. IV. Additional data on trailing current is presented in Secs. IV and V.

H. Summary of array implosion characteristics

We observe precursor pinch, a long wire ablation period, and delayed acceleration of the wire array edge, a from 2- to

TABLE IV. Summary of observed characteristics of wire array implosions. *X*: observation confirmed. *NY*: no published observations. *ND*: no observations presented in this paper. *P*: possible observations made. More work recommended.

Observation	Magpie [25–33] (1 MA)	Angara [34–40] (3 MA)	*Z* [41–44,50,51] (20 MA)
Implosion trajectories with a delayed acceleration of the array edge	$(0.78–0.79)\tau_{stag}$	$0.8\tau_{stag}$	$(0.44–0.74)\tau_{stag}$
Precursor plasma on the axis of the array at $>0.5\tau_{stag}$	*X*	*X*	*X*
Nonuniform axial ablation of the wires	*X*	*X*	*ND*
Nonuniform jetting into the center of the array	*X*	*X*	*ND*
Precursor expansion during acceleration phase	*X*	*NY*	*X*
Rapidly moving shock into ablated prefill	*X*	*NY*	*P*
Radiated power that ramps up during the acceleration phase and interaction with ablated wire material	*X*	*NY*	*X*
Inference of trailing mass from trajectory fitting and/or from other indirect means (opaque emission front)	*X*	*NY*	*X*
Direct measurement of trailing mass	*X*	*X*	*X*
Direct measurement of trailing current	*NY*	*X*	*X*

3-mm-wide imploding shell-like object early in the implosion possibly prior to significant MRT growth, a ramp up of the power from 0.1 to 5 TW during the implosion phase, and a limited compression ratio ($<5:1$) of the current. We also see indirect and direct evidence for trailing mass and a slow falloff of the mass density profile at the outer edge of the array, rather than a sharp edge, as well as axial modulation of the late-time density at the edge of the array. The observation of a cold halo surrounding a hotter-core region at stagnation, in multiple instruments, from axial, radial, and chordal lines of sight, appears to be consistent with the wings of trailing mass earlier in the pulse and the lower convergence ratio of the current at peak power. Prior to peak x-ray power, we observe an instability with an $m=0$ sausage character growing to large amplitude in the compressed-pinch on axis. Just after peak x-ray power, at a tighter compression, the pinch also exhibits a mild $m=1$ kink instability.

These results indicate that two-dimensional (r-z) thin-shell implosion models assuming wire ablation and wire-to-wire merger into a shell on a rapid time scale compared to wire acceleration are incorrect or at least incomplete when applied to massive (>2 mg/cm), single, tungsten wire arrays. Wire merger does not occur rapidly. When the shell does begin to implode, simulations need to consider the possible 3D nature of the perturbations generated during a long wire ablation period [25,26,50,51,97–99] as initiation for further growth of instabilities and the effect of a long ablation phase on the effective width of the imploding shell, as well as the impact of trailing mass on the rate of transfer of current to the axis of the system. These results also suggest that 2D(r-z) models of nested wire array behavior [23,48] may be incomplete and that the possible impact of discrete wire behavior of both the outer and inner arrays should be evaluated [29].

We summarize these and previous observations of wire array implosion characteristics on the Magpie (1 MA), Angara-5-1 (3 MA), and *Z* accelerators (20 MA) in Table IV. Areas marked with an "*X*" show confirmation of the particular observation on that accelerator. Areas marked with a "*NY*" have not been observed at the present time. Those marked with an "*ND*" are not presented in this paper and represent observations discussed in other publications [51]. Areas marked with a "*P*" represent possible observations. In this case more work is recommended. Based on this summary, a working hypothesis is that the behavior of wire arrays at 20 MA is qualitatively similar to those at 1–3 MA, in all aspects. The observations in common suggest that the missing observations could be confirmed with appropriate experiments. The observations in Table IV also apply to the outer array of nested array configurations. Investigations of the interaction of outer and inner arrays and the ablation rate and implosion dynamics of the inner array are in progress, guided by our new understanding of single-array dynamics. Refer to Secs. III and IV for modeling of the data with 2D-MHD simulations and the Lebedev rocket ablation model [32].

III. PHASE II–III TRANSITION: 2D-MHD MODELING OF WIRE-ARRAY ABLATION

In Secs. II D and II E (Table II), emission and electrical diagnostics determined the initial time of wire-array acceleration. In this section, comparisons of the acceleration times are made with the Alegra-3D-MHD code [80] shown in Fig. 14(a) and the Gorgon-3D-MHD code [81,85] shown in Figs. 14(b) and 14(c) to validate predicted wire ablation rates. Both simulations were run in 2D(x,y) coordinates. These simulations show the sensitivity of the predicted core burn-

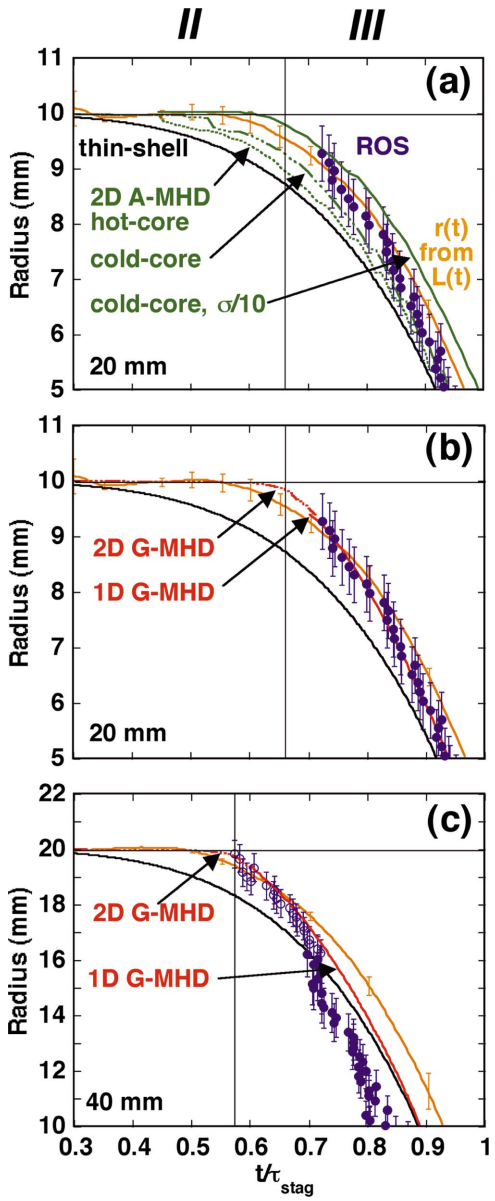

FIG. 14. (Color) Wire array trajectory measurements compared with 2D-MHD models of wire array ablation for (a) Alegra simulations (hot core, cold core, and cold core plus $\sigma/10$ models) and 20-mm array data from Fig. 6(a), (b) Gorgon simulations and 20-mm array data from Fig. 6(a), and (c) Gorgon simulations and 40-mm array data from Fig. 7(a).

through and the starting time of acceleration to the initial core and corona conditions assumed and to the equation-of-state (EOS) and conductivity models.

The Alegra-MHD code is a three-dimensional, arbitrary Lagrangian-Eulerian, finite-element code developed at Sandia for radiation-MHD modeling. The r-θ simulations are Eulerian and conducted on a 2D(x,y), Cartesian grid with $\sim$1.0 μm resolution near the wire. A single wire from the array is modeled in a periodic wedge. The relevant physics included is one-temperature resistive MHD, with thermal conduction and single group radiation diffusion. The EOS model is Kerley-Sesame and the conductivity model is Lee-More-Desjarlais (LMD) [100]. The wire-core–corona density, temperature, and velocity profiles are initialized via mapping of the variables from 1D (radial) cold-start wire initiation simulations [29,80]. The 1D cold-start simulations are conducted on a highly resolved ($\sim$0.02 μm cell size), radial, Eulerian grid. A single wire is driven by the 50-ns-long current prepulse during phase I. It is heated, melted, and eventually vaporized by the prepulse current, forming a core-corona plasma structure. After the formation of the core-corona structure, the 1D simulation is stopped and the relevant variables mapped to the 2D(x,y) geometry used for the r-θ simulations.

These "cold-start" initiation simulations give a hot, preexpanded core with a temperature of 1.2 eV for the 20-mm array. When these simulations are used to initialize, in turn, a highly resolved ($\sim$1 μm cell size near the wire) 2D simulation of the array implosion, the wire cores rapidly overheat and explode, and the trajectory of the peak density is only slightly delayed from that of a thin shell, accelerating at $\sim 0.44\tau_{\text{stag}}$ [shown in Fig. 14(a) as the "hot-core" model, dashed green line]. We use peak density since this is close to the position of peak radiation emission. This trajectory would be difficult to distinguish from a thin-shell experimentally and is more than 10–15 ns earlier than the optical streak or effective current position begins to move from the initial array position.

Similar "cold-start" calculations were performed for the 40-mm array with the earliest implosion $[\tau_a = (0.44\text{–}0.47)\tau_{\text{stag}}]$. The predicted acceleration time was $0.36\tau_{\text{stag}}$, earlier than experiment. Predicted acceleration times for the 12-mm array with the latest implosion $[\tau_a = (0.68\text{–}0.74)\tau_{\text{stag}}]$ were $0.45\tau_{\text{stag}}$, a larger discrepancy. We can readily conclude that "cold-start" simulations have a much higher wire ablation rate than we observe experimentally, for all the arrays. There appears to be a progressively larger deviation between the experimental results for acceleration time and the cold-start prediction for the heavier arrays with larger diameter wires. Deviation for the 40-mm array (7.7 μm wires) was 28%, for the 20-mm array (11.5 μm wires) 30%, and for the 12-mm array (23.4 μm wires) 64%.

Single-wire experiments performed at dI/dt's relevant to the current prepulse show termination of resistive heating after 29 ns when only 13%–21% of the vaporization energy is delivered (for 11.5-μm-diam W wires used for the 20-mm array), estimated to bring the material to the 0.32 eV melt temperature, assuming the energy was deposited uniformly in the wires [69]. For the case of the 7.5-μm wire used for the 40-mm array, the single-wire experiments [69] show a 23-ns-long resistive phase depositing 21%–28% of the energy required to vaporize the wire. At this point, the cores are a resistive, inhomogeneous solid-liquid-vapor mixture [67,101].

Discrepancies between single-wire experiments and cold-start simulations could be caused by uncertainties in the treatment of wire resistivity and EOS for possible 3D conditions with mixed phases and boiling [67,101]. This wire is at or near solid density and the melt transition and is perhaps not correctly treated as completely melted tungsten metal. Mixed-phase material may have both higher resistivity and

higher specific heat capacity than uniformly melted tungsten [102–104]. Both of these changes would reduce the ablation rate of the wire in the simulations compared to the experiment.

To estimate the effect of a colder, more resistive core or slower heating because of coronal contaminant plasma shielding [37,105,106], other Alegra simulations reduced the cold-start core temperature by a factor of 10, to 0.125 eV, without preexpansion. The trajectory of the peak density from this simulation ["cold-core" model, Fig. 14(a), solid green line] is delayed by about 8 ns from the "hot-core" case, accelerating at $0.53\tau_{\mathrm{stag}}$. This is about as early as the effective current position starts to move, but not as late as the optical streaks.

It may be that higher core resistivity is required to further delay the ablation and beginning of the implosion for the 20-mm Alegra simulations. A simulation with an initial temperature of 0.125 eV and with a factor of 10 reduction in wire conductivity σ is also shown in Fig. 14(a). These simulations show a further reduction of core heating and a further delay in array acceleration until about $0.60\tau_{\mathrm{stag}}$.

Three-dimensional, axially nonuniform ablation with a high frequency [25,26,32,36] might also lower the average ablation rate by more than a factor of ~ 2 from that obtained in 2D [80], further delaying the start of the trajectory from that of this 2D simulation, possibly in improved agreement with the start of the optical streak. Alegra simulations may also be overestimating the wire core ablation rate, even in 2D, because of assumptions used in initializing the core-corona structure or because of limitations in the treatment of heat flow to the core. Discrepancies between the wire ablation simulations and experiment might also be caused by desorption and ionization of surface and bulk contaminants from the wire [37,105,106].

The Gorgon-MHD simulation is initialized assuming that the core has already expanded to form a cold, nonionized resistive vapor and uses a perfect-gas-based EOS. Radiation is treated by a probability of escape model. Simulations of single wires were run in $2D(x,y)$ to resolve initial core expansion and ablation rates. These simulations were subsequently used to initialize 1D radial simulations of a single wire. These simulations show decreased core heating and a delayed core ablation, about the extent of the reduced conductivity case in Alegra-MHD. The low ionization state of the core in this model reduces resistivity compared to the standard LMD case.

An initial core temperature of 0.125 eV was chosen to give a best fit of the implosion of the peak density to the implosion start time from the optical streak for the 20-mm experiment [Fig. 14(b), red lines]. With this value the code also reproduces the start of the implosion for the 40-mm experiment [G-MHD, red lines, Fig. 14(c)], as well as data from aluminum Magpie arrays [32,81]. Subsequently, these same simulations predicted a $0.74\tau_{\mathrm{stag}}$ acceleration time for the 12-mm *Z* arrays, prior to the experiment, in quite reasonable agreement with the data.

As surprising as this is (e.g., one adjustable parameter, the core temperature, to fit both aluminum and tungsten trajectory results at about the same current per wire, but across a factor of 20–300 in mass, 2.5 in pulse length, and up to a factor of 6 in wire size), this may indicate that for a resistive enough core, the 2D G-MHD simulations capture enough of the physics to be relevant and that the trajectories may not sensitively depend on the precise details of the models. Also, the model may not necessarily capture the particular reasons that the core-corona structure or material conditions so drastically reduce core ablation rates in experiments. In this 2D-MHD model, when the core is highly resistive, the trajectories are insensitive to the initial core temperature and only vary by at most 5 ns.

In the Alegra-MHD treatment, a slower core heating was created by a reduction in material conductivity by a factor of 10. Both a change in specific heat and resistivity could be consistent with the change in material properties resulting from the mixed-phase nature of the wire produced by the current prepulse initiation [67,101]. Recent work on the simulation of flyer plates [102,103] required quantum molecular dynamic corrections [104] to the LMD model to properly treat the solid-liquid phase transition.

The significance of these simulations is that the core must be highly resistive and/or heat inefficiently to permit as long a life as we infer from the trajectory measurements. It appears that wire resistivity and/or EOS models need to be improved to match the initial state of the wires produced during the initiation phase (I). These states may drastically reduce wire-heating rates and dominate the further evolution of the wire-array behavior. More work on core and corona conditions during wire initiation is indicated in order to arrive at these resistive conditions from a cold start. Beyond this conclusion, the trajectory data are not sufficient to constrain further either the choice of the various properties used in the simulations (EOS or resistivities) or the actual configurations of the wire core and corona (temperatures, densities, diameters, or constituents). Both the wire properties and core-corona configuration appear to impact the ablation rate.

Additional experimental data, such as x-ray backlighting [50,51], are required to validate the models by comparing measured core sizes. In addition, pulsed gas desorption measurements are recommended to establish contaminant inventories to evaluate their possible importance. Since the trajectory data exhibit 3D effects (different diagnostic techniques have different starting times, different velocities, and produce trajectories which cross over each other), 2D models may ultimately be inadequate to model ablation rates.

IV. PHASES II AND III. MODELING OF ABLATION, IMPLOSION, AND ACCRETION OF INJECTED MASS

We compare the trajectory implied by the emission front, or the current sheath, and the power increase during implosion with the phenomenological rocket ablation and snowplow accretion model due to Lebedev *et al.* [32]. We also compare the pinch power increase during the implosion phase (data discussed in Sec. II D) with a 1D MHD simulation. The MHD models suggest that current convection is an important factor in Ohmic heating of the material inside the array. The 1D-MHD simulation is unable to generate powers much above 1 TW, however, while the measured powers are

1–5 TW prior to stagnation. These simulations and models show that inelastic snowplow accretion of the preinjected mass potentially contributes significantly to the power increase during the implosion run-in. A phenomenological energy balance model is presented to explain the expansion of the precursor radius as related to increasing absorption of energy as the power increases during implosion [32].

A. Rocket ablation model

Lacking a predictive method for calculating wire ablation rates in 3D we turn toward phenomenological modeling. Ablation rates have been estimated by two other techniques. The Lebedev rocket model (RM) [32] assumes that the ablation rate per unit length of the wires is given by the following expression:

$$\frac{dm_{\text{ablate}}}{dt} = -\frac{\mu_0 I_\ell^2}{4\pi R V_a}, \tag{3}$$

where μ_0 is the permeability of free space, I_ℓ the array current, R the array radius, and V_a a constant precursor injection velocity. This model is an expression of momentum balance, assuming that the $\mathbf{J}\times\mathbf{B}$ force is transmitted entirely to the corona, which is continuously ablated from the wire cores, and that the cores are stationary. The ablation velocity is assumed to remain constant. This expression does not explicitly have a dependence of the ablation rate on wire number. Wire number variation may cause a change in V_a in this model [81,91].

A similar scaling for the ablation rate was found from a numerical fit to 2D-MHD simulations of Sasorov, assuming the tungsten plasma generation rate can be modeled as the ablation of a uniform tungsten shell or liner [35]:

$$\frac{dm_{\text{ablate}}}{dt}\ [\mu\text{g cm}^{-1}\ \text{ns}^{-1}] = 0.4\pi\frac{I^{1.8}\ [\text{MA}]}{R^{0.8}\ [\text{cm}]}. \tag{4}$$

We note that Eqs. (3) and (4) scale similarly with current and array radius. The two formulas give equal ablation rates assuming

$$V_a\ [\text{cm}/\mu\text{s}] = 12.6\left(\frac{I\ [\text{MA}]}{R\ [\text{mm}]}\right)^{0.2} \tag{5}$$

in Eq. (3). This gives a range of ablation velocities of 7–15 cm/μs for $R\sim$4–10 mm and $I\sim$1–20 MA. This range shows that V_a may be a weak function of wire array conditions [81]. Given this formula, ablation velocities would be 8.3 cm/μs for Magpie (1 MA, R=8 mm), 12.3 cm/μs for the 40-mm Z array, 14.2 cm/μs for the 20-mm Z array, and 15.4 cm/μs for the 12-mm Z array. This is also similar to the weak dependence of ablation velocity derived in a recent study of the relevance of Eq. (3) to wire-array ablation rates from 2D-MHD simulations [81]. Both 2D simulations ablate all the wire-array mass. The velocity of the precursor flow measured by end-on laser probing on Magpie was 15 cm/μs [32], nearly a factor of 2 higher than the velocity from Eq. (5). Nonuniform ablation may be equivalent to a higher effective ablation velocity (a lower average ablation rate), in this model.

B. Rocket model fitting of emission and current trajectory data

In the rocket ablation model, the ablation velocity was a constant parameter chosen to relate the ablation rate to the force on the array. A choice of V_a also sets the mass profile inside the array. The density profile is given by the expression [32,91].

$$\rho(r,t) = \frac{\mu_0}{8\pi^2 V_a^2 R r}\left[I_\ell\left(t - \frac{R-r}{V_a}\right)\right]^2. \tag{6}$$

This expression uses an ablation rate calculated at a retarded time given by $t-(R-r)/V_a$. Here, the density profile is allowed to move as the array continues imploding. The rocket model allows one to assume that some of the initial array mass trails behind the implosion front and so can approximate 3D effects on the array dynamics [32]. This expression neglects possible acceleration of the prefill internal to the wire array via current convection with the ablated plasma. The trajectory is found by integrating the snowplow equations of motion [19,32], transformed to the moving frame of the snowplow. A portion of the mass is ablated, at a rate given by Eq. (3), with a prefill profile given by Eq. (6).

This is obviously a highly simplified model of the actual experimental conditions. The wire array implosion is more complex than a simple 1D ablation front and 1D implosion trajectory model can capture. The implosion trajectory data described in Sec. II showed a variety of implosion trajectories with different techniques. We found that the trajectories from visible emission, x-ray emission, and current had somewhat different initial acceleration times and very different velocities of approach, arrival times on the axis, and convergences. The evidence for a trailing mass profile from the XRPHC and shadowgraphy at the outer edge of the array requires a 3D explanation. Trailing mass and current data from lower current arrays also implied different implosion velocities along the length of the array, initiated by nonuniform axial ablation. Nonuniform axial ablation along the length of the wire array corresponds to a variation of ablation velocity along the length of the wire, in the rocket model. The actual array might be thought of as having a distribution of plasma ablation and injection velocities and a distribution of implosion velocities along the length of the array.

The rocket model, as used in this paper, is a three-parameter fit. We vary the time of acceleration, the ablation velocity V_a, and the fraction of mass left behind at the array edge or trailing behind the implosion front. This is a nonunique set of parameters that can vary over some range. We evaluated the goodness of fit for these three parameters by comparing to three independent measurements from the 20-mm array data described in Sec. II.

The model parameters are chosen to match the trajectory as follows. We match the starting time of the acceleration to the radial optical streak (e.g., $\sim 0.60\tau_{\text{stag}}$). We match the ending radius and time of the acceleration to the peak of the axial XRPHC, when the shell merges with precursor ($\sim$1.5 mm at $0.96\tau_{\text{stag}}$). We chose ablation velocities such that the distribution of density [Eq. (6)] and the implosion trajectory produce an increase of the power during implosion

to match (if possible) the measured power. The calculated power is assumed to be entirely from an inelastic snowplow accretion of the injected mass [32]. This last requirement greatly narrows the range of ablation velocities required to match the data (see Sec. IV D).

The rocket model is used to obtain estimates for the mass that corresponds to the various trajectory measurements (the involved mass). By implication, this also gives us the mass that trails behind or is outside the front corresponding to those measurements. We do not know from this model how far outside the trajectory fit the mass could be. The model assumes an infinitesimally thin current sheath, while the real object has a finite sheath width. Simulations of an MRT unstable 2D shell [22,23] with an RDP do show a slightly smaller inductance (larger radius) than that associated with a 1D thin-shell model. This 2D trajectory lags minimally behind a thin shell during the implosion, until MRT broadens the distribution very near the axis [22,23]. These effects are not sufficiently large to allow a 2D shell model to agree with the *Z* trajectory data, which show significant differences from 1D or 2D behavior, well away from the axis.

Figure 15(a) compares a rocket model trajectory with the trajectory data from the emission diagnostics. Ablation velocities of 14 ± 3 cm/μs, ablation times of $\sim 0.6\tau_{\mathrm{stag}}$, and a final radius and time of 1.5 mm at $0.96\tau_{\mathrm{stag}}$ allowed reasonable agreement of the rocket model with the emission trajectory data. The chosen trajectory fits the outside edge of the array early and the peak of the XRPHC later, as shown in Fig. 15(a) (R_{piston}, purple line). Ablation velocities in this range also allowed agreement of inelastic snowplow power with the measured power increase during the implosion, over a 20-ns period just prior to stagnation [see Sec. IV D, purple lines in Fig. 17(a)].

These ablation times and velocities imply a range of $47\%\pm8\%$ of the initial array mass could be ablated and injected as a precursor for the 20-mm array. In order to have a trajectory accelerating as fast as the peak of the XRPHC, assumed to be driven to the axis by all the measured load current, only about $24\%\pm5\%$ of the initial mass could be accelerated as a moving piston into the ablated prefill. A higher mass would have resulted in a slower implosion, not matching the emission data and not arriving on axis near the foot of the power pulse. The accretion of mass ahead of this piston produces radiation [e.g., the shell-like feature in Figs. 8(a) and 8(b)]. This trajectory corresponds to the trailing of $29\%\pm4\%$ of the absolute array mass (1.7 ± 0.2 mg/cm).

Since 47% of the array mass is ablated and injected as a precursor, only 53% is left at the edge at the start of acceleration. The piston mass (24% of the total array mass) corresponds to 45% (=24%/53%) of the mass left at the array edge at the end of the ablation phase. The trailing mass (29% of the total array mass) corresponds to 55% (=29%/53%) of the mass at the edge of the array at the end of the ablation period, which appears to arrive on axis only after the arrival of the bright XRPHC front. According to this model, when this bright front arrives on axis it has assembled 4.2 mg. The trailing current appears to be accelerating the remaining 1.7 mg into the mass already assembled on the axis.

These results may give reasonable estimates of the ablated mass prior to the start of acceleration (about 50% of the total). This particular fit provides an upper bound on the piston mass and a lower bound on the trailing mass because it assumes that all the current is driving the acceleration of the emission front. Measurements of the load inductance indicated that the effective radius of the current lags well behind this brightest emission front. This rapidly moving and brightest emission front does not in fact carry the entire load current down to the axis, as shown in the circuit modeling of electrical data presented in Sec. IV C. This is another indication of axial inhomogeneity of the implosion. The difference between the radius of the brightest emission and the effective radius of the inductance is the best evidence for trailing mass and current.

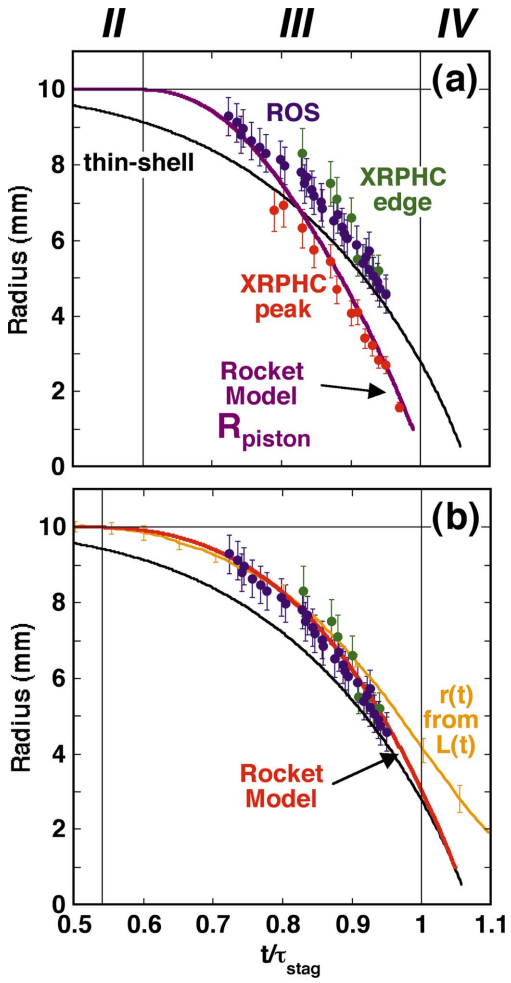

FIG. 15. (Color) (a) Comparison of wire array emission trajectory measurements corresponding to the brightest implosion front [peak of the radial profile from the axial x-ray pinhole camera (XRPHC peak) from the 20-mm array data from Fig. 6(a)] with a Lebedev rocket model fit. This trajectory involves ~60%–80% of the initial array mass. (b) Comparison of wire array inductance trajectory measurements corresponding to the array edge [inductance, radial optical streak (ROS) and XRPHC edge from 20-mm data from Fig. 6(a)] with a rocket model fit. This trajectory involves 90%–100% of the initial array mass.

We also fit a rocket model trajectory as closely as possible to the trajectory of the inductance or current as shown in Fig. 15(b) (red line). We match the starting time of the accelera-

tion to the effective current trajectory ($\sim 0.54\tau_{stag}$). We match the ending radius and time of the acceleration to the radius corresponding to the load inductance at peak power (2.8 ± 0.4 mm at $1.05\tau_{stag}$). Ablation velocities of 10–14 cm/μs, wire array ablation periods of $0.54\tau_{stag}$, and an initially ablated mass of $40\% \pm 6\%$ match, within experimental error, the trajectory of the current [down to $r(t) \sim R/2$] and radiation emission data from the array edge (ROS, XRPHC). These fits leave trailing mass of 0%–7% and therefore encompass most of the array mass. These estimates are again upper bounds on the mass of the piston and lower bounds on the trailing mass, because not all the current is located at the radius of the effective inductance. The last 30% of the mass of the array appears to come in between the foot of the power pulse and peak power, and may determine the effective inductance of the mass at stagnation.

The trajectory of the current still lags behind the model trajectory for $r(t) < 0.5R$, even including all the mass [Fig. 15(b)]. This possibly indicates trailing mass, a thicker current sheath, or some mass that leaves the edge of the array after $0.54\tau_{stag}$. The discrepancy could also be explained by a systematic error in the inductance unfolds because of current loss in the AK gap or convolute later in the pulse, after $t > 0.93\tau_{stag}$. This is difficult to rule out. The rocket model fits and current trajectory data together imply that no more than of order 10% of the mass can be outside a diameter of about 6 mm at peak power.

Similar fits to the emission and inductance data were made for the 40-mm array (not shown). For the trajectory of the emission diagnostics [Fig. 7(a)], fitting $V_a = 27 \pm 3$ cm/μs suggests $41\% \pm 5\%$ is ablated and injected, $32\% \pm 5\%$ is accelerated as a piston, and $28\% \pm 3\%$ is trailing. The trailing mass (28% of the total array mass) corresponds to about 47% (=28%/59%) of the mass at the edge of the array at the end of the ablation phase. Although the fraction of mass that trails appears to be about the same as for the 20-mm array, the absolute trailing mass is 0.6 mg/cm, which corresponds to only $36\% \pm 6\%$ of the absolute trailing mass per unit length compared to the 20-mm array. The inductance trajectories, even including all the mass, lag somewhat farther behind the trajectory of the current than was the case for the 20-mm array. This discrepancy is consistent with a larger systematic error in the inductance unfolds for the 40-mm array, compared to the 20-mm array.

To match Magpie emission trajectories with the moving prefill model [91], 40% of the initial array mass is injected, 20% is in the piston, and 40% trails. The trailing mass (40% of the initial array mass) corresponds to 66% of the mass at the array edge (=40%/60%) at the end of the wire ablation period trails behind the main implosion front, based on emission data. The longer ablation period of Magpie arrays compared to *Z* arrays ($\sim 0.8\tau_{stag}$ vs $\sim 0.55\tau_{stag}$) correlates with a larger fraction of trailing mass (40% vs 30%), but within the error of the fitting technique, these are about the same.

Table V summarizes the rocket model fits for arrays on *Z* and Magpie. Based on the average of these fits to three different arrays on two accelerators, about 40%–60% of the initial array mass is ablated in phase (II), a piston mass of 20%–30% of the initial mass accelerates into this ablated prefill during phase (III), and 30%–40% of the initial mass trails behind the brightest implosion front. This trailing mass corresponds to 45%–66% of the mass left at the edge of the array at the end of the ablation phase. The rocket model fit to the peak of the axial XRPHC data indicates that about 30% of the array mass trails behind this front, at the foot of the power pulse, for both the 20-mm and 40-mm arrays. The rocket model fit to the ROS, current, and XRPHC array edge data shows, down to $r(t) \sim 0.5R$–$0.25R$, the location inside of which up to 90%–100% of the mass resides [Fig. 15(b)]. The inductance trajectories on *Z* appear to contain almost all the initial wire array mass, within about 10% at peak x-ray power.

TABLE V. Rocket ablation model fits to wire array trajectory data.

			Fractions of total mass (%)		
Array (mm)	t_a/τ_{stag}	V_a (cm/μs)	Ablated	Piston	Trailing
40	0.54–0.57	27 ± 3	41 ± 5	$<32 \pm 5$	$>27 \pm 5$
20	0.60	14 ± 3	47 ± 8	$<24 \pm 5$	$>29 \pm 4$
Magpie[a]	0.80	15	40	20	40

[a]Courtesy of S. V. Lebedev.

The differences between the rocket model fits to the emission and current data illustrate the limitations in trying to piece together 1D models and various chordally integrated 2D measurements or global inductance unfolds to understand a fundamentally 3D object. The rocket model provides an interpretation of the trajectory data as a distributed implosion, with precursor, main, and trailing implosions. Based on these fits, we conclude that the emission front observed on the ROS shows when the initial implosion onto the precursor prefill begins. As observed in experiments on Magpie, this likely occurs at only some axial locations as the cores are nonuniformly ablated. The axial XRPHC shows a very rapidly moving and hotter emission front, accelerating away from the fronts implied by the ROS and current data. This surface may be the snowplow shock, propagating into the ablation prefill [32], or evidence of the implosion beginning or proceeding more rapidly at some axial locations than others.

Assuming that the current is constant on the time scale of the plasma motion, we can estimate the plasma clearing or compression time τ_C between radii R_i and R_f by [89]

$$\tau_C = \sqrt{\frac{\pi}{2}} \mathrm{erf}\left\{ \sqrt{\ln \frac{R_i}{R_f}} \right\} \tau_A, \tag{7}$$

where τ_A is the Alfvén transit time for the initial radius R_i:

$$\tau_A\,[\mathrm{ns}] = \frac{R_i}{V_A} = \frac{316 R_i\,[\mathrm{cm}] \sqrt{m_0\,[\mathrm{mg/cm}]}}{I\,[\mathrm{MA}]} = \frac{R_i^2\,[\mathrm{cm}^2] \sqrt{A n_i\,[\mathrm{atoms/cm}^3]}}{4.38e7 I\,[\mathrm{MA}]}. \tag{8}$$

In Eq. (8), V_A is the Alfvén velocity, m_0 is the plasma mass per unit length, n_i is the ion density, A is the atomic mass

number, and I is the current at that radius. Given ratios of $R_i/R_f \sim 1.3$–6 relevant to experiments, $\tau_C \sim (0.7$–$1.2)\tau_A$.

The shadowgraphy data of Fig. 7(b) (40-mm array) showed mass trailing for 20 ns in the outer 5 mm near the array edge, prior to clearing. Substituting $R_i = 2.0$ cm, $R_f = 1.5$ cm, $A = 184$, $I \sim 15$ MA, and $n_i \sim 10^{16}$–10^{17} cm^{-3} in Eqs. (7) and (8), we find $\tau_C = 0.69\tau_A = 6$–18 ns. Ion densities of $>10^{17}$ cm^{-3} (or $n_e > 10^{18}$ cm^{-3} for $\bar{Z} \sim 10$ or $m_0 > 0.5$ mg/cm, about 24% of the initial array mass) can therefore effectively impede the rate of current transfer toward the axis for >20 ns near the edge of the array, at $R_i = 2.0$ cm here. This is about the same as the 27% ± 5% trailing mass at the foot of the power pulse estimated from rocket model trajectory fitting, summarized in Table V.

This trailing mass at the edge of the array, once compressed, may produce the wings on the density profile at stagnation observed with the radial XRPHC. Recall in Fig. 11(a) (20-mm array) that a compression time scale of 9 ns was observed to bring the mass located about 3 mm from the axis in the wings of the profile, to within a 0.5 mm radius. Substituting $R_i = 0.3$ cm, $R_f = 0.05$ cm, and $I \sim 15$ MA at $n_i = 10^{19}$–2×10^{19} cm^{-3} ($m_0 \sim 0.9$–1.8 mg/cm or about 15%–30% of the initial array mass distributed in the wings) in Eqs. (7) and (8), we find $\tau_C = 1.18\tau_A = 7$–10 ns. This estimate is about the same as the 29% ± 4% trailing mass at the foot of the power pulse estimated from rocket model trajectory fitting, summarized in Table V. Ion densities of $>10^{19}$ cm^{-3} in the wings of the mass density profile at stagnation can effectively impede current transfer to the axis or hold up current at a larger radius on a >5 ns time scale.

This time scale is relevant to pinch thermalization rates because it is of order or greater than the typical pinch power rise times of 3–6 ns. Trailing ion densities as low as 10^{18} cm^{-3} near the edge of the array increase to 9×10^{18}–1.6×10^{19} cm$^{-3} \sim (R_i/R_f)^2$ once compressed near the axis with a convergence ratio of 3–4. We showed that densities in this range are clearly able to influence the rate of transport of current to the pinch and therefore the final pinch compression and thermalization rates. Rapid transfer of current to the axis and rapid compression of the pinch requires lower ion densities and a larger magnetic field (higher Alfvén velocity). A larger magnetic field requires a smaller effective radius of the current, which implies we should strive to limit mass profiles with trailing wings and trailing current.

The fraction of trailing mass may depend on the scale length and amplitude of the nonuniform ablation, on the length of the ablation period, or on the time scale for acceleration [81]. Direct measurements of the quantity and spatial distribution of trailing mass will determine how the nonuniform ablation and trailing mass actually limits the compression of the mass and the convergence of the current. X-ray radiography with bent-crystal imaging is one possible method [50,51].

C. Equivalent circuit modeling of electrical data

A trajectory model including the rocket model and the thin-shell model as limits was coupled to an equivalent circuit model for the Z accelerator [41]. This allowed us to generate predicted machine electrical data (voltages and currents) with various assumptions for the trajectory of the current. The equivalent circuit is shown in Appendix A [Fig. 24(b)] [54]. Within the confines of this model, no choice of ablation velocity, starting and ending radii, and time for acceleration can simultaneously fit the total current, load current, convolute voltage, either emission or current trajectory, and power increase during the implosion. Again, this is a fundamental problem of using 1D models to interpret 2D diagnostic views of a 3D object.

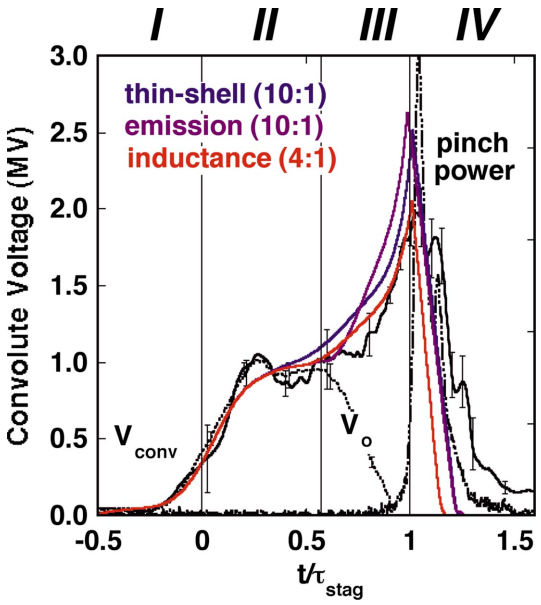

FIG. 16. (Color) Comparison of measured convolute voltages for the 20-mm array [from Fig. 5(b), shot 818] with models of convolute voltages for three cases: thin shell at a convergence of 10:1 (blue line), emission at a convergence ratio of 10:1 (purple line), and trajectory of inductance at a convergence of 4:1 (red line). The load impedance is consistent with a smaller convergence of the current.

The convolute data from Fig. 5 are compared with the predicted voltages in Fig. 16. The measured peak convolute voltage of the 20-mm array was 2.0 ± 0.1 MV. A thin-shell trajectory model (blue line) assumes that the mass and current converge simultaneously to a 10:1 convergence ratio. This model ramps up faster than the data to a peak of 2.6 MV. A trajectory matching the emission data [purple line from Fig. 15(a)], starting at $t/\tau_{\text{stag}} = 0.60$ and rapidly converging to a 10:1 ratio at the moment the peak of the XRPHC shell strikes the precursor, ramps up very quickly to a peak of 2.7 MV (purple line, Fig. 16). Clearly all of the current does not follow a trajectory with this high an L_a and dL_a/dt. A trajectory matching that of the load inductance unfold [red line, Figs. 6(a) and 15(b)] converging to a 4:1 ratio matches the peak voltage of 2 MV (red line, Fig. 16).

We note that the voltage from the inductance model does not entirely agree with the measured convolute voltage throughout the pulse. These circuit models incorporate a voltage and current-dependent impedance model [54] to approximate the current loss in the post-hole convolute. The impedance $Z_{\text{conv}}(t) = V_{\text{conv}}(t)/\sqrt{I_a^2(t) - I_l^2(t)}$ where I_a is the up-

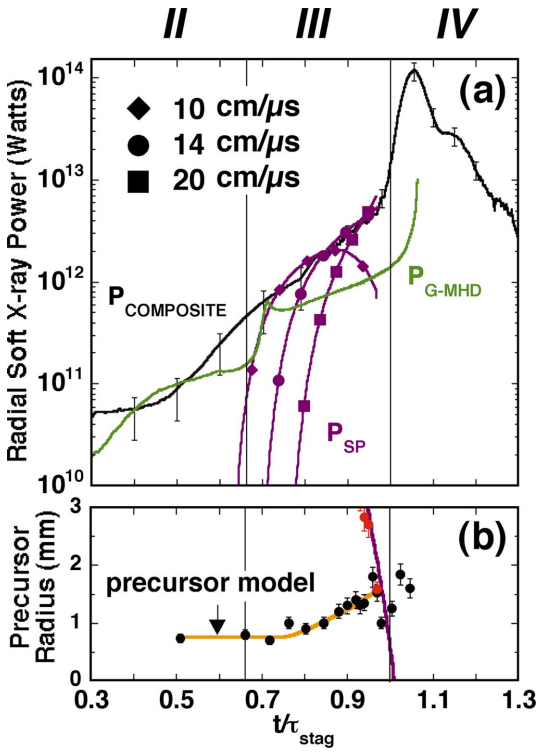

FIG. 17. (Color) (a) Comparison of a composite pinch power history during the implosion phase [$P_{\text{composite}}$, black line, from Fig. 6(b)] with a 1D-resistive MHD model ($P_{\text{G-MHD}}$, green line), and a snowplow accretion model [P_{SP}, purple lines, from trajectory of Fig. 15(a)]. Triangles correspond to an ablation velocity of 10 cm/μs, circles to 14 cm/μs, and squares to 20 cm/μs. (b) Comparison of the measured increase in precursor diameter [black circles, from Fig. 6(c)] with a simple precursor energetics model (orange line). The peak of the radial profile of the axial x-ray pinhole camera radial profile peak is shown in red circles, rocket model trajectory shown with a purple line.

stream or accelerator current and I_l is the downstream or load current, and $I_{\text{loss}}=I_a-I_l$. $Z_{\text{conv}}(t)$ was held fixed at 0.2 Ω to match the convolute current loss at peak current. The data, however, imply that a time-dependent flow impedance is required to model the convolute loss throughout the entire pulse [102,103]. As discussed in Sec. III G, sources of current loss in parallel with the *z* pinch at the convolute and in the AK gap at the base of the pinch need to be modeled properly in order to arrive at the correct effective convergence ratio of the current. AK gap loss at the base of the pinch was also neglected. In addition to a time-dependent convolute impedance, improved modeling of the electrical data may require a model of the current loss at the base of the pinch.

D. Pinch power increase during the implosion run-in

Several different models for the power increase during implosion are shown in Fig. 17. The composite pinch power curve, discussed in Sec. II F, is plotted in Fig. 17(a) (black line). This curve is obtained by joining the silicon diode data (early) with the XRD/bolometer data (later) at $t=0.85\tau_{\text{stag}}$. We consider two main sources of energy for radiation during the implosion run-in phase (III): inelastic collisions and Ohmic heating. The models indicate that both together could account for the power radiated during the implosion phase. Inelastic collisions dominate Ohmic heating for these models.

The MHD models for wire ablation, described in Sec. III, show a magnetic Reynolds number $R_m \sim 1$ near the wires and large $R_m > 10$ in the bulk of the precursor plasma inside the array. Small R_m near the wires limits current convection inside the array. Large R_m in the bulk plasma implies that whatever field does convect inside the array with the precursor would be frozen in. The 2D-MHD models show convection of up to 30%–40% of the total current inside the array diameter with the precursor. In these simulations, the ablated plasma continues to heat and accelerate inside the array, because of the entrained current. The acceleration of the precursor plasma results in a much smaller velocity difference between the velocity of the piston and the ablated plasma (V_p-V_a), which greatly reduces the inelastic snowplow power.

Resistive heating of the wire coronal material and the mass inside the array therefore produces 95% of the radiated power in the Gorgon-MHD model [$P_{\text{G-MHD}}$, green line, Fig. 17(a)], in reasonable agreement with the data at $<0.7\tau_{\text{stag}}$. Ohmic heating of the corona or precursor plasma may be responsible for the $\sim$0.5 TW radiation of the array during phase (II), prior to array motion. Ohmic heating produces a maximum of $\sim$0.5 to 1 TW of radiated power from the array between $0.7\tau_{\text{stag}}$ and $1.0\tau_{\text{stag}}$, during phase (III), with this model.

The 0.5–1 TW of Ohmic deposition is only about 20% of the total power radiated during the pinch run-in. The bulk of the power may result from inelastic collisions of the moving piston with the injected precursor mass. The snowplow accretion model [19,32] [P_{SP}, purple lines, Fig. 17(a)] assumes that the power is generated from inelastic collisions between the imploding piston (velocity V_p) and precursor with mass density profile $\rho(r,t)$ (transformed to the moving frame of the precursor):

$$P_{\text{SP}}(t)=\frac{1}{2}\frac{dm}{dt}\left(\frac{dr}{dt}-V_a\right)^2 \propto \frac{1}{2}\rho(r,t)(V_p-V_a)^3, \qquad (9)$$

where power is generated if $dr/dt > V_a$ and the mass density profile $\rho(r,t)$ is generated via the constant ablation velocity V_a [Eq. (6)].

Three different snowplow cases are compared with the measured power in Fig. 17(a). The purple lines correspond to the rocket model fit to the emission trajectory data shown in Fig. 15(a) and discussed in Sec. IV B. The three curves correspond to different ablation velocities. Ablation velocities of 14 ± 3 cm/μs produce a reasonable match to the measured power with the inelastic collision model over the 20-ns period leading up to the stagnation time.

The rocket model has been modified from the previous treatment [32] to allow the ablated prefill mass to redistribute at a constant initial velocity, while the array implodes [91]. In the previous treatment, the prefill profile was fixed at the

initial time of array motion [the retarded time in Eq. (6) was given by $t_a-(R-r)/V_a$, with t_a being the time acceleration starts [32]]. Allowing motion provides an increasing density ramp toward the axis [91]. Prefill motion was required for generating inelastic powers that agreed with the measured power for the 40-mm array. Ablation velocities of 27 ± 3 cm/μs produce a reasonable match of the inelastic collision model with the measured power over the 20-ns period leading up to the stagnation time, for the 40-mm-diam array.

The ramp up of the power as stagnation nears can only be reproduced, if inelastic collisions are assumed to dominate, by a density profile that peaks towards the axis and for a particular narrow range of ablation velocity. Ablation velocities of <12 cm/μs (<19 cm/μs) do not produce a ramped density profile for the 20-mm (40-mm) array, hence the fall-off in power for the 10 cm/μs velocity in Fig. 17(a). Assuming that the power results entirely from inelastic collisions, one can invert Eq. (9) using the measured power, the piston velocity from the trajectory fit in Fig. 15(a), and the ablation velocity, to determine the density profile encountered by the imploding piston, as a function of radius. This profile is self-consistent with that generated from Eq. (6), for velocities in the range of 12–17 cm/μs, and ramps up towards the axis. The requirement that the power agree with that generated from inelastic collisions provides strong constraints on the fitting parameters for the rocket ablation and snowplow models. The peaking of the density towards the axis may contribute to snowplow stabilization of wire array implosions [21,32,91–94]. It is interesting to note the similarity of Eq. (6) to analytic estimates by Hammer *et al.* [21] and Douglas *et al.* [94] of the mass density required to tamp the growth of MRT by the accretion of mass.

Ohmic heating power might be increased by axial nonuniformities in the plasma density or current (3D effects) or resistivities higher than Spitzer. If there is actually entrained current in the experiments, collisional effects [107] not included in MHD codes might reduce the precursor velocity near the axis, increasing the contribution of the inelastic power towards the limit of the constant-V_a snowplow model. Also, analytic work [108,109] indicates that $R_m\sim1$ near the cores, which could limit both current convection inside the array and acceleration of the injected plasma. MHD codes could therefore overestimate the current convecting inward from the region near the wires and therefore overestimate the plasma acceleration internal to the array. More work is required.

In conclusion, it is reasonable to suppose that some combination of power generated by Ohmic heating (0.5–1 TW) and inelastic collisions (up to 4–5 TW), possibly including 3D nonuniformities, can account for the 1–5 TW of power radiated during the implosion phase (III). Other heating mechanisms may exist based on 3D effects producing hot spots or other phenomenon [38,39]. The pessimistic conclusion of a previous work was that the implosion could not be represented as a snowplow implosion [39]. Although this is probably accurate in the strict 1D sense, the results presented in Secs. IV B, IV C, IV D, and IV F, following, indicate that the snowplow picture is, in fact, helpful for interpreting 2D trajectory and pinch power data. An important area for future development is to determine the current distribution inside the array, as a test of the MHD predictions.

The pinch power is the most highly integrated experimental measurement made on pinches and as such depends on many factors. The pinch power is therefore likely to be the most difficult measurement to model. The mechanisms for the pinch power ramp up during the implosion phase need to be determined and models further developed. Improved predictive models are important because we might be able to control this phase of the implosion in such a way as to produce radiation pulse shapes appropriate for ICF applications. Some progress in this direction has been reported [84].

E. Precursor expansion model

Figure 17(b) compares the precursor radius with a phenomenological model. We observe the precursor radius begins to expand ($\sim0.75\tau_{\mathrm{stag}}$) [Fig. 6(c)]. As discussed previously [32], the equilibrium precursor diameter may be a balance between the thermal pressure and the kinetic pressure of the incoming ablated mass. The kinetic pressure of the plasma flow, arriving on the surface of the precursor, is

$$P_{\mathrm{kin}}=\frac{V_a}{2\pi R_p}\frac{dm_{\mathrm{ablate}}}{dt}, \tag{10}$$

where V_a is the ablation velocity, R_p the precursor equilibrium radius, and dm_{ablate}/dt is the mass ablation rate per unit length. The thermal pressure in the precursor pinch balances this kinetic pressure:

$$P_{\mathrm{th}}=(\bar{Z}+1)n_iT. \tag{11}$$

Equation (11) can be rewritten through the total thermal energy E of the precursor:

$$E=\frac{3}{2}(\bar{Z}+1)n_i\pi R_p^2\ell T, \tag{12}$$

where ℓ is the pinch length, n_i the precursor ion density, and T the precursor temperature. Substituting Eq. (12) into Eq. (11) gives the following expression for the thermal pressure:

$$P_{\mathrm{th}}=\frac{2}{3}\frac{E}{\pi R_p^2\ell}. \tag{13}$$

Equating the kinetic pressure [Eq. (10)] and the thermal pressure [Eq. (13)] we find the following expression for the equilibrium radius of the precursor:

$$R_p=\frac{4}{3}\frac{E}{\ell V_a\dfrac{dm_{\mathrm{ablate}}}{dt}}. \tag{14}$$

Before the start of the implosion phase (III), the increase of the thermal energy of the precursor by the accumulation of mass is balanced by the increase of the kinetic pressure, and the precursor column radius is almost constant [33]. The precursor column will absorb some fraction of the snowplow radiation from the piston during the implosion phase, leading to increase of the thermal energy,

$$\frac{dE}{dt} = F(1-\alpha)P_{\mathrm{SP}}, \tag{15}$$

and to a corresponding increase of the equilibrium precursor radius:

$$\frac{dR_p}{dt} = \left(\frac{4}{3\ell V_a \dfrac{dm_{\mathrm{ablate}}}{dt}}\right)\frac{dE}{dt} = \left(\frac{4}{3\ell V_a \dfrac{dm_{\mathrm{ablate}}}{dt}}\right)F(t)(1-\alpha)P_{\mathrm{SP}}. \tag{16}$$

Here $F(t) \sim (2R_p)/(2\pi R_{\mathrm{piston}})$ is a view factor, P_{SP} is the radiation power from the imploding piston [Fig. 17(a), purple line with circles], R_{piston} is the radius of the imploding piston [Fig. 15(c), purple line], and α is the albedo of the precursor column. The albedo (=0.88) was adjusted to match the measured rate of precursor expansion. Precursor expansion was also observed at $t \geqslant 0.80\tau_{\mathrm{stag}}$ with laser diagnostics on 1-MA Magpie arrays [26,32], e.g., as acceleration begins. The precursor expansion data and this model provide additional evidence consistent with a rapidly increasing total radiated power well above 1 TW, during run-in.

F. Trajectory scaling

We noted that wire arrays on *Z* appeared to have a higher ablation rate per unit mass compared to arrays studied on lower-current accelerators. We found array implosions beginning at $0.5\tau_{\mathrm{stag}}$–$0.6\tau_{\mathrm{stag}}$ compared to arrays on Magpie and Angara-5-1 accelerators that began movement at $\sim 0.8\tau_{\mathrm{stag}}$. We also showed that heavier, smaller-diameter arrays accelerated later than the larger-diameter, lighter arrays, on *Z*. These observations can be explained by a higher ablation rate per unit mass for arrays that accelerate earlier in the current pulse. This conclusion does not depend on the model used to interpret the mass ablation rates.

Based on the rocket model, the ablation rate per unit mass is simply Eq. (3) divided by the initial array mass/length m_0:

$$f_m = \frac{\left|\dfrac{dm_{\mathrm{ablate}}}{dt}\right|}{m_0} = \frac{\mu_0 I_\ell^2}{4\pi R V_a m_0}. \tag{17}$$

This expression implicitly contains time in the load current. Load currents on Magpie can be represented by

$$I_{\ell M}(t) = I_m \sin^2\left(\frac{\pi}{2}\frac{t}{t_m}\right), \tag{18}$$

where I_m is the peak current driving the array and t_m is the time of peak current (240 ns for Magpie). The *Z* accelerator has a faster rate of rise of current (and ablation) than this function. Load currents for *Z* can be fit by [15]

$$I_{\ell Z}^2(t) = \frac{I_m^2}{2}\left(\frac{t}{t_m}\right)^2\left[3 - \left(\frac{t}{t_m}\right)^4\right], \tag{19}$$

where I_m is the peak load current and t_m is the time of peak current. *Z* current pulse shapes are well fit with $t_m = 90.4$ ns for 12-mm-, 20-mm-, and 40-mm-diam arrays, through about 100 ns.

Also, time is implicitly contained in the choice for the initial array mass m_0. These parameters m_0, I_m, and a characteristic time of the implosion, τ, are related through a dimensionless similarity variable Π [19]:

$$m_0 = \frac{\mu_0 I_m^2 \tau^2}{4\pi \Pi R^2}. \tag{20}$$

Π will vary for different current pulse shapes and array configurations. We let $\tau = \tau_{\mathrm{stag}}$.

Substituting Eq. (20) into Eq. (17), we find

$$f_m(t) = \frac{\Pi K}{\tau_{\mathrm{stag}}}\left(\frac{I_\ell(t)}{I_m}\right)^2, \tag{21}$$

where $K = R/[V_a \tau_{\mathrm{stag}}]$ is the wire array ablation similarity parameter proposed by Lebedev *et al.* [32], derived by combining Eqs. (3) and (20) in differential form. Lebedev *et al.* suggested that arrays with the same value of *K* might have the same deviation of wire arrays from thin-shell trajectories and the same radial redistribution of ablated mass. The variable *K* is $\propto \langle V_{\mathrm{array}} \rangle / V_a$, where $\langle V_{\mathrm{array}} \rangle$ is the average array implosion velocity. As *K* increases, the array motion approaches a thin-shell limit, with less radial extent of the injected mass (large array velocity, small ablation velocity, and a large ablation rate) [91].

The ablation rate per unit mass, f_m, is $\propto \Pi K/\tau_{\mathrm{stag}} \propto I_m^2/[R m_0 V_a]$. Higher values of Π and *K* and shorter τ_{stag} or higher peak drive current, smaller array mass m_0, and smaller ablation velocity V_a lead to a higher ablation rate per unit mass and therefore a shorter absolute time for wire burnthrough. If the array mass is scaled to keep the stagnation time constant, then $m_0 \propto R^{-2}$ and $f_m \propto R$. The normalized current wave forms [Eqs. (18) and (19)] are higher for *Z* on both the absolute and normalized time base; hence, *Z* arrays ablate through at a faster rate than Magpie, even for the same value of $\Pi K/\tau_{\mathrm{stag}}$.

The fraction of the total initial array mass that is ablated, f_a, can be found by integrating $f_m(t)$:

$$\frac{\delta m(t)}{m_0} = f_a(t) = \frac{\Pi K}{\tau_{\mathrm{stag}}}\int_0^t \left(\frac{I_\ell}{I_m}\right)^2 dt. \tag{22}$$

Integrating Eq. (22), we find for Eq. (18) the following expression [42,44] for the mass ablation fraction for the $\sin^2$ current pulse, appropriate for Magpie:

$$f_{aM}(t) = \frac{3\Pi K}{8}\left[\left(\frac{t}{\tau_{\mathrm{stag}}}\right) - \frac{4\beta}{3\pi}\sin\left(\frac{\pi t}{\beta\tau_{\mathrm{stag}}}\right) + \frac{\beta}{6\pi}\sin\left(\frac{2\pi t}{\beta\tau_{\mathrm{stag}}}\right)\right] = \frac{3\Pi R}{8 V_a \tau_{\mathrm{stag}}} g_M(t). \tag{23}$$

Lebedev *et al.* also presented a similar analysis [91], and we adopt his notation. For Eq. (19) we find, appropriate for *Z*,

$$f_{aZ}(t) = \frac{\Pi K}{2}\left[\frac{1}{\beta^2}\left(\frac{t}{\tau_{\mathrm{stag}}}\right)^3 - \frac{1}{7\beta^6}\left(\frac{t}{\tau_{\mathrm{stag}}}\right)^7\right] = \frac{\Pi R}{2 V_a \tau_{\mathrm{stag}}} g_Z(t), \tag{24}$$

where the variable $\beta = t_m/\tau_{\mathrm{stag}}$ is introduced to express Eqs. (23) and (24) in terms of t/τ_{stag}.

TABLE VI. Mass ablation rate fitting for Magpie and *Z* tungsten arrays. We apply the fitting technique of Eq. (23) to Magpie tungsten array trajectory data from Refs. [28,32], and Eq. (24) to *Z* tungsten trajectory data to find the product of ablation fraction f_a and ablation velocity V_a.

Array	Π	τ_{stag} (ns)	t_a/τ_{stag} t_a (ns)	β	$g(t_a/\tau_{stag})$	f_aV_a (cm/μs)	V_a (cm/μs)	K
Magpie tungsten array data (Refs. [28,32])[a]								
64 wires	7.4	270	0.78	0.89	0.705	5.8	14.5	0.20
			220				(f_a=0.4)	
32 wires	10.7	230	0.79	1.04	0.516	7.2	18.0	0.19
			190				(f_a=0.4)	
16 wires	16.1	200	0.78	1.2	0.351	8.5	21.3	0.19
			165				(f_a=0.4)	
Z tungsten array data								
12-mm	5.57	100.5	0.74[b]	0.90	0.469	7.8	16.6	0.36
			74				(f_a=0.47)	
20-mm	5.17	95.5	0.61[c]	0.94	0.253	6.8	14.5	0.72
			58				(f_a=0.47)	
40-mm	4.92	106.6	0.52[c]	0.85	0.192	8.8	21.5	0.87
			55				(f_a=0.41)	

[a]In order to define the stagnation time for Magpie experiments of Refs. [28,32] in the same manner as for *Z* experiments (based on the extrapolated leading edge of the current; see Fig. 3) subtract 40 ns from τ_{stag} and t_a. Only the values of t_a/τ_{stag} above are already corrected for this shift.
[b]No optical measurement available. This number is from the electrical measurement of Table II (Sec. II E).
[c]These fractions are the average of electrical (Sec. II E) and ROS measurements from Table II and near the starting times used for the rocket model results in Table V.

Table VI summarizes the analysis of Eq. (23) as applied to Magpie tungsten array data from Refs. [28,32] and Eq. (24) applied to the *Z* array data. We measure the time at which the array accelerates from its initial position, t_a, the array implosion time, τ_{stag}, and know the variables Π and R based on the initial setup of the accelerator and wire array. We can therefore solve Eqs. (23) and (24), with the product of ablation fraction x ablation velocity ($=f_aV_a$) as the only unknown. Using fits to the trajectory and power, discussed in Secs. IV B–IV D, we estimated that the ablated fraction f_a was 41%–47% at the moment of initial acceleration. This was similar for Magpie arrays ($f_a \sim 40\%$) [32].

The ablation velocity obtained in this way can be thought of as giving the average or effective ablation rate along the length of the wire, taking into account axially nonuniform ablation. This velocity is not necessarily the actual velocity of the ablated mass. Figure 18 plots t/τ_{stag} for tungsten arrays on *Z*, versus $g_Z(t)=2f_aV_a\tau_{stag}/(\Pi R)$ from Eq. (24). The data points are plotted at the experimentally observed t_a/τ_{stag} and at the required f_aV_a to fit the acceleration by the ablation of a given fraction f_a of the initial array mass, giving a graphical solution to Eq. (24). The curves are similar to each other because the experimental conditions were changed to keep Π and β roughly constant.

As the wire number increases (wire-to-wire gap decreases) in the Magpie experiments, the required ablation velocity from a solution to Eq. (23) decreases (increasing wire ablation rate) [91,81]. In a similar way, ablation velocities are smaller for the 12-mm and 20-mm arrays compared to the 40-mm array perhaps because of the smaller wire-to-wire gap [91]. The ablation velocities for the 12-mm and 20-mm arrays are approximately equal, perhaps because of identical wire-to-wire gaps. The ablation velocities on *Z* approach those for the higher wire number Magpie arrays. The effective ablation velocities show small changes over large changes in experimental conditions between *Z* and Magpie [81].

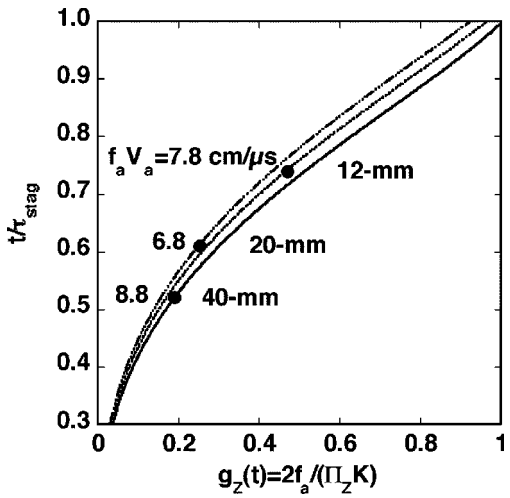

FIG. 18. Plot of t/τ_{stag} vs g_Z [Eq. (24)] for *Z* tungsten arrays. Array mass and radii were changed to keep the measured implosion time roughly constant (Π roughly constant).

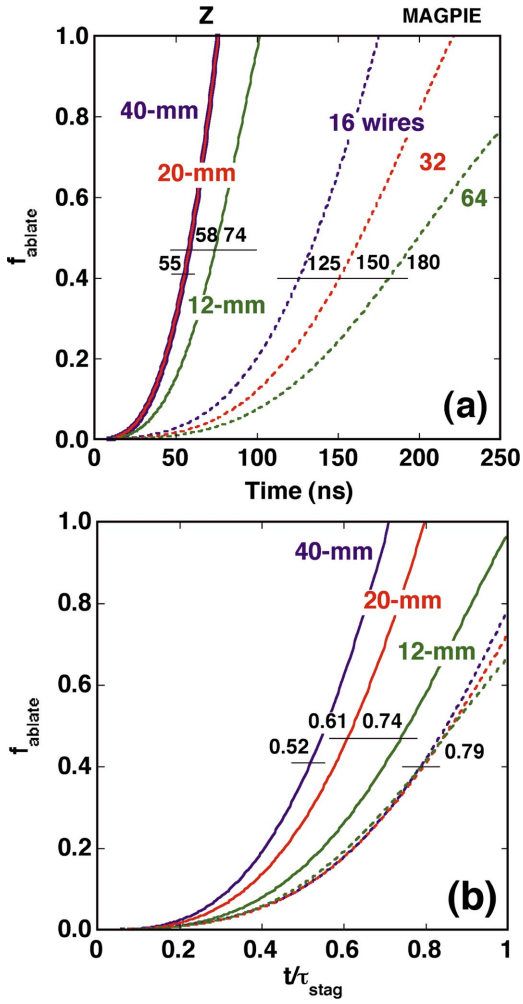

FIG. 19. (Color) (a) Mass ablation fraction as a function of time for *Z* (solid lines) and Magpie arrays (dotted lines). The value of V_a was adjusted to produce agreement with the measured time of acceleration at the appropriate value of the ablation fraction. Ablation fractions are noted with horizontal lines (41% for the 40-mm array, 47% for the 20-mm and 12-mm arrays, and 40% for Magpie; see Table VI). Magpie curves and acceleration times are shifted earlier by 40 ns so that the $t=0$ point is defined in a similar fashion for both *Z* and Magpie. (b) Mass ablation fraction as a function of normalized time (t/τ_{stag}) for *Z* (solid lines) and Magpie arrays (dotted lines). The Magpie acceleration and stagnation times from Table VI were decreased by 40 ns in calculating the t_a/τ_{stag} ratio. Magpie arrays ablate and burnthrough later in the pulse than *Z* arrays.

Using the results of this analysis (e.g., the particular f_aV_a and K values found above), Fig. 19 plots the mass ablation fraction for these six arrays versus time [Fig. 19(a)] and versus the normalized time [t/τ_{stag}, Fig. 19(b)]. These curves were adjusted to pass through the measured ablation time t_a [in Fig. 19(a)] and the measured t_a/τ_{stag} [in Fig. 19(b)] at the relevant ablation fraction by selecting a different value of V_a for each curve (see Table VI).

The normalized and absolute ablation times appear to decrease inversely with the ablation parameter K; e.g., the higher K, the earlier in the current pulse the array begins implosion. Arrays on Magpie ($K_M\sim 0.20$) start to implode at $(0.76–0.82)\tau_{\mathrm{stag}}$. *Z* arrays ($K_{20}\sim 0.72$, $K_{40}\sim 0.87$) have an increased ablation rate per unit mass compared to those on Magpie largely because of smaller τ_{stag} by $\sim$2.5, ablate through, and begin implosion earlier [$(0.52–0.60)\tau_{\mathrm{stag}}$]. Arrays on Angara-5-1 with a similar K to Magpie ($K_A\sim 0.30$) also show a delayed trajectory ($\sim 0.80\tau_{\mathrm{stag}}$) [34–36]. In this case, although the stagnation time is similar to the $\sim$100 ns on *Z*, the ablation rate per unit mass is smaller because of a smaller array diameter (8 mm) by a factor of 1.5–5. The 12-mm-diam array on *Z* ($K_{12}\sim 0.36$) had an ablation rate per unit mass ($\propto 1/[m_0RV_a]$) smaller by 46% compared to the 20-mm *Z* array, and so burned through and accelerated relatively later, approaching the Angara and Magpie results. These results presented in Table VI are strong evidence in favor of the hypothesis by Lebedev *et al.* in Ref. [32], concerning scaling of the wire array trajectory with the parameter K.

These equations make it apparent that if the rocket ablation model is correct in a global or average sense, there should be a one-to-one correspondence between measured values of the ablation time t_a and the product f_aV_a. We determine the values of ablation velocity required to fit the experimentally measured ablation times by construction. Direct measurements of the flow velocity of the plasma precursor on Magpie with axial interferometry [32] showed that $V_a=15$ cm/μs, roughly consistent with the above analysis using $f_a\sim 40\%$ and, in turn, possibly consistent with the observed high periodicity of the axially nonuniform ablation [32].

If V_a could be directly measured experimentally, it might give insight into whether the rocket model is a reasonable representation of the effective or global ablation rate and, if so, help to determine the fraction of the array mass ablated prior to acceleration. Also x-ray backlighting or shadowgraphy [50,51] could provide direct measurements of f_a. Recall we inferred values of the ablation velocity based on the requirement to provide a density ramp towards the axis, generating inelastic power in agreement with the measurement (see Sec. IV D). These values of velocity (14 ± 3 cm/μs for the 20-mm and 27 ± 3 cm/μs for the 40-mm array) are in reasonable agreement with those from the above analysis. Direct measurements of V_a are critically important to provide an independent confirmation of the above model.

Direct experimental measurements of how V_a might scale with experimental conditions such as array geometry (radius, array mass, number of wires, wire diameter), accelerator configuration (I, dI/dt, current prepulse length and amplitude), as well as on wire material or wire alloy properties (such as conductivity, EOS, and other factors possibly seeding the growth of the nonuniform ablation) would also be helpful. The ablation velocity apparently strongly controls the dynamics of the array, but has shown significant variations only to wire number in 2D-MHD simulations [81]. Also the source of the initially nonuniform ablation is unknown. If V_a could be decreased or, equivalently, if f_a could be increased, higher values of K would result, burning through the array at an earlier fraction of the stagnation time, possibly resulting in a reduction of trailing mass.

Presently, lacking any obvious experimental control over either the product f_aV_a, f_a, or V_a, these equations still give

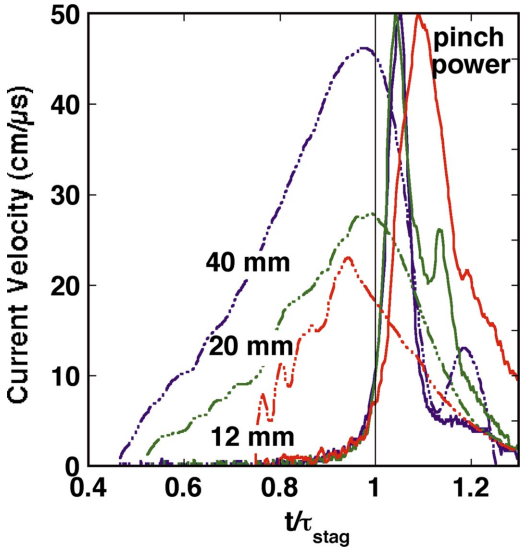

FIG. 20. (Color) Comparison of the effective velocity of current compression (dotted lines) with the normalized power pulses (solid lines) for the 40-mm (blue, shot 846), 20-mm (green, shot 818), and 12-mm-diam (red, shot 931) arrays. We observe a later acceleration time for smaller radius arrays. Faster initial acceleration of the current and a longer time between peak velocity of the current and peak power for the 12-mm array may indicate a higher trailing mass compared to the other arrays. Faster deceleration of the current near peak velocity for the 40-mm array may indicate less trailing mass compared to the other arrays.

guidance on an appropriate direction to increase the ablation rate per unit mass. Based on Eq. (21), a high ablation rate per unit mass requires high Π, high K, and short τ_{stag}. Fixing the radius relevant to a particular application [10], only a decrease in the initial array mass or an increase in the driving current (or both) can modify the ablation rate per unit mass.

V. PHASE IV: STAGNATION AND THERMALIZATION

A. Current compression velocities and stagnation times

The effective velocity of current compression can be obtained by differentiating the effective current radius curves. Figure 20 plots the effective velocities of the current compression for the 12-mm, 20-mm, and 40-mm arrays, with the soft x-ray pulse shape for comparison. We find that the peak velocity of compression of the mean current radius (28 ± 2 cm/μs) for the 20-mm array (green line, Fig. 20) is lower than the velocity of the emission front near the axis (40 cm/μs) [Fig. 6(a)]. The same is true for the 40-mm array. The peak velocity of current compression is 46 cm/μs (blue line, Fig. 20) for the 40-mm array. The peak velocity of the current is lower than the velocity of the emission front at 62 cm/μs [Fig. 7(a)].

The effective current velocity for the 40-mm array is an underestimate of the peak velocity, considering the previous discussion about increased AK gap current loss for the 40-mm array, relative to the 20-mm array. The current velocity of the 20-mm array is also likely an underestimate. We saw in Sec. IV C that the inductance trajectory still lagged behind the rocket model and the measured edge of the mass distribution with the ROS and XRPHC, including all the mass [Fig. 15(b)].

The time at which the current reaches peak velocity in both cases is 3–6 ns later than the observed time of merger of the peak of the radial x-ray profile (axial view with XRPHC) with the precursor and just prior to the stagnation times of the arrays. For the 20-mm array, the velocity of the current peaks at -0.4 ± 1.7 ns prior to τ_{stag}, while the peak of the radial x-ray profile merges with the precursor at -3.8 ± 1.9 ns prior to τ_{stag}. For the 40-mm array, the velocity peaks at -2.6 ± 0.9 ns prior to τ_{stag}, while the peak of the radial x-ray profile merges with the precursor at -8.6 ns prior to τ_{stag}. After this time, the rate of pinch current compression decreases, perhaps because of the stagnation pressure increase as most of the mass is compressed and heated on axis or because of the onset of instabilities which spread the sheath. The effective velocity of the current compression at peak pinch power is always lower than and later than the peak velocity of the current.

These observations are further evidence consistent with the hypothesis that the collision of the shell with the precursor begins the pinch thermalization phase (IV). Recall that we chose the extrapolated leading edge of the pinch power as a convenient method to define the start of the pinch thermalization phase (IV) (Sec. II B). This was useful as a demarcation of rapid power increase, but arbitrary. A physically motivated criterion might be when the shell strikes the precursor or when the acceleration of the current compression is observed to decrease. These three observations are within 3–9 ns of each other for both arrays.

Figure 20 also shows that the peak velocity of current compression for the 12-mm array is 23 cm/μs (red line) and that this occurs 14.5 ns prior to peak radiation. This is the longest time delay between peak velocity of the current and peak radiation for any of the single arrays discussed in this paper. The rate of current transfer to the axis and rate of compression appears to decrease for the 12-mm array. For example, compare with a 5.8 ± 1.8 ns delay between peak velocity of the current and peak power for the high-current 20-mm arrays. This might be consistent with a larger trailing current and mass for arrays with a longer wire ablation period.

If the fraction of trailing mass for the 12-mm array is the same as we inferred for the 20- and 40-mm arrays (30% at the foot of the power pulse; see Sec. IV B), as much as 4.5 mg may be trailing (0.3×14.9 mg). This is a factor of 2.5 times that inferred for the 5.9-mg, 20-mm array, in absolute quantity. Interestingly, the acceleration of the current (dv/dt from Fig. 20) for the 12-mm array is highest, implying the smallest involved mass and thus indirectly indicating a higher fractional (and absolute) trailing mass than the 20- and 40-mm arrays. This is consistent with our speculation that the fraction of trailing mass could increase for longer ablation periods. Magpie arrays ($t_a\sim0.8\tau_{stag}$) were estimated to have a trailing fraction as high as 40%. If this fraction applies to the 12-mm array on *Z*, as much as 6 mg might be trailing. This is a factor of 3.4 increase in absolute quantity compared to the 20-mm array.

If we assume that the "clearing time" for final compression of the trailing mass is proportional to the time period between peak velocity of the current and peak power, we can use Eqs. (7) and (8) to estimate the required increase in trailing ion density. Compared to the 20-mm array, a factor of $14.5/(5.8\pm1.8)=2.5\pm0.8$ increase in the final compression or clearing time requires an increase in trailing ion density by a factor of 6.3 ± 4. This is within a factor of 2–3 of the 2.5–3.4 increase in trailing mass estimated above, based the assumption of 30%–40% trailing mass fractions from rocket model fitting.

Further data consistent with a change in the radial distribution of the current are obtained by comparing inductance unfolds for the low-current and high-current cases from the recent current scaling work of Stygar *et al.* [20]. In that work, scaling of power with current was determined for 20-mm-diam tungsten wire arrays with a fixed implosion time (95 ns). Radiated power scaled subquadratically with current ($\propto I^{1.24\pm0.18}$) between 13 MA (2.7 mg/cm) and 19 MA (5.9 mg/cm) where only array mass and current were varied. Multiple-shot averages of current trajectories [57] and velocities for the low- and high-current cases of this data are compared in Fig. 21. This is a better relative comparison than the 20-mm and 40-mm cases discussed previously since we used identical and large AK gaps (3 or 4 mm) for which no discernible effects of AK gap on radiated power and energy were observed.

The comparison of current trajectories and velocities in Fig. 21 indicates a tighter pinching of the current for the lower-current array, as well as a higher implosion velocity of the current. At peak radiated soft x-ray power, the radius and CR of the current are, respectively, 1.4 ± 0.4 mm and 7.1 ± 2.0 for the lower current case (average of three shots). The radii and CR of the current are 2.8 ± 0.4 mm and 3.6 ± 0.6 for the higher current case (average of three shots), showing reduced compression. We measure a peak velocity of the current compression of 35 ± 0.3 cm/μs for the low-current case (approaching the thin-shell model limit of 40 cm/μs at a 10:1 compression) and 28 ± 2 cm/μs for the high-current case. Were the arrays behaving as a thin shell, a fixed stagnation time scaling would result in identical trajectories, compression ratios, and implosion velocities for the two currents.

Figure 22(a) compares time-dependent FWHM from the radial XRPHC camera with the soft filter, for both low- and high-current shots. The time axis is plotted as time with respect to the peak power. The final compression of the FWHM from of order 4–5 mm down to 1 mm occurs in about 2–3 ns for the low-current case, at about 45 cm/μs, consistent with the peak velocity of compression of the current [35 cm/μs, Fig. 21(b)]. The final compression of the FWHM for the high-current case occurs in about 5–7 ns, about a factor of 2 slower than the low-current case, but at a factor of 5 reduced velocity (9 cm/μs). The peak velocity of current compression for the high-current array is 28 cm/μs [Fig. 21(b)].

We argued in Sec. IV B that the wings on the mass density profile at stagnation determine the final compression time (Fig. 11) and that the size of the wings are relevant to the compression (and final velocity) of the current at peak power. The wings are below the level of the FWHM [Fig. 11(a)]. The difference between the peak velocity of compression of the FWHM (9 cm/μs) and that of the current for the high current case (28 cm/μs) argues for a reduced efficiency of compression and heating of the main pinch mass on axis. Since the velocity of FWHM compression for the low current case (45 cm/μs) is consistent with the final current compression velocities (35 cm/μs), we would therefore infer a lower mass distributed in wings to delay the final compression. A reduction in trailing mass and in the time period for compression is consistent with the shorter rise time of the power pulses for the lower-current case, shown in Fig. 22(b). A reduction in trailing mass is also consistent with the smaller delay between the peak current and stagnation time ($t=1.0\tau_{stag}$) for the low-current case [Fig. 21(b)] and with the faster deceleration of the current after peak velocity for the lower-current case [Fig. 21(b)]. [In a similar way, the deceleration of the current after peak velocity for the 40-mm array

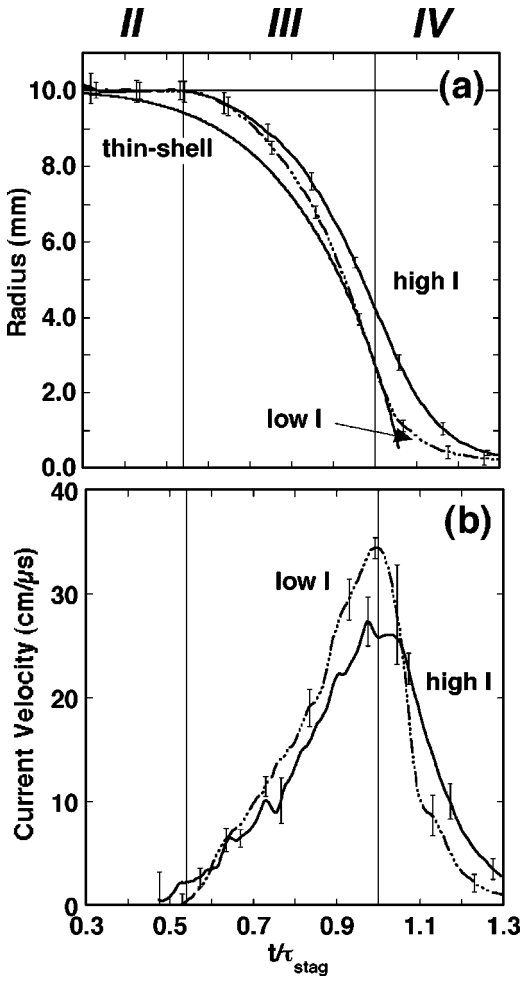

FIG. 21. (a) Comparison of the trajectory of the effective position of the current from the current scaling experiment of Ref. [20]. Wire array experiments at 13 MA (dashed line, average of shots 725, 819) and 19 MA (average of shots 724, 817, 818). Higher convergence is noted for the lower-current case. (b) Effective velocity of current compression for the trajectories from part (a). A higher peak velocity and a more rapid deceleration of the velocity near peak power is observed for the low-current data.

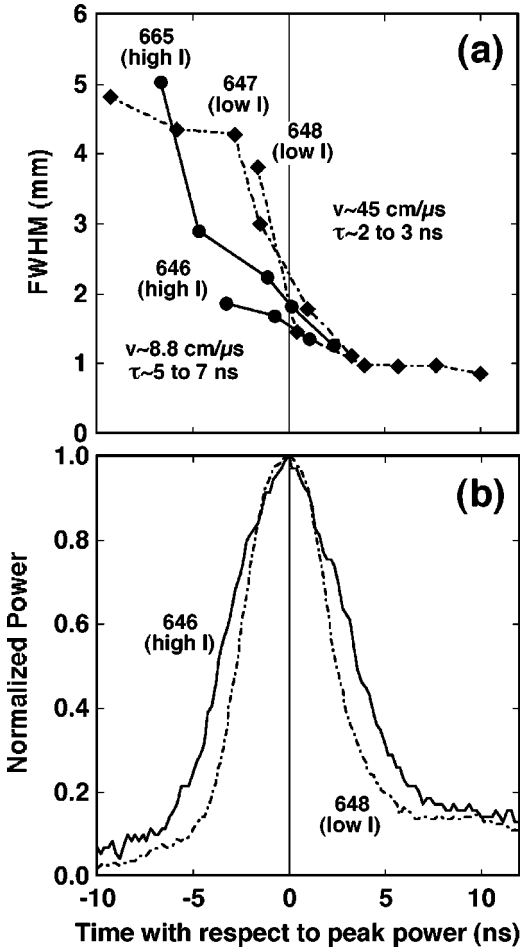

FIG. 22. (a) Comparison of the pinch FWHM obtained from the soft-filtered radial x-ray pinhole camera data for low-current (dashed lines with diamonds, shots 647 and 648) and high-current (solid line with circles, shots 646 and 665) configurations. (b) Pinch power pulse at low current (648) and high current (646), both with otherwise identical hardware configurations and AK gaps (1 mm). The low-current arrays implode faster, correlated with a narrower, faster rising pinch power pulse.

is faster compared to the 20-mm and 12-mm arrays (Fig. 20), also consistent with smaller trailing mass.]

B. MHD stability at stagnation

In Figs. 10(b)–10(d), the structure of the hot spots and the shape of the intensity contours (white lines) appear to show an instability with an $m=0$ sausagelike character growing up rapidly during the pinch power rise time. These images are obtained after the beginning of phase IV (e.g., $>\tau_{\mathrm{stag}}$, after the acceleration of the system has ceased); thus, an $m=0$ MRT mode is not indicated. This sausage mode may be initiated by the wavelength of the axially nonuniform ablation set by the ablation process at the array edge and/or by an MRT wavelength at stagnation [24]. Axial profiles from Fig. 10(a) (not shown) suggest that $\lambda \sim 1.8$ mm just prior to stagnation.

A pinch with current and pressure profiles peaked on axis is stable to the $m=0$ sausage instability [110–112]. However, since the effective radius of the current is off axis (at 2.8 mm), the pinch mass at stagnation is unstable to both the $m=0$ sausage and $m=1$ kink perturbations [111,112]. Trailing mass and distributed current, however, do reduce the growth rate of $m=0$ and $m=1$ instabilities by creating a broader, more diffuse current profile [113,114].

The overall shape of the bright core region or intensity contours also clearly show the onset of a mild $m=1$ kink instability in Figs. 10(d) (just after peak power) and 10(e). The radius of peak emission as a function of axial position (defined as the pinch centroid) is plotted as the green line in Figs. 10(b)–10(i). The centroid shows an overall $m=1$ instability with a wavelength of about the pinch length. An $m=1$ kink, when observed, is always on all frames obtained after peak power, never on frames before, for the 20-mm arrays. Thus there may be some relation between the occurrence of $m=1$ and the termination of the rapid rise of the power pulse.

The peak compression of the self-emission is always after peak power (see Fig. 10) and hence also associated with the appearance of the kink. The peak radiation temperature of the pinch after peak power is similar to those at peak power, but the total power radiated lower, perhaps because of a smaller surface area. Perhaps one reason the total radiated pinch power begins to decrease is simply because of the final assembly of all the mass into a tighter pinch after peak power. The conditions for the maximum growth of the kink instability may not occur until peak compression is reached. Also, the growth rate of the kink instability may be somewhat lower than for the sausage, independent of the current profile [113,114]. The spectra of the pinch emission become progressively harder throughout the pulse, in particular after peak power, possibly related to the growth of MHD instabilities and the production of axially directed electron beams between the cathode and anode.

On a more speculative note, we observe in Figs. 10(c) and 10(d) the presence of a number of "bubble" regions, defined for this discussion as cold regions surrounded by hot material. These bubble regions, labeled "b1"–"b3" in Fig. 10, appear to be correlated frame to frame and are similar to structures produced in nonlinear simulations of the $m=0$ sausage mode in 2D by Vikhrev *et al.* [115]. Vikhrev *et al.* proposed that the sausage mode could produce small bubblelike torroidal cavities in a compressed cylindrical pinch on axis. Rudakov *et al.* and Velikovich *et al.* [75,76] (RV) further proposed that should these torroidal cavities close off or bridge at the entrance and trap some current that the buoyant transport of the bubbles or magnetic flux tubes to the axis deposits energy in the *z*-pinch plasma through either displacement work (PdV) or drag heating (viscosity). This was proposed as a mechanism that might account for the total radiated energy by pinches up to $2\times$–$4\times$ the kinetic energy at stagnation.

For example, we see a bubble "b1" in Fig. 10(c), which appears to correlate with a similar feature in Fig. 10(d). This bubble apparently fails to form a closed cavity and does not appear torroidal (axis enclosing). Bubble "b2" observed in Fig. 10(c) appears to compress in Fig. 10(d) and also appears

to be torroidal in the harder filtered image of Fig. 10(h). In Fig. 10(e) this bubble has disappeared, but the associated hot spot has increased in intensity. The cluster of three bubbles "b3" in Fig. 10(c) appears to shrink and merge by the time of Fig. 10(d), and is correlated with an increase in intensity of this hot spot. These bubble regions are observed in all pinhole pictures at peak power.

The RV mechanism must have a source of convective MHD instability—for example, an $m=0$ sausage—to provide the magnetic field curvature required to drive the bubbles toward the axis [75]. The radial XRPHC data convincingly demonstrate the existence of some kind of MHD instability with a dominant $m=0$ character. The obviously 3D pinch structure and the presence of trailing mass and current imply that the application of this mechanism, in practice, should take into account 3D effects and the actual profile of trailing current. The RV enhanced power is increased for higher Alfvén velocity, e.g., at larger magnetic fields (higher current, smaller radius) and for smaller pinch masses. A faster rate of increase of magnetic field near the axis (higher current, smaller radius) is obtained for decreased trailing mass. Decreased trailing mass may also be obtained in general, for lower initial load masses.

There may be a relationship between trailing mass and current [faster final compression time scales for higher V_A, $\tau_C \sim 1/V_A$, Eqs. (7) and (8)], an increase in MHD growth rates Γ near the axis ($\Gamma \sim V_A$) [89], and increased coupling of magnetic energy into pinch power on the time scale of the initial thermalization or pinch power rise time ($P_{\mathrm{RV}} \sim I^2 V_A/R$) [75,76]. Although there is no generally agreed upon pathway for pinch plasma heating by the magnetic energy on axis at stagnation, it is agreed that the coupling of magnetic energy is critical to explain the large radiation yields of *z* pinches. Any mechanism coupling magnetic energy into the pinch at a velocity proportional to the Alfvén velocity should likewise be improved by these kinds of modifications.

C. Possible signature of trailing mass in pinch power pulse shapes

We speculate about signatures of trailing mass and current in observed x-ray power pulse shapes. X-ray pulse shapes have a secondary pulse or tail in general; e.g., see Fig. 3 or 6(b). Figure 23 compares the normalized soft x-ray pulse shapes for a variety of single wire arrays, averaged over multiple shots. The secondary pulse or tail is smaller for smaller AK gaps and for hotter feed electrodes [6,20] because of a decrease in the driving current resulting from AK gap current loss or complete AK gap closure. We speculate that the amplitude of the secondary pulse on the radiated power might also be related, in part, to secondary implosions of trailing mass and current or to reduced pinch compressibility. A larger tail relative to the peak power could correlate with increased trailing mass and current. If true, this would imply the converse: increased power in the main pulse relative to the tail correlates with improved simultaneity of arrival of the current and mass at the axis.

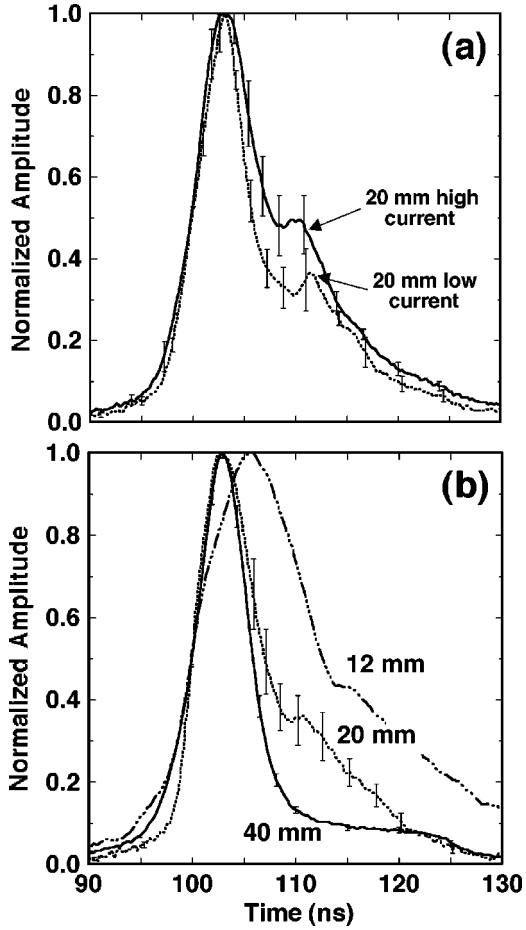

FIG. 23. (a) Comparison of normalized radiation power pulse shapes for the current scaling experiments of Ref. [20]. Normalized power pulses from 3- and 4-mm shots are averaged. High-current shots are 594, 683, 723, 724, 817, 818. Low-current shots are 647, 725, 819. (b) Comparison of normalized radiation power pulse shapes for three different initial array diameters: 12 mm (dashed line, shot 931, 3-mm AK gap), 20 mm (dotted line, average of shots 719, 726, 728, 747, 749, 3-mm AK gap), and 40 mm (solid line, average of shots 160, 161, 165, 168, 169, 234, 235, 269, 281, 326, 394, 5-mm AK gap). The power pulses are aligned with the 50% point on the leading edge at 100 ns. Peak radiated power for the 12-mm array is ~50 TW, for the 20-mm array ~125 TW, and for the 40-mm array ~165 TW. Error bars are reduced by $\sqrt{N-1}$ for a sample of *N* independent measurements. Larger relative tail amplitude is observed for arrays with greater trailing mass.

Figure 23(a) compares pulse shapes for the 20-mm low-current and 20-mm high-current arrays from the current scaling study of Ref. [20]. We average multiple shots all with 3- and 4-mm AK gaps. The multiple soft x-ray pulse shapes are normalized to peak power ($\equiv 1$) and then aligned in time at half peak amplitude (0.5). The averaged curves are found by averaging the values of each curve as a function of time. The peak power and total energy are constant at these large AK gaps, so changes in the amplitude of the late time tail are not due to variations in AK gap current loss. In Fig. 23(a), a smaller tail (and smaller FWHM) is observed for the low-current experiments that had a higher implosion velocity of

the current and a tighter pinching of the current at peak power.

Figure 23(b) compares normalized pulse shapes for 12-mm, 20-mm, and 40-mm single arrays. Except for the 12-mm case, these data are multiple-shot averages. These experiments all have approximately the same ratio of d_0/R representative of the initial magnetic insulation strength of the feed gap. The insulation for the 12-mm array is about 20% stronger than the 20-mm case. The insulation for the 40-mm array is about 30% weaker than the 20-mm case. The secondary pulse is a smaller fraction of the peak power for arrays that ablate and accelerate sooner. In particular, the 10% tail for the 40-mm array is much smaller than the 35% for the 20-mm array. Although the 40-mm array probably shows increased AK gap current loss relative to the other two arrays, which would decrease the tail, the much lower tail is also consistent with less trailing mass and an improved simultaneity of implosion of the current and mass. Increased FWHM of the radiated power is correlated with longer ablation periods.

This argument does not suggest what mechanism generates the late-time radiation, just that it may be correlated with the implosion of an array with trailing mass profile and the arrival of all the current near the axis. The pinch is more tightly compressed during the tail of the pulse (Figs. 10 and 23). Spectrally resolved x-ray emission data indicate that the radiation from the tail has a significantly harder spectrum than the main pulse. The energy in the tail of the radiation pulse, possibly associated with the arrival of trailing mass and current, might be useful for ICF if we can understand the generation mechanism and thermalize this energy on a more rapid time scale during the main pulse to increase the peak power and improve the scaling of pinch power with current.

VI. SUMMARY AND DISCUSSION

In summary, for high-wire-number, single, tungsten arrays at 17–19 MA, at diameters of 12–40 mm, with masses >2 mg/cm we show a number of discrete-wire implosion characteristics. The wire arrays from which the particular observations are derived are noted in parenthesis in the list below. We observe the following: (1) a precursor pinch on the axis of the array and cold tungsten in the center (20-mm, 40-mm arrays); (2) a long wire ablation period (12-mm, 20-mm, 40-mm arrays); (3) a corresponding delayed acceleration of the wire array edge from that of a thin-shell (12-mm, 20-mm, 40-mm arrays); (4) a wide imploding shell-like object early in the implosion, possibly prior to significant MRT growth (20-mm array); (5) a plateau or shelf of trailing hot mass during the implosion out to the limit of the field of view (8.7 mm), early in the implosion (20-mm array); (6) other indirect and direct evidence for trailing mass and a tail on the mass density profile at the outer radius, rather than a sharp edge (20-mm, 40-mm arrays); (7) a ramp up of the power from 0.1 to 5 TW during the implosion phase (12-mm, 20-mm, 40-mm arrays); (8) a limited compression ratio of the current at stagnation (trailing current) and smaller implosion velocities of the current compared to a thin-shell model (12-mm, 20-mm, 40-mm arrays); (9) a cold halo of material at a diameter consistent with the trailing current, around a smaller diameter hot core or hot spots, at stagnation (20-mm array); and, (10) low-density material at the array edge and an axial modulation of the late time density at the edge of the array, at stagnation (40-mm array).

Trailing mass at the array edge early in the implosion appears to produce wings on the mass density profile at stagnation once compressed. These wings, which may contain of order 30% of the total array mass according to simple trajectory models, impact the final compression and thermalization rate. We observe the growth of an instability with an $m=0$ sausage character growing up rapidly during the rise of the power pulse. We also see a mild $m=1$ kink instability near to, but always after, peak x-ray power, correlated with a tighter compression of the self-emission, increasingly harder pinch x-ray emission, and the emission of hard x rays >100 keV.

In contrast to work where the array accelerated from its initial radius very late in the pulse ($\sim$80% of the stagnation time) [25–40], our results show that very late acceleration is not a universal aspect of wire array behavior. We demonstrated a scaling of wire array trajectories, for the first time, and varied the wire ablation time between 46% and 71% of the array stagnation time by changing the initial diameter of the wire array at constant implosion time. Wire arrays on *Z* have a higher ablation rate per unit mass, and ablate and implode earlier in the current pulse compared to arrays on Magpie and Angara-5-1.

The behavior of the arrays is dominated by the long wire ablation period, even for the smallest wire-to-wire gaps used on *Z* (209 μm for the 20-mm array). This suggests that two-dimensional (*r*-*z*) models that implicitly assume wire ablation and wire-to-wire merger into a shell on a rapid time scale compared to wire acceleration are incorrect, or incomplete, for high-wire-number, massive (>2 mg/cm), single, tungsten wire arrays. These results also suggest that 2D(*r*-*z*) models of nested wire array behavior [23,48] may be incomplete and that the possible impact of discrete-wire behavior of the outer and inner arrays should be evaluated [29].

The primary significance of this work is improved understanding of the 3D conditions during wire initiation, wire ablation, and array implosion, during the first 97% of the array implosion history. This work leads to a more quantitative understanding of what the initial conditions for pinch thermalization (plasma heating and radiation rates) and the termination of the radiation pulse are and how they are set up near the axis of the array at 20 MA.

Although we have an improved understanding of the wire array dynamics, both 2D and 3D models still require that we assume initial conditions to generate, for example, the axial perturbation on the individual wires (e.g., see Ref. [80]). Also we were able to match the wire array ablation rates observed in experiments, only with adjustable constants within the material models used in the 2D-MHD codes. No simulations are as yet entirely *ab initio*. We need improved material models to begin to understand the long-lived wire cores. The key initial conditions need to be adequately determined and characterized to achieve a truly predictive capability for scaling pinch output to higher currents and to de-

termine how to optimize wire-array implosions and scale the parameters.

High peak radiated power requires rapid and simultaneous assembly of mass and current on the axis. We see clear differences in the velocity and simultaneity of assembly between the current and radiation emission for the various array configurations discussed. We infer a somewhat higher fraction of trailing mass at the start of stagnation for arrays with a longer wire ablation period by comparing rocket model fits on Magpie (40% trailing) with *Z* (30% trailing for the 20-mm and 40-mm arrays). However, there is not a very strong change in the fraction. Within the error of the estimates from the rocket model it is possible that all the arrays simply leave a fixed fraction of trailing mass. The longest delay between peak velocity of the current and peak radiation was observed for the 12-mm array, the heaviest array with the longest ablation period. The 12-mm array had the largest acceleration, implying the largest absolute trailing mass and a larger fraction of trailing mass compared to the 20-mm and 40-mm arrays. We also observe a correlation between longer wire ablation periods and arrays with larger FWHM and increased tail power relative to the peak power.

We observed a slower apparent velocity of the current, a lower convergence of the current at peak radiation, and a longer delay between peak velocity and peak radiation for the high-current 20-mm case compared to the lower-current 20-mm case, consistent with an increase in trailing mass and current for higher-mass arrays. We showed that the trailing mass at the edge of the array leads to wings on the mass profile at stagnation for the 20-mm array, causing a slower rate of current transfer to the axis of the array and therefore a slower rate of increase of the magnetic energy density ($L_a I^2/2$) and magnetic pressure near the axis. This could reduce the rate of delivery of magnetic field energy available for conversion to radiation.

Trailing mass [32,85] leading to trailing current [36] is therefore proposed as the most likely cause of the subquadratic scaling of radial power with current ($\propto I^{1.24}$) for massive ($\geqslant$2.5 mg/cm) 20-mm arrays ($\tau_{\mathrm{stag}} \sim 95$ ns) observed by Stygar *et al.* [20]. As further support for the conclusion that trailing mass results in slower scaling of power with current, we note that the radial power scales quadratically with array current ($\propto I^2$) for lighter ($\leqslant$2 mg/cm) 40-mm arrays ($\tau_{\mathrm{stag}} \sim 105$ ns) in the experiments of Nash *et al.* [78]. Recall that the 40-mm arrays were estimated (Sec. IV B) to have only $36\% \pm 6\%$ of the absolute trailing mass per unit length of the 20-mm array using rocket model fits to trajectory data. Lower trailing mass correlates with the improved power scaling with current.

We need improved characterization of pinches at stagnation to test models of pinch thermalization and radiation termination. MHD simulations are primarily predictions of the location of mass and current; properties of radiation are second-order predictions of radiation models within those codes. Code validation is eased by comparisons to direct measurements of mass and current. Recently, crystal-imaging backlighting techniques have greatly improved our knowledge of the mass distribution [50,51]. Direct, quantitative measurements of the trailing mass distribution and areal density and mass distribution of the pinch at stagnation are needed to complement the chordally and axially integrated self-emission measurements presented in this paper. Measurements of plasma injection or ablation velocity or direct measurements of wire ablation rates would also be useful. Spectroscopic measurements of the densities and temperatures of both electrons and ions will also be critical to understand pinch stagnation physics.

Future applications of wire arrays to ICF for ignition and high fusion yields with the baseline double-pinch approach [8] will require scaling to powers of $\sim$1 PW/pinch at currents of about 60 MA. This level can only be reached [9] if the present powers achieved on *Z* with a 20-mm array ($\sim$125 TW) scaled with current no slower than $I^{1.85}$. The demonstrated scaling of power with current [20] for these single tungsten arrays at a 95-ns stagnation time is slower than this and implies peak array currents larger than 75–100 MA would be required, considerably in excess of those for which accelerators have been designed. Although hot-spot ICF or fast-ignition compression schemes require radiation pulse shaping, for which it is likely that nested wire arrays, nested shells, or arrays imploding on shells would be used, and *not* a single high-mass tungsten wire array scaled to keep the implosion time constant, it is clear that further optimization is required.

Trailing mass might affect performance on next-generation *z*-pinch accelerators such as the planned ZR accelerator [116] and future accelerators at high-yield-scale currents (50–60 MA) [117]. Were the 20-mm arrays scaled to ZR keeping the implosion time at $\sim$100 ns, the array mass would increase from 5.9 mg to about 20 mg. Since the current is scaled up accordingly, the time of ablation and acceleration might be unchanged compared to arrays on *Z*, based on the discussion in Sec. IV.

This is consistent with predictions of the "tuned" 2D G-MHD model (normalized to *Z* trajectory measurements in Sec. III) of a high-yield-scale 20-mm array. Assuming the trailing mass fraction is no smaller than the 30% observed on *Z*, a 20-mm array on ZR would have a trailing mass of 6 mg/cm. This is as large as the entire array mass for *Z*. The higher dI/dt of the current pulse on ZR might improve the uniformity of ablation or the acceleration of any trailing mass. However, the increase in absolute trailing mass and in axial electric field (a 60% larger voltage) might instead increase shunting of current to larger radii. We have no simulations or models that can actually predict the performance of arrays at larger currents.

In addition to potential effects on wire array and current dynamics, this increase in absolute trailing mass, if present, would affect the vacuum hohlraum energetics (specific heat loss) and secondary coupling efficiency [9,13]. We need a way to scale wire array performance to higher currents at constant radii, which reduces either the fraction of trailing mass or the absolute trailing mass or both, preferably. The long ablation period and poor performance of the 14.9-mg, 12-mm-diam arrays and the current scaling experiments of Ref. [20] also suggest caution when scaling the mass upwards to keep a constant implosion time and couple efficiently to the accelerator. A recent wire-array experiment that

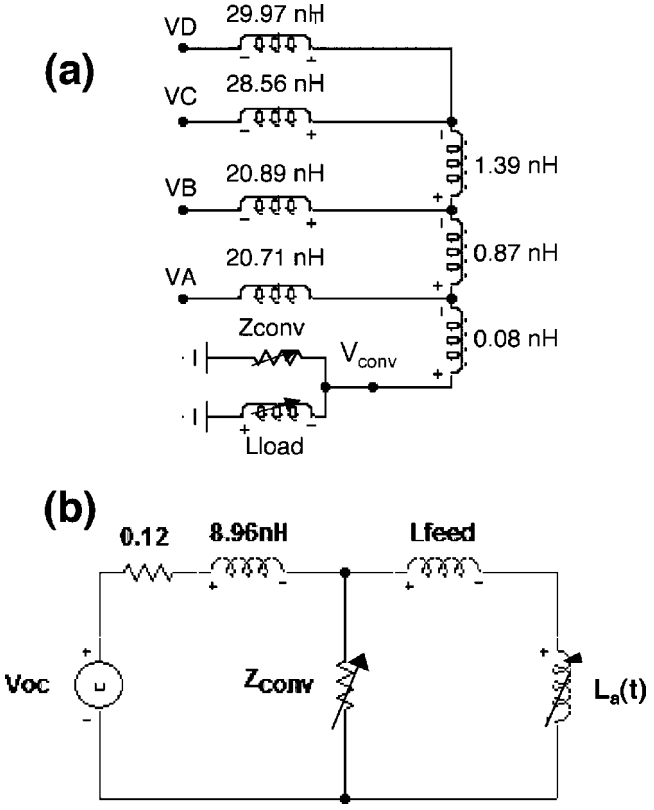

FIG. 24. (a) Equivalent circuit for the four-level *Z* transmission lines from the water-vacuum insulator stack convoluted into a single feed to the load. VA, VB, VC, and VD are the stack voltages for each level. The horizontal inductors are the transmission line inductances from the insulator stack to the convolute. The vertical inductors are the coupling inductances between the transmission lines in the convolute. (b) Equivalent circuit for the *Z* accelerator with a single constant impedance voltage source V_{OC}, a variable impedance element to model current loss in the convolute $Z_{conv}(t)$, and a variable inductance array $L_a(t)$.

lengthened the implosion time showed a reduction in radiated pinch powers with an increase in wire array mass, also consistent with this trend [118].

We want to maximize the rate of delivery of and simultaneity of arrival of mass and current at the axis. This requires a minimization of the trailing mass. Although this work strongly suggests a relationship between wire array ablation rate per unit array mass, wire-array dynamics (the normalized acceleration times), trailing mass and current, the peak compression of the current, and the scaling of power with peak load current, it is not clear what physical processes actually control the relationship or how the process itself scales. We speculate that trailing mass results from axially nonuniform wire ablation in the same manner as observed at lower currents. In this mechanism, regions that ablate through, first, implode and allow more-slowly ablating regions to trail. It may be that a longer wire ablation period modifies the amplitude and/or wavelength of the instability controlling the axial nonuniform ablation of the wires, subsequently leading to variations in trailing mass and trailing current.

These results suggest that a larger ablation rate per unit mass [$f_m \propto \Pi K/\tau_{stag} \propto I_m^2/[Rm_0V_a]$, Eq. (21)] will decrease the ablation time period. Higher ablation rate per unit mass is obtained with higher drive current, smaller array mass, and smaller ablation velocity (or conversely, higher Π, higher K, smaller τ_{stag}). Decreasing the mass of the array (for a fixed radius) would decrease the stagnation time, increase the ablation rate per unit mass, increase the wire burnthrough rate, and the array would ablate earlier, possibly with a lower fraction of trailing mass. Even were the fraction of trailing mass a constant of the array dynamics, a lower initial mass would imply a lower absolute amount of trailing mass. It is interesting to note that decreasing the mass of the array with fixed wire number results in the use of smaller-diameter wires. Data from single-wire experiments [119] show a higher wire ablation rate with smaller diameter wires.

The heuristic model of Stygar *et al.* [20] suggests that optimization of array performance requires shortening the array implosion time by increasing the array mass with increasing current more slowly than the $m_0 \sim I^2$ rate that maintains constant implosion time. Hence, a decrease in array mass is suggested based on an independent line of argument. Previous experiments on the Saturn accelerator [120] and several more recent experiments on Magpie [121] and *Z* [122,123] show that higher radiated powers are obtained for smaller array masses and shorter implosion times. Accelerators with faster risetimes to optimally drive lower-mass arrays with shorter implosion times might further increase the mass ablation rate and implosion velocity [124]. Shorter current pulse rise times improved axial uniformity of wire explosions in single-wire experiments [70] and might alter the dynamics of the process that allows mass to trail. Also, if the application permits, increasing the array radius would also increase the ablation rate per unit mass and decrease trailing mass, for a fixed stagnation time.

In conclusion, we do not necessarily want to maximize the kinetic energy at stagnation. This optimization would increase the array mass and implosion time to optimize energy transfer from a given accelerator, which is opposed to the direction suggested by scaling of the ablation rate per unit mass. The peak power may depend more strongly on the radial distribution of the current rather than the peak current. Future work needs to explore the relationship between trailing mass and current and ablation rates to maximize power. We need a more complete understanding of wire ablation rates, the physics of trailing mass and its scaling, the influence of ablation on the effective width of the imploding sheath, and the influence of trailing mass on the rate of transport of the current to the axis of the array and the final implosion velocities. We should continue to explore the relationship between trailing mass and current, the onset and rapid growth of $m=0$ instabilities on axis, the conversion of magnetic energy into radiation, and the possible termination of the pulse by the growth of MHD instabilities. Future work should also evaluate the observed correlation between the onset of an $m=1$ kink instability, higher compression, and the evolution of the harder x-ray spectrum.

TABLE VII. Symbol definitions.

Symbol	Definition
A	atomic mass number of plasma ions
A_h	hohlraum wall area
$\mathbf{B}$	magnetic-field induction
CR	radial convergence ratio
E	precursor total thermal energy
F	precursor view factor
I_a	accelerator total current
I, I_ℓ	wire array load current
I_{loss}	convolute loss current
$I_{\ell M}$	load current waveshape for Magpie accelerator
$I_{\ell Z}$	load current waveshape for Z accelerator
I_m	peak load current
$\mathbf{J}$	current density
K	dimensionless array ablation similarity parameter
K_A	ablation similarity parameter for Angara accelerator
K_M	ablation similarity parameter for Magpie accelerator
K_{12}	ablation similarity parameter for 12 mm array on Z
K_{20}	ablation similarity parameter for 20 mm array on Z
K_{40}	ablation similarity parameter for 40 mm array on Z
$L_a, L_a(t)$	wire array load inductance
$L_a(t_0)$	geometric wire array load inductance before array acceleration
L_{feed}	transmission line inductance upstream of convolute (not including L_a)
N	number of shots
P	radiated pinch soft x-ray power
$P_{\text{COMPOSITE}}$	composite pinch power waveform from P_{XRDCORR} and P_{SD}
PdV	rate of work done on plasma from a change in volume
P_{kin}	kinetic pressure of ablated plasma flow at the precursor surface
$P_{G\text{-MHD}}$	radiated power from Gorgon 1D-MHD simulation
P_{RV}	power from Rudakov-Velikovich model
$P(t)_{\text{SD}}$	pinch soft x-ray power inferred from silicon diode measurement
P_{SP}	radiated power from mass accretion by the imploding snowplow piston
P_{th}	thermal pressure of the precursor plasma
$P(t)_{\text{XRD}}$	pinch soft x-ray power from an XRD measurement
$P(t)_{\text{XRDCORR}}$	XRD power corrected for collimation by the diagnostic viewing slot
R	initial radius of wire array load
R_{cur}	effective radius of the current flow
R_f	final radius of plasma
R_i	initial radius of plasma
R_m	plasma magnetic Reynolds number
R_p	precursor equilibrium radius
R_{piston}	radius of the piston from a snowplow mass accretion model
T	precursor temperature
T_P	pinch brightness temperature
T_R	hohlraum radiation temperature
VA,VB,VC,VD	Z accelerator insulator stack voltage for levels A,B,C,D
V_A	plasma Alfven velocity
V_a	effective plasma ablation velocity from rocket model
$\langle V_{\text{array}} \rangle$	average array implosion velocity
V_{conv}	convolute voltage determined from stack voltage and circuit model

TABLE VII. (*Continued.*)

Symbol	Definition
V_o	initial convolute voltage determined from load current
V_{OC}	accelerator open circuit voltage
V_P	mass accretion piston velocity
$\overline{Z}$	average charge state of the ions in a plasma
$Z_{\mathrm{conv}}(t)$	convolute impedance
$a(t)$	pinch acceleration
d_o	initial anode-cathode gap distance
$d(t)$	time-dependent anode-cathode gap distance
dE/dt	rate of change of precursor thermal energy
dm_{ablate}/dt	wire array mass ablation rate per unit length
$dI/dt, dI_\ell/dt$	time derivative of wire array load current
dL_a/dt	time derivative of wire array load inductance
dv/dt	acceleration of the effective radius of the current
f_a	mass ablation fraction
f_{aM}	mass ablation fraction for Magpie
f_{aZ}	mass ablation fraction for *Z*
g_{aM}	mass ablation function for Magpie
g_{aZ}	mass ablation function for *Z*
f_m	fractional mass ablation rate
k	wave number
ℓ	wire array length
l	characteristic plasma length
m_{array}	initial mass of wire array per unit length
m_o	wire array or plasma mass per unit length
m	azimuthal mode number
n_e	plasma electron density
n_i	plasma ion density
$r, r(t)$	time dependent wire array radius
t_a, t_{ablate}	starting time for array acceleration or time at end of ablation phase
t_m	time of peak load current
v	characteristic plasma velocity
ΔL_a	change of array inductance from initial geometric inductance
Γ	growth rate of MHD instabilities
Π	dimensionless pinch acceleration similarity parameter
α	precursor pinch albedo
β	normalized time of peak load current $(=t_m/\tau_{\mathrm{stag}})$
δL	change of inductance from current convection with precursor plasma
$\delta m(t)$	total mass per unit length ablated from wire array
μ_o	permeability of free space
η	characteristic plasma resistivity
$\rho(r,t)$	precursor mass density profile
σ_B	Boltzmann radiation constant
σ	wire material conductivity
τ	characteristic timescale for implosion or motion
$\tau_a, \tau_{\mathrm{ablate}}$	array ablation or acceleration time normalized to stagnation time $(=t_a/\tau_{\mathrm{stag}})$
τ_A	Alfven transit time
τ_C	plasma clearing or compression timescale
τ_R	Rosseland mean optical depth
τ_{stag}	stagnation or implosion time of wire array

ACKNOWLEDGMENTS

This paper is based on an invited talk given at the 5th Dense *Z*-pinch Conference [44]. We thank J. F. Seamen, T. L. Gilliland, J. L. McKenney, D. O. Jobe, and the *Z* accelerator operations and data acquisition teams for their superb and tireless technical efforts to provide perfect experimental hardware, wire arrays, and instrumentation. We appreciate the programmatic support of M. K. Matzen, D. H. McDaniel, R. J. Leeper, and J. P. Quintenz. We are also grateful to the Alegra-MHD development team for their careful work. We thank H. C. Harjes for calculating the load mass for 20-mm arrays on ZR with a 100 ns implosion time. We acknowledge helpful discussions with J. E. Bailey (Sandia), M. Dunne (AWE), M. G. Haines (Imperial College), J. H. Hammer (LLNL), R. W. Lemke (Sandia), M. G. Mazarakis (Sandia), N. Pereira (Ecopulse), D. L. Peterson (LANL), and T. W. L. Sanford (Sandia). We thank Ray Lemke for a thorough technical review of this paper and T. L. Cutler for technical editing. Sandia is a multiprogram laboratory operated by Sandia Corporation, a Lockheed Martin Company, for the U.S. Department of Energy under Contract No. DE-AC04-94AL85000.

APPENDIX A: CIRCUIT MODELS FOR THE *Z* ACCELERATOR

Figure 24(a) shows an equivalent circuit diagram for the four *z* transmission lines from the vacuum insulator stack to the *z*-pinch load [53]. Four estimates for the convolute voltage can be derived, one from each branch of this circuit. At the convolute, all these voltages must be equal, so we simply average as one estimate for the convolute voltage. An equivalent method of deriving the convolute voltage is to assume that the current in each one of the four transmission lines is equal at the convolute [57]. The convolute voltage determined from this circuit is independent of the load impedance (e.g., independent of current conducted across the AK gap and/or through the pinch). Current is known to be lost at the convolute. This method is also independent of convolute loss if it is assumed to be small or if the effective position of the loss is at the top of the convolute. Figure 24(b) gives a circuit diagram for *Z* as a single voltage source [54], which is effectively identical to Fig. 24(a) but simpler to implement in a trajectory circuit model. The voltage source for this model is derived from insulator stack voltage and current measurements and projected back to the constant impedance section of the accelerator in the water section. An impedance element is included to model current loss in the convolute.

This circuit model and the monitors were calibrated to produce self-consistency with an independently measured time-dependent inductance of a short circuit load [57,101,102]. We adjusted the stack voltages by −7%, the accelerator feed inductance by +4%, and the measured currents by +2%. All of these changes are within the ±7% 1σ (random plus systematic) errors of the various probes and ±5% tolerance of the calculated inductances (random plus systematic). An inductive wire voltage monitor was also developed. Direct measurements of the voltage at the convolute with this monitor are consistent with values derived from the circuit and adjusted values of the stack and transmission line electrical data.

APPENDIX B: TABLE OF SYMBOL DEFINITIONS

Table VII provides definitions of symbols used throughout the text.

[1] T. W. L. Sanford, G. O. Allshouse, B. M. Marder, T. J. Nash, R. C. Mock, R. B. Spielman, J. F. Seamen, J. S. McGurn, D. Jobe, T. L. Gilliland, M. Vargas, K. W. Struve, W. A. Stygar, M. R. Douglas, M. K. Matzen, J. H. Hammer, J. S. DeGroot, J. L. Eddlemen, D. L. Peterson, D. Mosher, K. G. Whitney, J. W. Thornhill, P. E. Pulsifer, J. P. Apruzese, and Y. Maron, Phys. Rev. Lett. **77**, 5063 (1996).

[2] C. Deeney, T. J. Nash, R. B. Spielman, J. F. Seamen, G. A. Chandler, K. W. Struve, J. L. Porter, W. A. Stygar, J. S. McGurn, D. O. Jobe, T. L. Gilliland, J. A. Torres, M. F. Vargas, L. E. Ruggles, S. Breeze, R. C. Mock, M. R. Douglas, D. L. Fehl, D. H. McDaniel, M. K. Matzen, D. L. Peterson, W. Matuska, N. F. Roderick, and J. J. MacFarlane, Phys. Rev. E **56**, 5945 (1997).

[3] C. Deeney, M. R. Douglas, R. B. Spielman, T. J. Nash, D. L. Peterson, P. L. Eplattenier, G. A. Chandler, J. F. Seamen, and K. W. Struve, Phys. Rev. Lett. **81**, 4883 (1998).

[4] M. K. Matzen, Phys. Plasmas **4**, 1519 (1997).

[5] R. B. Spielman, C. Deeney, G. A. Chandler, M. R. Douglas, D. L. Fehl, M. K. Matzen, D. H. McDaniel, T. J. Nash, J. L. Porter, T. W. L. Sanford, J. F. Seamen, W. A. Stygar, K. W. Struve, S. P. Breeze, J. S. McGurn, J. A. Torres, D. M. Zagar, T. L. Gilliland, D. O. Jobe, J. L. McKenney, R. C. Mock, M. Vargas, T. Wagoner, and D. L. Peterson, Phys. Plasmas **5**, 2105 (1998).

[6] M. E. Cuneo, R. A. Vesey, J. L. Porter, G. A. Chandler, D. L. Fehl, T. L. Gilliland, D. L. Hanson, J. S. McGurn, P. G. Reynolds, L. E. Ruggles, H. Seamen, R. B. Spielman, K. W. Struve, W. A. Stygar, W. W. Simpson, J. A. Torres, D. F. Wenger, J. H. Hammer, P. W. Rambo, D. L. Peterson, and G. C. Idzorek, Phys. Plasmas **8**, 2257 (2001).

[7] J. L. Porter, Jr., Bull. Am. Phys. Soc. **42**, 1948 (1997).

[8] J. H. Hammer, M. Tabak, S. C. Wilks, J. D. Lindl, D. S. Bailey, P. W. Rambo, A. Toor, G. B. Zimmerman, and J. L. Porter, Phys. Plasmas **6**, 2129 (1999).

[9] M. E. Cuneo, R. A. Vesey, J. H. Hammer, J. L. Porter, L. E. Ruggles, and W. W. Simpson, Laser Part. Beams **19**, 481 (2001).

[10] M. E. Cuneo, R. A. Vesey, J. L. Porter, G. R. Bennett, D. L. Hanson, L. E. Ruggles, W. W. Simpson, G. C. Idzorek, W. A. Stygar, J. H. Hammer, J. J. Seamen, J. A. Torres, J. S. McGurn, and R. M. Green, Phys. Rev. Lett. **88**, 215004

(2002).
[11] G. R. Bennett, M. E. Cuneo, R. A. Vesey, J. L. Porter, R. G. Adams, R. A. Aragon, J. A. Caird, O. L. Landen, P. K. Rambo, D. C. Rovang, L. E. Ruggles, W. W. Simpson, I. C. Smith, and D. F. Wenger, Phys. Rev. Lett. **89**, 245002 (2002).
[12] M. E. Cuneo, R. A. Vesey, G. R. Bennett, J. L. Porter, D. L. Hanson, P. K. Rambo, D. B. Sinars, I. C. Smith, S. A. Slutz, W. A. Stygar, G. A. Chandler, J. P. Chittenden, S. V. Lebedev, T. J. Nash, M. K. Matzen, and C. L. Olson, *Proceedings of the 11th International Conference on Emerging Nuclear Energy Systems*, edited by B. L. Daniels and D. G. Cole (National Technical Information Service document number PB2003–102104, Springfield, VA), p. 189.
[13] R. A. Vesey, M. E. Cuneo, G. R. Bennett, J. L. Porter, R. G. Adams, R. A. Aragon, P. K. Rambo, L. E. Ruggles, W. W. Simpson, and I. C. Smith, Phys. Rev. Lett. **90**, 035005 (2003).
[14] T. J. Nash, M. S. Derzon, G. A. Chandler, R. Leeper, D. Fehl, J. Lash, C. Ruiz, G. Cooper, J. F. Seamen, J. McGurn, S. Lazier, J. Torres, D. Jobe, T. Gilliland, M. Hurst, R. Mock, P. Ryan, D. Nielsen, J. Armijo, J. McKenney, R. Hawn, D. Hebron, J. J. MacFarlane, D. Peterson, R. Bowers, W. Matuska, and D. D. Ryutov, Phys. Plasmas **6**, 2023 (1999).
[15] S. A. Slutz, M. R. Douglas, J. S. Lash, R. A. Vesey, G. A. Chandler, T. J. Nash, and M. S. Derzon, Phys. Plasmas **8**, 1673 (2001).
[16] J. E. Bailey, G. A. Chandler, S. A. Slutz, G. R. Bennett, G. Copper, J. S. Lash, S. Lazier, R. Lemke, T. J. Nash, D. S. Nielsen, T. C. Moore, C. L. Ruiz, D. G. Schroen, R. Smelser, J. Torres, and R. A. Vesey, Phys. Rev. Lett. **89**, 095004 (2002).
[17] J. E. Bailey, G. A. Chandler, D. Cohen, M. E. Cuneo, M. E. Foord, R. F. Heeter, D. Jobe, P. W. Lake, J. J. MacFarlane, T. J. Nash, D. S. Nielsen, R. Smelser, and J. Torres, Phys. Plasmas **9**, 2186 (2002).
[18] R. F. Heeter, J. E. Bailey, M. E. Cuneo, J. Emig, M. E. Foord, P. T. Springer, and R. S. Thoe, Rev. Sci. Instrum. **72**, 1224 (2001).
[19] D. D. Ryutov, M. S. Derzon, and M. K. Matzen, Rev. Mod. Phys. **72**, 167 (2000).
[20] W. A. Stygar, H. C. Ives, D. L. Fehl, M. E. Cuneo, M. G. Mazarakis, J. E. Bailey, D. E. Bliss, G. A. Chandler, R. J. Leeper, M. K. Matzen, D. H. McDaniel, J. S. McGurn, J. L. McKenney, L. P. Mix, D. J. Muron, J. L. Porter, J. J. Ramirez, L. E. Ruggles, J. F. Seamen, W. W. Simpson, C. S. Speas, R. B. Spielman, K. W. Struve, J. A. Torres, R. A. Vesey, T. C. Wagoner, T. L. Gilliland, G. R. Bennett, D. O. Jobe, S. E. Lazier, J. A. Mills, T. D. Mulville, J. H. Pyle, T. M. Romero, J. J. Seamen, J. D. Serrano, and R. M. Smelser, Phys. Rev. E **69**, 046403 (2004).
[21] J. H. Hammer, J. L. Eddleman, P. T. Springer, M. Tabak, A. Toor, K. L. Wong, G. B. Zimmerman, C. Deeney, R. Humphreys, T. J. Nash, T. W. L. Sanford, R. B. Spielman, and J. S. DeGroot, Phys. Plasmas **3**, 2063 (1996).
[22] D. L. Peterson, R. L. Bowers, K. D. McLenithan, C. Deeney, G. A. Chandler, R. B. Spielman, M. K. Matzen, and N. F. Roderick, Phys. Plasmas **5**, 3302 (1998).
[23] D. L. Peterson, R. L. Bowers, W. Matuska, K. D. McLenithan, G. A. Chandler, C. Deeney, M. S. Derzon, M. Douglas, M. K. Matzen, T. J. Nash, R. B. Spielman, K. W. Struve, and W. A. Stygar, and N. F. Roderick, Phys. Plasmas **6**, 2178 (1999).
[24] T. W. L. Sanford, Laser Part. Beams **19**, 541 (2001).
[25] S. V. Lebedev, I. H. Mitchell, R. Aliaga-Rossel, S. N. Bland, J. P. Chittenden, A. E. Dangor, and M. G. Haines, Phys. Rev. Lett. **81**, 4152 (1998).
[26] S. V. Lebedev, R. Aliaga-Rossel, S. N. Bland, J. P. Chittenden, A. E. Dangor, M. G. Haines, and I. H. Mitchell, Phys. Plasmas **6**, 2016 (1999).
[27] J. P. Chittenden, S. V. Lebedev, A. R. Bell, R. Aliaga-Rossel, S. N. Bland, and M. G. Haines, Phys. Rev. Lett. **83**, 100 (1999).
[28] S. V. Lebedev, F. N. Beg, S. N. Bland, J. P. Chittenden, A. E. Dangor, M. G. Haines, S. A. Pikuz, and T. Shelkovenko, Phys. Rev. Lett. **85**, 98 (2000).
[29] J. P. Chittenden, S. V. Lebedev, S. N. Bland, F. N. Beg, and M. G. Haines, Phys. Plasmas **8**, 2305 (2001).
[30] J. P. Chittenden, S. V. Lebedev, S. N. Bland, J. Ruiz-Camacho, F. N. Beg, and M. G. Haines, Laser Part. Beams **19**, 323 (2001).
[31] S. V. Lebedev, F. N. Beg, S. N. Bland, J. P. Chittenden, A. E. Dangor, M. G. Haines, S. A. Pikuz, and T. A. Shelkovenko, Laser Part. Beams **19**, 355 (2001).
[32] S. V. Lebedev, F. N. Beg, S. N. Bland, J. P. Chittenden, A. E. Dangor, M. G. Haines, K. H. Kwek, S. A. Pikuz, and T. A. Shelkovenko, Phys. Plasmas **8**, 3734 (2001).
[33] S. V. Lebedev, F. N. Beg, S. N. Bland, J. P. Chittenden, A. E. Dangor, and M. G. Haines, Phys. Plasmas **9**, 2293 (2002).
[34] V. P. Smirnov, Bull. Am. Phys. Soc. **45**, 61(2000).
[35] V. V. Aleksandrov, A. V. Branitskii, G. S. Volkov, E. V. Grabovsky, M. V. Zurin, S. L. Nedoseev, G. M. Oleinik, A. A. Samokhin, P. V. Sasorov, V. P. Smirnov, M. V. Fedulov, and I. N. Frolov, Plasma Phys. Rep. **27**, 89 (2001).
[36] V. V. Aleksandrov, I. N. Frolov, M. V. Fedulov, E. V. Grabovsky, K. N. Mitrofanov, S. L. Nedoseev, G. M. Oleinik, I. Yu. Porofeev, A. A. Samokhin, P. V. Sasorov, G. S. Volkov, M. M. Zurin, and G. G. Zukakischvili, IEEE Trans. Plasma Sci. **30**, 559 (2002).
[37] V. V. Aleksandrov, A. G. Alekseev, V. N. Amosov, M. M. Basko, G. S. Volkov, E. V. Garbovskii, A. V. Krasilnikov, G. M. Oleinik, I. N. Rastyagaev, P. V. Sasorov, A. A. Samokhin, V. P. Smirnov, and I. N. Frolov, Plasma Phys. Rep. **29**, 1034 (2003).
[38] V. V. Alexandrov, E. V. Grabovsky, G. G. Zukakishvili, M. V. Zurin, N. N. Komarov, I. V. Krasovsky, K. N. Mitrofanov, S. L. Nedoseev, G. M. Oleinik, I. Yu. Porofeev, A. A. Samokhin, P. V. Sasorov, V. P. Smirnov, M. V. Fedulov, I. N. Frolov, and A. A. Chernov, JETP **97**, 745 (2003).
[39] E. V. Grabovskii, G. G. Zukakishvili, S. L. Nedoseev, G. M. Oleinik, and I. Yu. Porofeev, Plasma Phys. Rep. **30**, 30 (2004).
[40] E. V. Grabovskii, K. N. Mitrofanov, G. M. Oleink, and I. Yu. Porofeev, Plasma Phys. Rep. **30**, 121 (2004).
[41] M. E. Cuneo, G. A. Chandler, W. E. Fowler, S. Lazier, D. Nielsen, J. L. Porter, R. B. Spielman, K. W. Struve, R. A. Vesey, G. R. Bennett, L. E. Ruggles, W. W. Simpson, H. Seamen, J. Chittenden, S. Lebedev, D. Sinars, K. Chandler, D. Hammer, M. Hu, B. Kusse, and D. L. Peterson, http://dorland.pp.ph.ic.ac.uk/magpie/publications/workshop2001/Cuneo.pdf
[42] M. E. Cuneo, G. A. Chandler, R. A. Vesey, J. L. Porter, T. J. Nash, J. E. Bailey, R. A. Aragon, W. E. Fowler, W. A. Stygar, K. W. Struve, J. A. Torres, J. S. McGurn. S. E. Lazier, D. S.

Nielsen, J. P. Chittenden, and S. V. Lebedev, Bull. Am. Phys. Soc. **46**, 234 (2001).

[43] G. A. Chandler, M. E. Cuneo, R. A. Aragon, J. E. Bailey, C. A. Coverdale, M. Douglas, T. J. Nash, W. A. Stygar, K. W. Struve, R. B. Spielman, S. E. Lazier, J. P. Chittenden, and S. V. Lebedev, in *Proceedings of the 28th International IEEE Conference on Plasma Science, Las Vegas, NV, 2001*, edited by R. Reinovsky and T. Hussey (IEEE, Piscataway, NJ, 2001), p. 189 (IEEE Catalog No. 01-CH37255).

[44] M. E. Cuneo, G. A. Chandler, J. P. Chittenden, S. V. Lebedev, R. A. Vesey, T. J. Nash, J. L. Porter, D. Nielsen, S. E. Lazier, R. A. Aragon, J. E. Bailey, W. E. Fowler, J. S. McGurn, L. E. Ruggles, W. W. Simpson, K. W. Struve, W. A. Stygar, and J. A. Torres (unpublished).

[45] I. K. Aivazov, V. D. Vikharev, and G. S. Volkov, L. B. Nikandrov, V. P. Smirnov, and V. Ya. Tsarfin, Sov. J. Plasma Phys. **14**, 110 (1988).

[46] E. J. Yadlowski, J. J. Moschella, R. C. Hazelton, T. B. Setterson, G. C. Spanjers, C. Deeney, B. H. Failor, P. D. LePell, J. Davis, J. P. Zpruzese, K. G. Whitney, and J. W. Thornhill, Phys. Plasmas **3**, 1745 (1996).

[47] C. Deeney J. McGurn, D. Noack, J. L. Porter, R. B. Spielman, D. O. Jobe, M. F. Vargas, T. Gilliland, M. R. Douglas, and M. K. Matzen, Rev. Sci. Instrum. **68**, 653 (1997).

[48] T. W. L. Sanford, R. W. Lemke, R. C. Mock, G. A. Chandler, D. L. Peterson, R. E. Chrien, G. C. Idzorek, R. G. Watt, and J. P. Chittenden, Phys. Plasmas **9**, 3573 (2002)

[49] T. J. Nash, M. S. Derzon, G. A. Chandler, D. L. Fehl R. J. Leeper, J. L. Porter, R. B. Spielman, C. Ruiz, G. Cooper, J. McGurn, M. Hurst, D. Jobe, J. Torres, J. Seaman, K. Struve, S. Lazier, T. Gilliland, L. A. Ruggles, W. A. Simpson, R. Adams, J. A. Seaman, D. Wenger, D. Nielsen, P. Riley, R. French, B. Stygar, T. Wagoner, T. W. L. Sanford, R. Mock, J. Asay, C. Hall, M. Knudson, J. Armijo, J. McKenney, R. Hawn, D. Schroen-Carey, D. Hebron, T. Cutler, S. Dropinski, C. Deeney, P. D. LePell, C. A. Coverdale, M. Douglas, M. Cuneo, D. Hanson, J. E. Bailey, P. Lake, A. Carlson, C. Wakefield, J. Mills, J. Slopek, T. Dinwoodie, and G. Idzorek, Rev. Sci. Instrum. **72**, 1167 (2001).

[50] D. B. Sinars, G. R. Bennett, D. F. Wenger, M. E. Cuneo, J. L. Porter, R. G. Adams, P. K. Rambo, D. C. Rovang, and I. C. Smith, Rev. Sci. Instrum. **75**, 3672 (2004).

[51] D. B. Sinars, M. E. Cuneo, E. P. Yu, D. E. Bliss, T. J. Nash, J. L. Porter, C. Deeney, M. G. Mazarakis, G. S. Sarkisov, and D. F. Wenger, Phys. Rev. Lett. **93**, 145002 (2004).

[52] W. A. Stygar, R. B. Spielman, G. O. Allshouse, C. Deeney, D. R. Humphreys, H. C. Ives, F. W. Long, T. H. Martin, M. K. Matzen, D. H. McDaniel, C. W. Mendel, L. P. Mix, T. J. Nash, J. W. Poukey, J. J. Ramirez, T. W. L. Sanford, J. F. Seamen, D. B. Seidel, J. W. Smith, D. M. VanDeValde, R. W. Wavrick, P. A. Corcoran, J. W. Douglas, I. D. Smith, M. A. Mostrom, K. W. Struve, T. P. Hughes, R. E. Clark, R. W. Shoup, T. C. Wagoner, T. L. Gilliland, and B. P. Peyton, in *Proceedings of the 11th International Pulsed Power Conference, Baltimore, MD, 1997*, edited by G. Cooperstein and I. Vitkovitski (IEEE Piscataway, NJ, 1997), Vol. 1, p. 591 (IEEE Catalog No. 97CH36127).

[53] P. C. Corcoran, J. W. Douglas, I. D. Smith, P. W. Spence, W. A. Stygar, K. W. Struve, T. H. Martin, R. B. Spielman, and H. C. Ives, in *Proceedings of the 11th International Pulsed Power Conference* [52], p. 466.

[54] K. W. Struve, T. H. Martin, R. B. Spielman, W. A. Stygar, P. A. Corcoran, and J. W. Douglas, in *Proceedings of the 11th International Pulsed Power Conference* [52], p. 162.

[55] W. A. Stygar, R. B. Spielman, H. C. Ives, W. B. S. Moore, J. F. Seamen, A. W. Sharpe, T. C. Wagoner, T. L. Gilliland, R. S. Broyles, J. A. Mills, T. A. Dinwoodie, J. S. Slopek, K. W. Struve, and P. G. Reynolds, in *Proceedings of the 11th International Pulsed Power Conference* [52], Vol. 2, p. 1258.

[56] T. D. Pointon, W. A. Stygar, R. B. Spielman, H. C. Ives, and K. W. Struve, Phys. Plasmas **8**, 4534 (2001).

[57] E. M. Waisman, M. E. Cuneo, W. A. Stygar, R. L. Lemke, K. W. Struve, and T. C. Wagoner, Phys. Plasmas **11**, 2009 (2004).

[58] G. A. Chandler, C. Deeney, M. Cuneo, D. L. Fehl, J. S. McGurn, R. B. Spielman, J. A. Torres, J. L. McKenney, J. Mills, and K. W. Struve, Rev. Sci. Instrum. **70**, 561 (1999).

[59] R. B. Spielman, C. Deeney, D. L. Fehl, D. L. Hanson, N. R. Keltner, J. S. McGurn, and J. L. McKenney, Rev. Sci. Instrum. **70**, 651 (1999).

[60] G. C. Idzorek and R. J. Bartlett, in *Proceedings of the 11th International Pulsed Power Conference* [52], Vol. 2, pp. 1274–1279.

[61] L. E. Ruggles, M. E. Cuneo, J. L. Porter, D. F. Wenger, and W. W. Simpson, Rev. Sci. Instrum. **72**, 1218 (2001).

[62] M. C. Hettrick, M. E. Cuneo, J. L. Porter, L. E. Ruggles, W. W. Simpson, M. F. Vargas, and D. F. Wenger, Appl. Opt. **43**, 3772 (2004).

[63] L. E. Ruggles, R. B. Spielman, J. L. Porter, and S. P. Breeze, Rev. Sci. Instrum. **66** 712(1995).

[64] S. E. Lazier, T. L. Barber, M. S. Derzon, and J. W. Kellog, Rev. Sci. Instrum. **68**, 660 (1997).

[65] T. J. Nash, M. S. Derzon, G. A. Chandler, D. Fehl, R. Leeper, M. Hurst, D. Jobe, J. Torres, J. Seamen, S. Lazier, T. Gilliland, and J. McGurn, Rev. Sci. Instrum. **70**, 4664 (1999).

[66] The terms "stagnation time" or "implosion time" are equivalent. We use "stagnation time" to indicate the start of phase IV when pinch power rapidly increases to peak. This avoids confusion with the phrase "implosion phase" to represent phase III, when acceleration toward the axis of the array takes place.

[67] S. A. Pikuz, T. A. Shelkovenko, D. B. Sinars, J. B. Greenly, Y. S. Dimant, and D. A. Hammer, Phys. Rev. Lett. **83**, 4313 (1999).

[68] D. B. Sinars, T. A. Shelkovenko, S. A. Pikuz, J. B. Greenly, and D. A. Hammer, Phys. Plasmas **7**, 1555 (2000).

[69] D. B. Sinars, M. Hu, K. M. Chandler, T. A. Shelkovenko, S. A. Pikuz, J. B. Greenly, D. A. Hammer, and B. R. Kusse, Phys. Plasmas **8**, 216 (2001).

[70] G. S. Sarkisov, B. S. Bauer, and J. S. DeGroot, JETP Lett. **73**, 69 (2001).

[71] K. Chandler, D. A. Hammer, D. B. Sinars, S. A. Pikuz, and T. A. Shelkovenko, IEEE Trans. Plasma Sci. **30**, 537 (2002).

[72] G. S. Sarkisov, P. V. Sasorov, K. W. Struve, D. H. McDaniel, A. N. Gibov, and G. M. Oleinik, Phys. Rev. E **66**, 046413(2002).

[73] P. U. Duselis and B. R. Kusse, Phys. Plasmas **10**, 565 (2003).

[74] M. D. Johnston, Y. Y. Lau, R. M. Gilgenbach, T. S. Strickler, M. E. Cuneo, and T. A. Mehlhorn, Appl. Phys. Lett. **83**, 4915 (2003).

[75] L. L. Rudakov, A. L. Velikovich, J. Davis, J. W. Thornhill, J. L. Guiliani, Jr., and C. Deeney, Phys. Rev. Lett. **84**, 3326

(2000).
[76] A. L. Velikovich, J. Davis, J. W. Thornhill, and J. L. Guiliani, Jr., L. I. Rudakov, and C. Deeney, Phys. Plasmas **7**, 3265 (2000).
[77] M. R. Douglas, C. Deeney, R. B. Spielman, C. A. Coverdale, N. F. Roderick, and D. L. Peterson, Phys. Plasmas **7**, 1935 (2000).
[78] T. J. Nash, M. E. Cuneo, R. B. Spielman, G. A. Chandler, D. B. Sinars, R. J. Leeper, J. F. Seaman, J. McGurn, S. Lazier, J. Torres, D. Jobe, T. Gilliland, D. Nielsen, R. Hawn, J. E. Bailey, P. Lake, A. L. Carlson, H. Seamen, T. Moore, R. Smelser, J. Pyle, T. Wagoner, P. D. LePell, C. Deeney, M. R. Douglas, D. McDaniel, K. Struve, M. Mazarakis, and W. Stygar, Phys. Plasmas **11**, 5156 (2004).
[79] G. B. Zimmerman and W. L. Kruer, Comments Plasma Phys. Controlled Fusion **2**, 51 (1975).
[80] C. Garasi, D. Bliss, T. A. Mehlhorn, B. V. Oliver, A. C. Robinson, and G. S. Sarkisov, Phys. Plasmas **11**, 2729 (2004).
[81] J. P. Chittenden, S. V. Lebedev, B. V. Oliver, E. P. Yu, and M. E. Cuneo, Phys. Plasmas **11**, 1118 (2004).
[82] B. V. Oliver, C. J. Garasi, T. A. Mehlhorn, and E. P. Yu, Bull. Am. Phys. Soc. **47**, 243 (2002).
[83] K. G. Whitney, J. W. Thornhill, P. E. Pulsifer, J. P. Apruzese, T. W. L. Sanford, T. J. Nash, R. C. Mock, and R. B. Spielman, Phys. Rev. E **56**, 3540 (1997).
[84] S. N. Bland, S. V. Lebedev, J. P. Chittenden, C. Jennings, and M. G. Haines, Phys. Plasmas **10**, 1100 (2003).
[85] J. P. Chittenden, S. V. Lebedev, M. E. Cuneo, C. A. Jennings, and A. Ciardi, in *Dense Z-Pinches*, edited by Jack Davis, Christopher Deeney, and Nino R. Pereira, AIP Conf. Proc. No. 651 (AIP, Melville, NY, 2002), p. 354.
[86] P. V. Sasorov, Sov. J. Plasma Phys. **16**, 281 (1990).
[87] P. V. Sasorov, Sov. J. Plasma Phys. **17**, 874 (1991).
[88] R. E. Terry and N. R. Pereira, Phys. Fluids B **3**, 195 (1991).
[89] M. A. Liberman, J. S. DeGroot, A. Torr, and R. B. Spielman, *Physics of High-Density Z-Pinch Plasmas* (Springer, New York, 1999).
[90] W. A. Stygar, R. E. Olson, R. B. Spielman, and R. J. Leeper, Phys. Rev. E **64**, 026410 (2001).
[91] S. V. Lebedev, D. J. Ampleford, S. N. Bland, S. Bott, J. P. Chittenden, C. Jennings, M. G. Haines, J. B. A. Palmer, and J. Rapley, Nucl. Fusion **44**, S215 (2004).
[92] J. S. DeGroot, A. Toor, S. M. Golberg, and M. A. Liberman, Phys. Plasmas **4**, 737(1997).
[93] A. L. Velikovich, F. L. Cochran, J. Davis, and Y. K. Chong, Phys. Plasmas **5**, 3377 (1998).
[94] M. R. Douglas, C. Deeney, and N. F. Roderick, Phys. Plasmas **8**, 238(2001).
[95] J. P. Apruzese, P. E. Pulsifer, J. Davis, R. W. Clark, K. G. Whitney, J. W. Thornhill, T. W. L. Sanford, G. A. Chandler, C. Deeney, D. L. Fehl, T. J. Nash, R. B. Spielman, W. A. Stygar, K. W. Struve, R. C. Mock, T. L. Gilliland, D. O. Jobe, J. S. McGurn, J. F. Seamen, J. A. Torres, and M. Vargas, Phys. Plasmas **5**, 4476 (1998).
[96] S. V. Lebedev, J. P. Chittenden, F. N. Beg, S. N. Bland, A. Ciardi, D. Ampleford, S. Hughes, M. G. Haines, A. Frank, E. G. Blackman, and T. Gardiner, Astrophys. J. **564**, 113 (2002).
[97] M. G. Haines, IEEE Trans. Plasma Sci. **26**, 1275 (1998).
[98] M. R. Desjarlais and B. M. Marder, Phys. Plasmas **6**, 2057 (1999).
[99] J. H. Hammer and D. D. Ryutov, Phys. Plasmas **6**, 3302 (1999).
[100] M. P. Desjarlais, Contrib. Plasma Phys. **41**, 267 (2001).
[101] G. V. Ivanenkov, A. R. Mingaleev, S. A. Pikuz, V. M. Romanova, T. A. Shelkovenko, W. Stepniewski, and D. A. Hammer, JETP Lett. **87**, 663 (1998).
[102] R. W. Lemke, M. D. Knudsen, C. A. Hall, T. A. Haill, M. P. Desjarlais, J. R. Asay, and T. A. Mehlhorn, Phys. Plasmas **10**, 1092 (2003).
[103] R. W. Lemke, M. D. Knudsen, A. C. Robinson, T. A. Haill, K. W. Struve, J. R. Asay, and T. A. Mehlhorn, Phys. Plasmas **10**, 1867 (2003).
[104] M. P. Desjarlais, J. D. Kress, and L. A. Collins, Phys. Rev. E **66**, 025401(R) (2002).
[105] M. D. Johnston, R. M. Gilgenbach, T. S. Strickler, Y. Y. Lau, M. C. Jones, T. A. Mehlhorn, and M. E. Cuneo, Bull. Am. Phys. Soc. **48**, 235 (2003).
[106] M. E. Cuneo, IEEE Trans. Dielectr. Electr. Insul. **6**, 469 (1999).
[107] M. Sherlock, J. P. Chittenden, S. V. Lebedev, and M. G. Haines, Phys. Plasmas **11**, 1609 (2004).
[108] M. G. Haines, IEEE Trans. Plasma Sci. **30**, 588 (2002).
[109] M. G. Haines, Plasma Phys. Rep. **29**, 586 (2003).
[110] R. J. Taylor, Proc. Phys. Soc. London, Sect. B **70**, 31 (1957).
[111] M. Coppins, Plasma Phys. Controlled Fusion **30**, 201 (1988).
[112] A. E. Dangor, D. Favre, M. B. Dominguez, S. Lee, and E. Kahn, Phys. Rev. A **27**, 2751 (1983).
[113] N. R. Pereira, N. Rostoker, and J. S. Pearlman, J. Appl. Phys. **55**, 704 (1984).
[114] V. V. Neudachin and P. V. Sasorov, Nucl. Fusion **31**, 1053 (1991).
[115] V. Vikhrev, V. V. Ivankov, and G. A. Rozanova, Nucl. Fusion **33**, 311 (1993).
[116] D. H. McDaniel, M. G. Mazarakis, D. E. Bliss, J. M. Elizondo, H. C. Harjes, H. C. Ives, III, D. L. Kitterman, J. E. Maenchen, T. D. Pointon, S. E. Rosenthal, D. L. Smith, K. W. Struve, W. A. Stygar, E. A. Weinbrecht, D. L. Johnson, and J. P. Corely, in *Dense Z-Pinches* [85], p. 23.
[117] K. W. Struve, J. P. Corely, D. L. Johnson, D. H. McDaniel, R. B. Spielman, and W. A. Stygar, in *Proceedings of the 12th IEEE International Pulsed Power Conference*, edited by C. Stallings and H. Kirbe (IEEE, Piscataway, NJ, 1999), Vol. 1, p. 493.
[118] T. W. L. Sanford, R. W. Lemke, R. C. Mock, and D. L. Peterson, Phys. Plasmas **10**, 3252 (2003).
[119] S. A. Pikuz, T. A. Shelkovenko, A. R. Mingaleev, D. A. Hammer, and H. P. Neves, Phys. Plasmas **6**, 4272 (1999).
[120] T. W. L. Sanford, R. C. Mock, R. B. Spielman, D. L. Peterson, D. Mosher, and N. F. Roderick, Phys. Plasmas **5**, 3737 (1998).
[121] S. V. Lebedev and S. N. Bland (private communication).
[122] D. B. Sinars and M. E. Cuneo (private communication).
[123] M. G. Mazarakis and M. E. Cuneo (private communication).
[124] M. E. Cuneo and W. A. Stygar (private communication).